THE UNIVERSITY OF CHICAGO

ENABLING NON-CIRCULAR IGRT IMAGING TRAJECTORIES WITH OPTIMIZATION-BASED RECONSTRUCTION ALGORITHMS

A DISSERTATION SUBMITTED TO
THE FACULTY OF THE DIVISION OF THE BIOLOGICAL SCIENCES
AND THE PRITZKER SCHOOL OF MEDICINE
IN CANDIDACY FOR THE DEGREE OF
DOCTOR OF PHILOSOPHY

COMMITTEE ON MEDICAL PHYSICS

BY
ANDREW MICHAEL DAVIS

CHICAGO, ILLINOIS
MARCH 2018

To all who have been directly or indirectly afflicted by cancer – especially my Dad

The Art of Peace is medicine for a sick world. We want to cure the world of the sickness of violence, malcontent, and discord—this is the Way of Harmony. There is evil and disorder in the world because people have forgotten that all things emanate from one source. Return to that source and leave behind all self-centered thoughts, petty desires, and anger. Those who are possessed by nothing possess everything.

お先生 (Ueshiba Morihei Sensei)

TABLE OF CONTENTS

LIST OF FIGURES

LIST OF TABLES

ACKNOWLEDGMENTS

I would first like to express my deepest gratitude to the guidance provided by Drs. Charles Pelizzari and Xiaochuan Pan. Working with these exemplarly scientists in their labs has been one of the most rewarding experiences in my life. Their curioisty and dedication to the scietific method as well as their dedication to their students has given me a clear picture of the archetypical scientist and mentor. I am indebted to these two men for their efforts in guiding my scientific training.

I also would like to thank my committee members Drs. Hania Al-Hallaq and Emil Sidky for their stimulating feedback, discussions, and additional guidance in my research. Like Drs. Pan and Pelizzari, they have been extremely supportive of my research endeavors and instrumental in helping me devekop as a scientist. From the intial coursework at the start of my graduate education to the research presented in this work, my committee and adviers have provided me with a high standard of what it means to be a scientist through their example.

Furthermore, I would like to thanks my fellow friends and lab mates Sean Rose and Drs. Buxin Chen, Zheng Zhang, Adrian Sánchez, Xiao Han, Junguo Bian, Dan Xia, and Erik Pearson. Together, they have provided vast amounts of help, feedback, support, and friendship during my graduate work. I would also like to thank my classmate Dr. Meredith Sadinski as well as fellow students Drs. Dave Rigie, Johnathan Rosenfield, Gage Redler, Alex Cunliffe, Kevin Little, Zachary Grelewic, and Zacariah Labby who also provided engaging discussion and feedback throughout my studies. I also would like to extend my gratitude to the rest of the students in the Committee of Medical Physics for providing a wonderful learning environment.

This work was made possible by in part by the Lawrence H. Lanzl Fellowship, the GPMP T32 training grant, and NIH Grants R01 CA182264, R01EB018102, S10 RR021039 and P30 CA14599. Additional funding was provided by Varian Medial Systems with particular gratitude to Dr. Timo Berkhus for stimulating conversation and feedback as well as Drs.

Pascal Paysan and Dieter Seghers for providing and assisting with the iTools Reconstruction software. The contents of this work are solely the responsibility of the author and do not necessarily represent the official view of any of the supporting organizations.

ABSTRACT

The use of cone-beam computed tomography (CBCT) in image-guided radiation therapy (IGRT) has helped linear accelerators (LINACs) become the most popular form of radiation therapy today. The ability to acquire tomographic information from the patient at the treatment position allows for setup and target verification as well as steeper dose gradients and higher dose fractions while simultaneously providing images that allow the oncologist to monitor the tumor's response to the therapy. The current kV-CBCT scanning configuration of this LINAC-mounted imaging system provides a circular trajectory of the source and detector around the patient as the LINAC gantry makes a single rotation around the patient. Though this provides the requisite trajectory for the analytic-base FDK reconstruction algorithm that is the workhorse of clinical reconstruction in IGRT today, there are some issues of this scanning geometry that can either limit or even prevent the use of this CBCT information in clinical practice. In this work, we develop a generalized non-circular scanning trajectory framework enabled by optimization-based reconstruction that allow for non-circular trajectories that directly address two issues of LINAC-mounted CBCT for IGRT. The first issue is overcoming the limited axial coverage provided by the current detector size and circular acquisition trajectory. This is problematic as the CBCT axial coverage is smaller than the potential treatment field size. As engineering costs restrict the axial coverage of the detector, we investigate potential non-circular trajectories that can extend the axial coverage with current LINAC-mounted CBCT detectors. The other existing limitation that could be resolved with non-circular scanning trajectories is that of potential patient collisions with the LINAC gantry. As some patient treatment positions can put the patient in a collision path with components of the LINAC gantry, the inability to acquire the full circular rotation can lead to forgoing the CBCT. This is another problem to which we provide example trajectories that could alleviate these collisions while still acquiring useful CBCT images. We found that in both of these examples, our non-circular imaging framework was able to reconstruct images that have comparable image quality to the current clinical

method using a single circular scan while simultaneously providing potential solutions to the current clinical limitation of restricted axial coverage and potential patient collisions with the LINAC gantry.

CHAPTER 1

INTRODUCTION

Tomography is the imaging technique of using a penetrating wave to create an image of a slice in an object while either blurring or obscuring details from other planes in the object. The ability to peer inside an object and create a map of its contents is a powerful tool that is routinely used in myriad applications. Today, tomographic methods have been deployed in locations ranging from border-control checkpoints to local medical clinics.

As the non-invasive nature of tomographic imaging had obvious benefits for the field of medicine, many significant advances in tomographic technology were driven by clinical research. One such form of tomographic imaging is x-ray computed tomography (CT) which uses projection images acquired from different locations around the object to compute the distribution of material densities inside the object. With the growth of tomographic imaging, additional technologies were developed to acquire images using a variety of waves from ultrasound to injecting radioactive tracers which emit these waves from inside a patient as in single-photon computed tomography (SPECT) and positron emission tomography (PET).

1.1 CT development history

In a CT scanner system, an x-ray source and opposing detector typically rotate in a circle relative to the object being imaged as x-ray projection images are acquired at different angular positions. By modeling the attenuation of the incident x-rays by the object being imaged at different projection angles and finding an approximate inversion of this model, an estimate of the object's interior could be produced. The development of modern CT imaging systems today was driven not only by innovation in the hardware design, but also by advances in the algorithms used to invert the poorly conditioned forward model encountered in CT imaging.

Figure (1.1) shows a schematic of the first generation of CT scanner, which was built by

EMI (*Electric and Musical Industries Ltd.*) in 1967 using the work of Allan M. Cormack and Godfrey N. Hounsfield [7]. In this design, a source and detector acquire a series of pencil-beam projections by translating together along a line in a plane orthogonal to the rotation axis. The source and detector then rotate before acquiring another series of projections along another line. This process is repeated for successive rotation angles until the system has rotated an entire 180° and the source and detector have moved to each other's starting position. For their work, Cormack and Housfield shared the 1979 Nobel Prize in Physiology or Medicine [28].

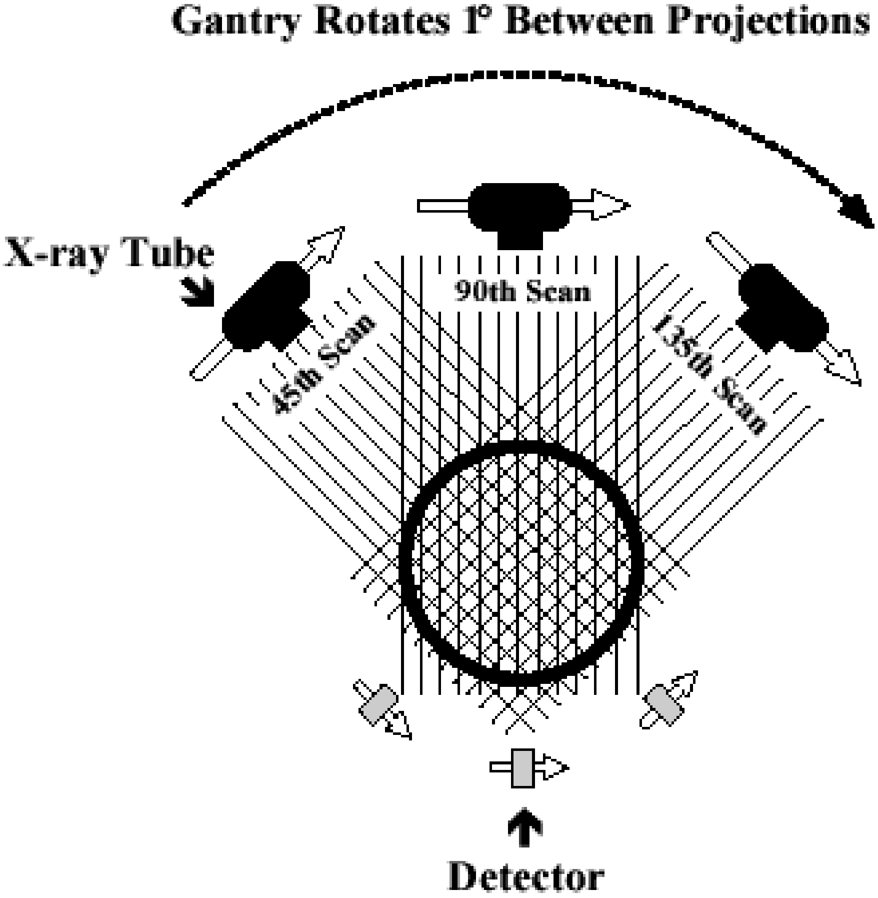

Figure 1.1: First-generation CT scanner. At each angle, the source and detector move together in a line to acquire a series of pencil beam projections at that angle. The source and detector then rotate one degree around the object before repeating this process.

The algorithms for reconstructing the tomographic image from these x-ray projections at different angles evolved concurrently with the different iterations of CT-scanner hardware. The projection data acquired from the first-generation scanner was necessarily digitized as the reconstructed image was computed by solving a linear system of equations, now known as algebraic reconstruction technique (ART) [28]. Though Radon's theories that provide the basis for some of the analytic-based reconstruction algorithms were known at the time, the necessary computer hardware needed for a practical implementation had yet to be developed when Cormack and Hounsfield reconstructed their first CT image [7].

Though the first-generation CT system was a groundbreaking achievement, the rasterized scanning of the pencil beam at multiple angles required approximately 4.5 minutes to acquire the projection information to reconstruct a single two-dimensional (2D) slice of the scanned object [28]. Long scan times are problematic as they increase the possibility of motion during scanning which creates motion contamination artifacts in the reconstruction. The second generation of CT scanners significantly reduced this acquisition time to about 30 seconds by replacing the pencil beam of x-rays with a fan beam and a detector array with approximately 30 detector elements. This new design, shown in Figure (1.2), still required the source and detector to acquire projections using a linear translation before rotating to a new angular position and repeating the process [7].

One of the most important factors driving the hardware development in CT-scanner technology was the issue of acquisition speed. As the reconstruction framework used a forward model that assumes the projections are acquired from a stationary object, the first two generations were only successful in imaging parts of the patient that were relatively stationary. As such, these early scanners were initially only used with the cranium as it is relatively motionless relative to the required acquisition time. Unlike the cranium, other anatomical sites such as the thorax and abdomen are greatly affected by cardiac and respiratory motion. The next generation of scanners were designed to reduce the acquisition time to under 20 seconds in order to image a patient's abdomen in a single breath hold [7].

The third generation of CT scanners, shown in Figure (1.3), would soon become the

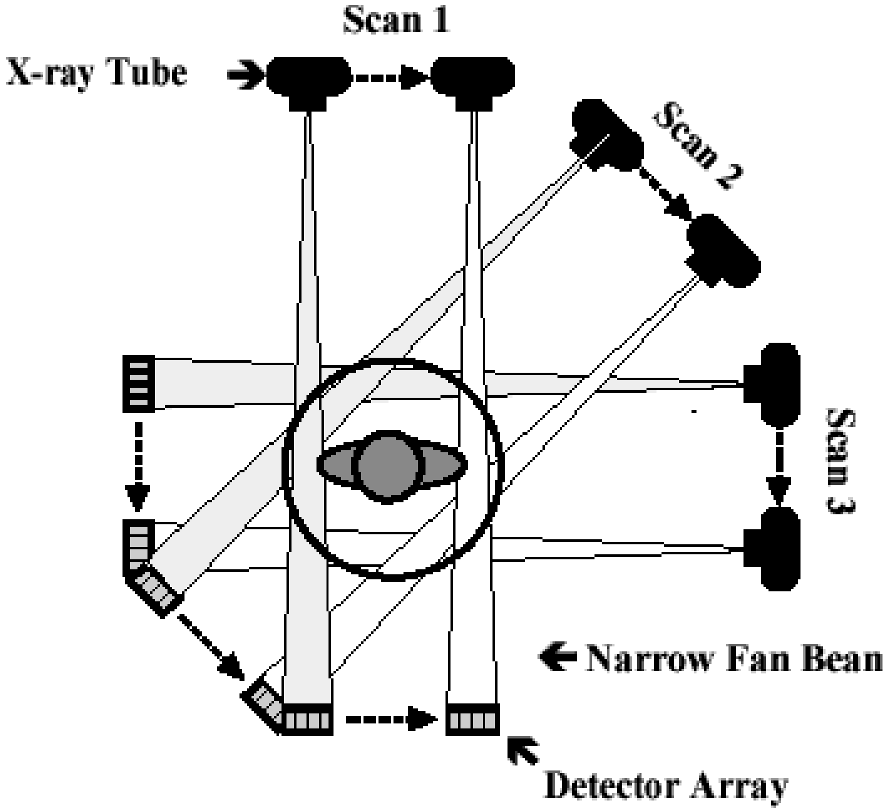

Figure 1.2: Second-generation CT scanner. Though similar to the first-generation scanner in Figure (1.1), a significant reduction in acquisition time was achieved by replacing the pencil beam and single detector with a fan beam and an array of detector elements. The acquistion method remained the same in that the source and detector first acquired multiple projections via a linear translation before rotating to a new angular position and repeating the translation.

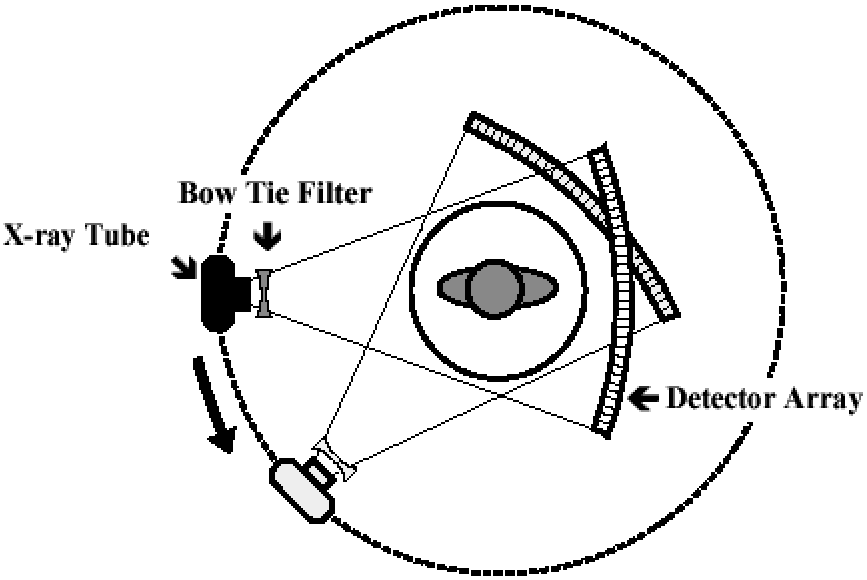

Figure 1.3: Third-generation CT scanner. This design kept the fan-beam x-ray source seen in the second generation of scanners, but the detector size was increased to illuminate the entire patient. This new design no longer required the source and detector to acquire a linear translation before rotating to a new scanning angle. Instead, this generation of scanners simply acquire a single projection at each angle which significantly reduces the acquisition time.

dominant scanner design. This remains true today as most modern diagnostic CT imaging systems, such as the one shown in Figure (1.4), are still based on the third generation design. Unlike the earlier generations of scanners, this design removed the need for the linear translation of the source and detector by increasing the size of the detector so that the entire patient could be illuminated at a given angle. By doing this, it was only necessary to acquire a single projection at each rotation angle which significantly reduced the acquisition time [28].

The evolution from the first generation of scanners to the second and third generations of scanners was enabled by advances in both computer hardware and reconstruction algorithms for solving the inverse problem. As we will further discuss in the following chapter, analytic-based algorithms for solving the CT inverse problem gradually replaced the initial algebraic solution to the linearized forward model used by Cormack and Hounsfield. The most popular form of this implementation is known as filtered-backprojection (FBP) [9, 28].

The FBP approach to CT reconstruction was first implemented as the parallel-beam backprojection algorithm [9]. This provided an analytic inverse to the acquisition method of the first generation of scanners where at a given angle, all of the projections are acquired as parallel incident x-ray beams. However, with the second and third generation of CT scanners, this imaging model was modified from the parallel-beam geometry to the fan-beam geometry to account for the divergent x-ray beam of a point-like x-ray source on an array of x-ray detectors. The new fan-beam FBP algorithm enabled the scanning geometry of the third generation of scanners which are still the backbone of clinical CT today [58].

The fourth generation of CT scanners was developed to eliminate ring artifacts that can appear in the third-generation CT scanners. These ring artifacts can occur when there is a mismatch in projection data of opposing rays along the same line in the patient which can result from misalignment of the moving detector. With a stationary ring of detectors, these ring artifacts are eliminated. However, with the advent of multi-slice detector technology which will be discussed in *Cone-beam CT and new scanning trajectories*, the engineering and

Figure 1.4: Modern Brilliance CT Big Bore scanner (Philips, Amsterdam, NL) which is a third generation multislice scanner with 16 detector rows. The unusually large bore (85 cm diameter) is specifically designed for radiation therapy simulation planning in order to avoid collisions.

cost requirements has led to fourth-generation scanners being phased out [28].

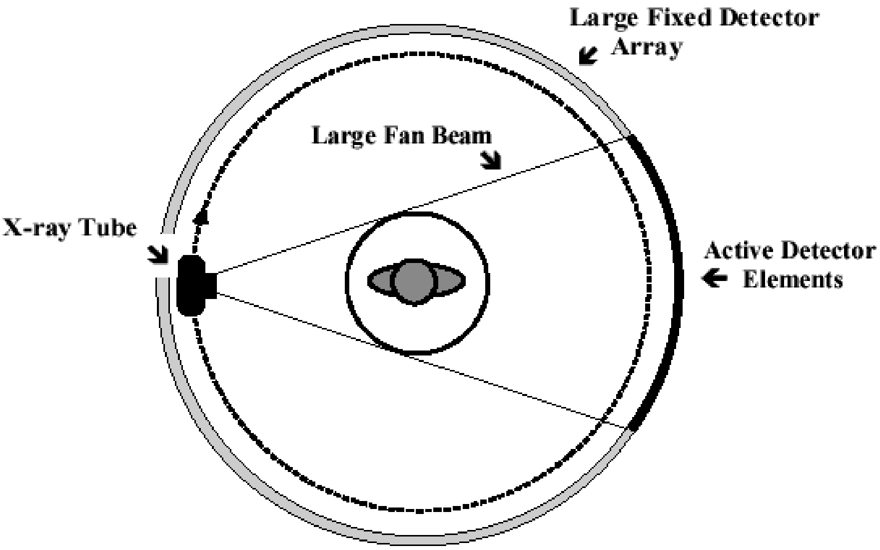

Figure 1.5: Fourth-generation CT scanner. In this design, only the x-ray source rotates inside a ring of fixed detector elements.

The fifth generation of CT scanners, also known as electron-beam, computed-tomography (EBCT) scanners, was developed in the early 1980s for cardiac imaging. In order to acquire the projection data fast enough to "freeze" cardiac motion (20-50 ms for a full rotation), it would be impossible to design a mechanical system that could rotate that quickly and withstand the centripetal force incurred at such high rotational velocity. Instead, this generation was designed to steer the electron beam onto the x-ray anode that was curved around the patient – effectively placing the patient inside the x-ray tube. The design is similar to the fourth generation in that the EBCT scanners have a fixed, partial-ring detector around the patient [7, 28].

Though the fourth and fifth generation scanners are interesting manifestations of CT scanning technology, they are only included here for completeness and will not be discussed further. In the following section, we will look at a major development in reconstruction algorithm technology that cemented the third-generation CT scanner's popularity. This algorithm development enabled the extension of the CT detector's axial coverage allowing for volumetric image acquisition and reconstruction using the third-generation scanner design.

This development also led to the development of a new cone-beam CT (CBCT) geometry which is the focus of this work.

1.2 Cone-beam CT and new scanning trajectories

For all the CT scanners discussed in the previous section *CT development history*, the only scanning trajectory utilized for CT was the circular rotation of the source and detector around the patient. This limitation was due to both the hardware geometry and the reconstruction algorithms that were initially focused on acquiring and reconstructing 2D-planar slices of the object being imaged. Unfortunately, this slice-by-slice acquisition and reconstruction framework was somewhat limiting in acquiring volumetric CT images.

The use of new scanning trajectories to increase the volumetric imaging capabilities of CT began with the development of the spiral or helical CT reconstruction algorithm [35, 41, 37, 40]. By adding longitudinal translation of the patient couch through a third-generation scanner, it was possible to perform a helical trajectory of the source and detector around the patient. This made it possible to rapidly acquire multi-slice (or volumetric) CT of a patient using the existing diagnostic imaging hardware of the third-generation scanners.

Another approach to acquire volumetric tomographic images was to extend the CT detector array in the longitudinal direction by adding additional rows of detector arrays. These multi-array detectors helped to improve the interpolation procedure used for reconstructing the data acquired from a helical scan, and continue to be used in modern third generation CT scanners. As these multi-array detectors began to cover larger extents of the axial field of view (FOV), they eventually led to large flat-panel detector being used to acquire projection information. The flat-panel detector systems are now known as cone-beam CT (CBCT) systems to reflect the cone of x-ray illumination on these detectors as opposed to the fan-beam geometry of the earlier slice-by-slice scanners.

With the advent of CBCT scanners, efforts were made to extend the FBP algorithm to three dimensions (3D) [24, 42, 43, 8]. Though all of these methods attempted to find an analytic inverse to the forward-projection imaging model, they require exact Radon data, which is not provided by the circular trajectory routinely employed by third generation scanners. It was the development of a modified FBP algorithm by Feldkamp, Davis and Kress or FDK [21] (which we will discuss further in *Analytic-based reconstruction*) that made it possible to obtain a useful reconstruction from a circular scanning trajectory on a CBCT system.

1.3 Image-guided radiation therapy

X-ray technology is unique in how rapidly it was applied to the field of medicine following the discovery of x-rays by Wilhelm Röntgen in 1895. The next year in Chicago, Emil Grubbe built his own x-ray device which he began to use for therapeutic purposes [51]. Both diagnostic and therapeutic uses of radiation developed in concert throughout the 20th century culminating in radiation treatment devices that combine low-energy CT imaging or magnetic resonance imaging (MRI) with high-energy treatment beams in image-guide radiation therapy (IGRT). A particularly popular method of delivering therapeutic radiation doses are linear accelerators (LINACs) that deliver powerful megavoltage (MV) treatment beams to diseased tissue.

Though the type of particle and energy spectra of therapeutic radiation will vary depending on both the type and progression of the disease, the desired effect of the prescribed dose is to ablate the diseased tissue by inducing cell death in the cancer cells. Much as with traditional surgical techniques, there is also a simultaneous need to spare the healthy tissue while removing the diseased tissue. In the pursuit of achieving this balance between killing diseased tissue and sparing healthy tissue with the delivered dose, a variety of radiation therapy modalities have been developed.

The initial application of radiation for therapeutic purposes was initially limited to superficial lesions. As great care must be take to ensure the dose is delivered just to the target area, there must be a way to visualize the target of the delivered dose. In the early application of therapeutic radiation, physicians were limited to those pathologies that were externally visible. It was the Swedish neurosurgeon Lars Leksell who conceptualized using a high-energy photon beam to deliver a therapeutic dose deep inside the brain without the additional complications of invasive surgery [45].

The half a century between the discovery of x-rays and the use of them to treat internal structures was the need for imaging technology that made visualizing these internal targets feasible. The development of CT technology discussed in *CT development history* provided the requisite volumetric information that allowed physicians to locate these internal lesions in the patient. This was required in order for the physicians to accurately target the lesions using the high-energy beams proposed by Leksell. He realized by distributing small-field beams around the target, we could create a high-dose deposition at a desired internal target location which led to him and his colleagues producing the GammaKnife in 1968 which consisted of 179 cobalt-60 sources distributed in a hemisphere around the patient's cranium for stereotactic radiosurgery (SRS) [45].

The eventual acceptance of SRS in the United States in 1984 and the subsequent rise in popularity of the technique led to use of linear accelerators for delivering the therapeutic dose rather than the fixed cobalt-60 sources [45]. LINACs were not only able to produce treatment beams that were comparable to those provided the cobalt-60 sources, but they had the additional benefits of being able to produces much higher energy spectra without the need to replace the radiation source as they decayed as cobalt-60 sources. However, despite the tomographic imaging used to plan the prescribed radiation dose, only radiographic projection imaging was used for setting up the patient at the treatment isocenter of these devices.

The addition of a LINAC-mounted, kV-imaging, cone-beam computed tomography (CBCT) system to the gantry-mounted clinical linear accelerator [33, 48, 62] helped this modality become the most popular form of image-guided radiation therapy (IGRT) [80, 5, 17]. The tomographic information provided in the kV energy range improves soft-tissue contrast resolution over that provided by the MV electronic portal imaging device (EPID) alone [32]. The

LINAC-mounted, kV-imaging, CBCT system not only helps with patient setup and target verification, but it also allows the monitoring of the tumor response during treatment [55].

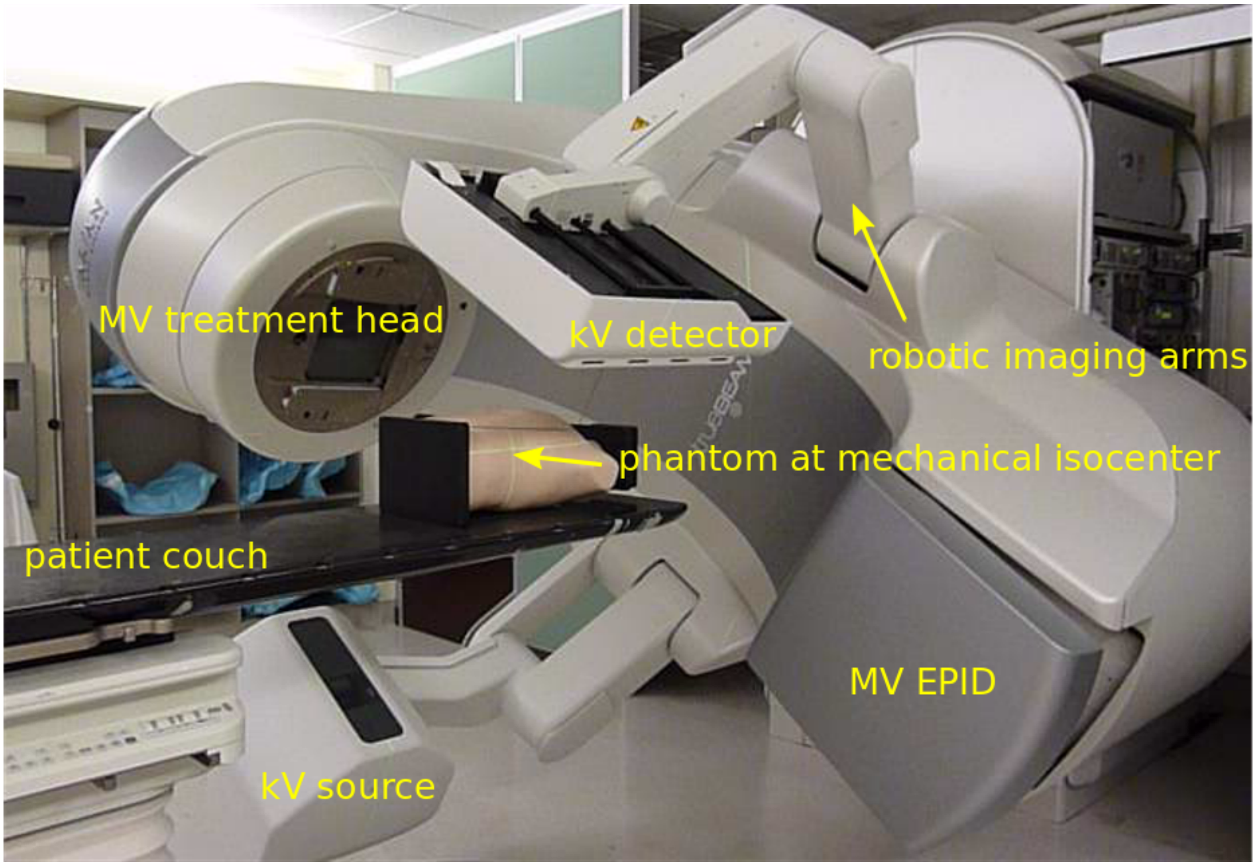

Figure 1.6: Annotated image of a TrueBeam LINAC. See text for description of components.

Figure (1.6) shows an annotated image of a Varian TrueBeam LINAC (Varian Medical Systems, Palo Alto, CA). On the patient couch is the CIRS Torso Phantom (Computerized Imaging Reference Systems, Norfolk, VA) aligned at the mechanical isocenter using the laser guidance system. Above the torso phantom to the left is the MV treatment head with the metallic accessory mount and beam exit window. Below the table to the left is the kV source which provides the kV x-rays for the kV-CBCT imaging system. Above the phantom to the right is the kV detector panel which acquires the projections through the phantom for the kV-CBCT imaging system. Both the kV source and kV detector are mounted on robotic position arms. Below the phantom to the right is the MV electronic portal imaging device, which is retracted in this image, for acquiring MV projections from the MV treatment beam. Finally all of these components are mounted on a rotating gantry which can rotate 360° around the mechanical isocenter for a single rotation. A subsequent rotation must occur in the opposite direction as the gantry lacks the ability to make multiple rotations in the same direction like a diagnostic CT system due to the complexity of the MV LINAC design.

While there are many advantages to using LINAC-mounted CBCT imaging systems for IGRT, there are still technical limitations that negatively impact clinical utility, that could be alleviated by utilizing non-circular scanning trajectories with optimization-based reconstruction. One issue is the limited axial FOV coverage provided by the current detectors and circular scanning trajectory. Another issue is the increased potential of patient collisions with the rotating treatment gantry. In this work, we will focus exclusively on utilizing a generalized optimization-based reconstruction framework from arbitrary CBCT trajectories to address these clinical issues for IGRT. However, the framework itself is not necessarily restricted to IGRT and could be of potential use for a variety of other CBCT applications.

1.4 Organization

In this work, we will discuss an optimization-based, image-reconstruction framework that enables the use of new scanning trajectories. In particular, we will focus on how this approach was developed to address the two clinical shortcomings of limited axial FOV coverage and potential patient collisions with the LINAC gantry. By using these two examples, we will not only show the feasibility of using these non-circular trajectories, but also a potential solution to existing clinical needs.

First, we will discuss the framework and considerations of using optimization-based reconstruction with different scanning trajectories in *Optimization-based algorithms*. Next, we will discuss the need for geometric calibration and discuss a method we developed to accomplish this for these trajectories in *Geometric calibration*. We will then review the use of new trajectories to address the limited axial FOV issue in *Axial field-of-view extension* followed by using these trajectories to alleviate the issue of patient collisions in *Collision-avoiding tra-*

jectories. Finally, we will summarize this work and discuss possible clinical considerations with this methodology in *Summary and conclusions*.

The increased flexibility in choosing different scanning trajectories allowed by optimization-based reconstruction methods provided two solutions to the issues of limited axial FOV coverage and potential patient collisions. For these two problems, we found that the existing limitations could be resolved by using a different scanning configuration. In each case, we proposed a trajectory that would solve the existing problem, and then we evaluated how well the optimization-based reconstructions compared to currently used clinical images.

CHAPTER 2

GENERAL CBCT TRAJECTORY RECONSTRUCTION FRAMEWORK WITH OPTIMIZATION-BASED ALGORITHMS

Through the years of CT research, a fundamental question has always been how to move the source and detector of the imaging system relative to the object to obtain sufficient projection information to reconstruct a useful image. Part of this answer must take into account certain engineering limitations that go into building such a system. However, this is fundamentally a question that must address the requirements of the computational reconstruction algorithm used to assemble the image from the x-ray projections.

There are two main classes of reconstruction algorithms. Analytic-based algorithms, such as FDK [21], represent an approximate solution to the inverse imaging problem, i.e., calculating the object function from its projections. Optimization-based algorithms represent the forward imaging problem as a linear system, and attempt to iteratively invert this system to find an object function that is consistent with the observed projections. Image reconstruction with optimization-based methods provides a robust framework for reconstructing from projections acquired with nonstandard trajectories designed to address specific CBCT limitations as they require no assumptions about the initial scanning trajectory.

The use of optimization-based methods for tomographic image reconstruction is a natural extension of linearizing the x-ray transform imaging model of a tomographic scan. Approaching the image reconstruction problem as a linearized imaging model has existed since the first CT system built by Cormack and Hounsfield. As discussed in the *Introduction*, they utilized the algebraic reconstruction technique (ART) to solve a system of equations created by the summation of the rays through the image pixel grid at each projection angle [27].

Though the initial optimization-based image reconstruction with ART was successful in providing a solution to the inverse problem, the limited computational power available at the time proved to be an intractable limitation. Though the number of unknown variables in the system of equations associated with this 2D reconstruction problem is trivial by today's standards, the lack of parallelization and other engineering limitations of transistors at the time were too onerous for the clinical workflow. This computational complexity was further increased when moving from two-dimension (2D), single-slice images to three-dimensional (3D), volumetric image reconstruction which introduces a greater number of unknowns. However, a recent renaissance of utilizing graphics processing units (GPUs) – technology once solely in the purview of video games – for scientific computation has made optimization-based methods temporally competitive with analytic-based methods [81, 66].

2.1 Background: Cone-beam computed tomography

2.1.1 Analytic-based reconstruction

Analytic-based reconstruction algorithms are formulated by explicitly finding an inverse to the X-ray transform

$$g(\mathbf{r}_0, \hat{\theta}) = \int_0^{\infty} f(\mathbf{r}_0 + t\hat{\theta})dt, \tag{2.1}$$

where the data function g is acquired by integrating along the ray from the source at $\mathbf{r}_0$ in the direction $\hat{\theta}$ through the object function f. In x-ray CT, this object function represents the distribution of the linear attenuation coefficients of the various materials within the object's interior that provide exponential attenuation to the incident beam as it travels through the object as characterized by Beer's law [6].

A fundamental problem with these reconstruction algorithms when practically reconstructing f is the assumption of a continuous-to-continuous (CC) model. These analytic-based reconstruction algorithms impose dense sampling requirements for both the detector and number of views to approximate a continuous data function. Given that the data function from the digital detector and the numerical array for storing the reconstructed image are both discrete, a more natural approach to the inverse problem would be a discrete-to-discrete

(DD) imaging model [1].

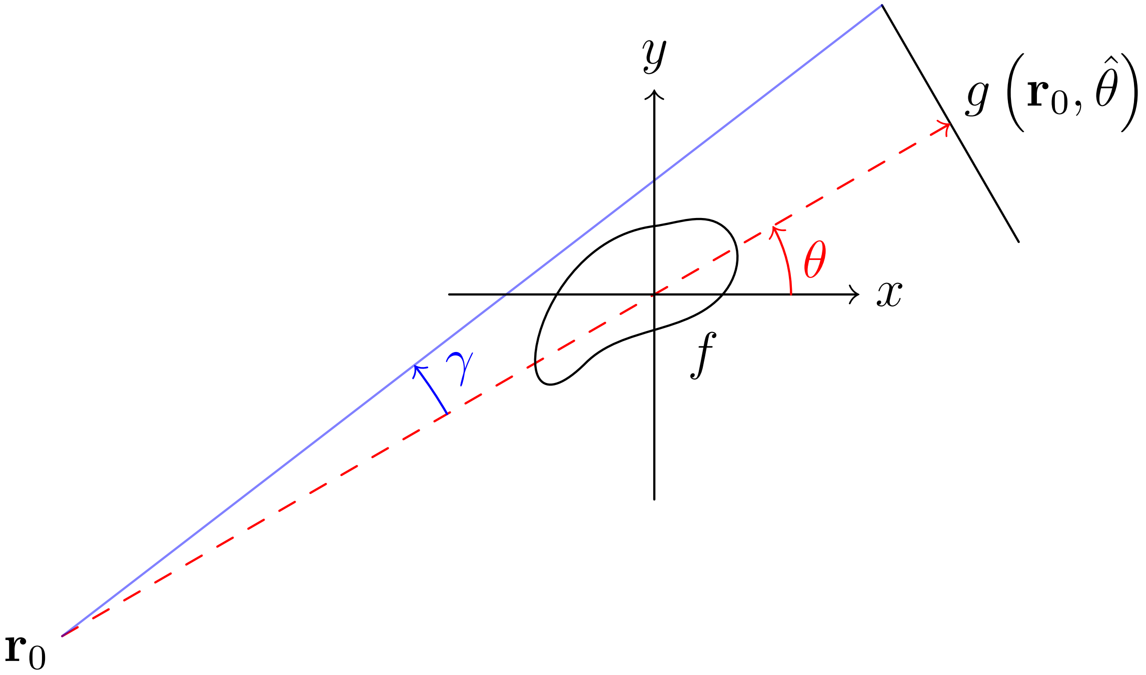

Figure 2.1: Single-view schematic of the x-ray transform of an object f from an x-ray source at $\mathbf{r}_0$ illuminating the detector in the direction of $\hat{\theta}$ to produce the detector response $g\left(\mathbf{r}_0, \hat{\theta}\right)$. The angle γ is the maximum cone-angle of this CBCT as determined by the detector size. The source and detector geometry is that of Varian's TrueBeam kV-imaging system.

In the 1980s, work was done to directly solve the inverse problem for the cone-beam geometry [60, 22]. By modeling the projection formation process as a Radon transform or an X-ray transform, reconstruction algorithms were formulated by finding an analytic-based inverse to the transform. However, for the inverse to be exact, it needed to meet strict requirements such as Tuy's condition which states that every plane through the object must intersect the source trajectory [76]. Though there are non-circular trajectories such as the infinite-line trajectory which satisfy Tuy's condition, the application of such trajectories for real scanning configurations are always approximations [72] which fail to satisfy the requisite geometry to provide an exact inverse.

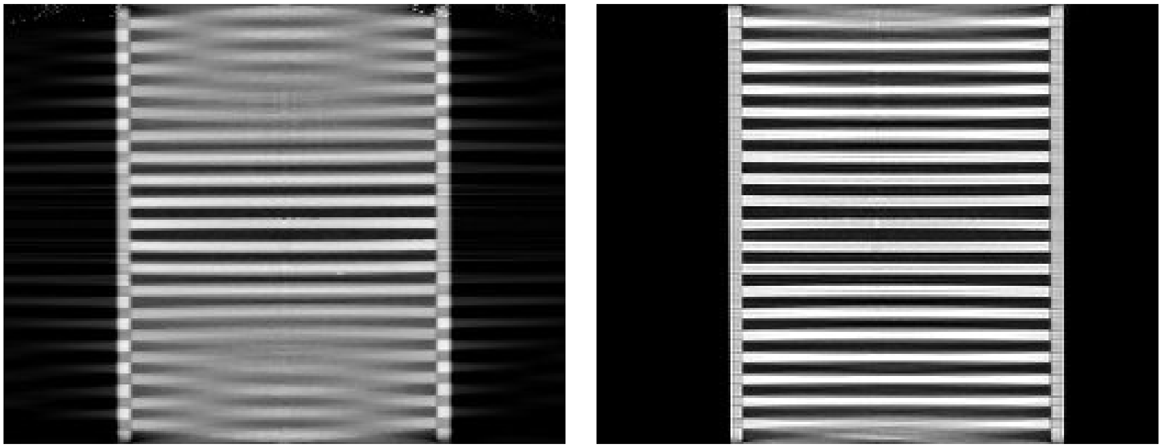
(a) (b)

Figure 2.2: Simulated example of cone-angle artifacts seen in the sagittal view of a reconstructed Defrise-style phantom. On the left is an FDK reconstruction, and on the right is an MLEM reconstruction (200 iterations). Such a phantom design of alternating high-contrast densities along the longitudinal direction is explicitly identified by the FDK authors as being a case where their assumptions breakdown at larger cone angles. In the middle of image that corresponds to the plane of the source orbit, the sharp boundaries between the alternating disks can be seen. However at the edges of the image, corresponding to larger cone angles, the breakdown of these assumptions and the cone-angle artifacts produced can be seen. The cone-angle artifacts at the larger cone angles are less severe in the optimization-based reconstruction ([0, 0.3] cm^{-1} display window).

The circular scanning trajectory that is ubiquitous in the clinic for CBCT is one trajectory that fails to meet Tuy's condition. The most popular reconstruction algorithm for the circular CBCT trajectory is the filtered-backprojection (FBP) algorithm proposed by Feldkamp, Davis, and Kress (FDK) [21] which is still the industry standard. FDK is only an exact inversion to the Radon transform on the midplane containing the circular source trajectory. For transaxial planes other than the midplane, a quasi-redundancy in the scanning data is assumed. It is the violation of this assumption which leads to cone-angle artifacts, an example of which is shown in Figure (2.2a). These artifacts become more severe at larger cone angles (the angle γ in Figure (2.1)) where this assumption is less applicable.

The presence of cone-angle artifacts in FDK reconstructions from the incomplete data acquired with circular scanning trajectories led to research into inverse algorithms for cone-beam scans from theoretically complete trajectories such as a circle plus a line [83]. It became apparent in the reconstruction results that implementing these direct reconstruction algorithms did not produce the anticipated results [42]. Severe artifacts and numerical errors were found in the reconstructions due to factors such as truncation introducing high-frequency components that are amplified in the filtration process.

2.1.2 Optimization-based reconstruction

Analytic-based reconstruction algorithms are problematic in that they require a fixed scanning trajectory to formulate the inverse. When approximations are made for the inverse, as in FDK, deviations from these approximations lead to inconsistencies in the model and subsequently artifacts in the reconstruction such as the cone-angle artifacts shown in Figure (2.2a). In contrast, optimization-based reconstruction algorithms represent a more robust model of the image formation process [68, 26, 70, 69, 3]. As Figure (2.2b) shows, this can help reduce artifacts such as the cone-angle artifacts.

Optimization-based reconstruction algorithms provide a more accurate model of the DD imaging system that comprises both the digitized projection images from the kV-imaging detector and the digitized tomographic image calculated by the reconstruction program. The X-ray transform of the object function can be represented as the linear system

$$\mathbf{g} = \mathcal{H}\mathbf{f}, \tag{2.2}$$

where $\mathbf{g}$ is the discrete M pixel sampled projection on the detector, $\mathcal{H}$ is the $M \times N$ discrete form of the X-ray transform, and $\mathbf{f}$ is the object function represented on a N voxel basis. As direct inversion of $\mathcal{H}$ is impractical due to both its size and inconsistencies from factors such as noise, optimization techniques are used to solve this system for an estimate of the object $\mathbf{f}^*$.

The optimization problem is formulated as an objective function based on the actual data $\mathbf{g}$ and the image model $\mathcal{H}\mathbf{f}$. An optimization algorithm is then used to iteratively update the estimate of $\mathbf{f}^*$ until a suitable convergence criterion has been met. The parameters of the optimization problem, the optimization algorithm, and the convergence criteria are all important factors in determining the properties of the reconstructed image and subsequently its utility. When the reconstruction program is not run to convergence, a parameter such as the number of iterations can be fixed provided justification is given for the choice of iterations.

In selecting the parameters for the reconstruction program, consideration must be given to the impact each parameter will have on the reconstructed image quality. As we investigated using optimization-based reconstruction for non-circular scanning trajectories, we selected parameters of our reconstruction program to mimic the relevant clinically-utilized parameters where applicable. For instance, our reconstruction resolution sizes are chosen to provide the same voxel sizes used by the clinical reconstruction software. However, these parameter choices are made only to provide comparisons to the current clinical image quality. This does not mean that these values are optimally selected, and for any clinically relevant evaluation, rigorous parameter optimization must be studied for the clinical imaging task [49, 79].

Previous work has shown that optimization-basaed algorithms can reconstruct clinically useful images under scanning conditions for which analytic-based FDK fails [26, 71, 69]. In applying optimization-based reconstruction to non-circular trajectories, we focus primarily on the well-understood maximum-likelihood expectation maximization (MLEM) [68, 18]. Though a variety of optimization-based reconstruction programs exist, we used the MLEM program to limit the number of parameters introduced by the reconstruction program, since new scanning trajectories already introduce additional parameters that impact the projection data and resulting tomographic reconstruction.

2.2 Background: Scanning trajectories

2.2.1 Standard Trajectories

In IGRT, LINAC-mounted CBCT imaging systems such as Varian's TrueBeam kV-imaging system now routinely provide patient image information. These images are used to check the patient alignment before delivering the radiation treatment. The circular rotation of the LINAC gantry defines the acquisition trajectory for the CBCT scan. While such a scanning trajectory provides sufficient information for an analytic-based reconstruction of the scan volume, there are a variety of limitations that arise from this work flow.

Due to engineering and cost restrictions, the kV detector has a limited size. The TrueBeam system has a transaxial width of 40 cm and an axial height of 30 cm. This restricts the FOV that can be imaged in a traditional circular scan. While the offset detector technique [4, 12] is commonly used to increase the transaxial FOV (for a 1.5X magnification, this is an increase in FOV diameter from 26.7 cm to 44.0 cm on the TrueBeam system with a 13 cm offset), the axial coverage is still very limited (20 cm for the same TrueBeam geometry) [61]. The reason that the limited FOV has not been addressed by increasing the detector size is partially due to the industry's reliance on the approximate FDK algorithm [58]. As shown in Figure (2.2), as the cone angle increases, artifacts near the end of the axial FOV become more severe.

Another problem with the current circular imaging trajectory is the potential for LINAC collisions with the patient [29, 52]. Cases arise when the patient is positioned in the treatment position, a CBCT image cannot be acquired due to part of the patient being in the path of the LINAC's trajectory (i.e., gantry clearance cannot be achieved). As the current FDK algorithm requires a trajectory with sufficient angular coverage, the patient must be moved to a position where the gantry can make an uninterrupted rotation around the patient. These workarounds can incur significant temporal costs in re-positioning the patient on the treatment couch for a new collision-avoiding setup. A robust scanning modality that could avoid these collision zones while providing sufficient tomographic information would alleviate these expensive re-positioning occurrences.

In both of these examples, the default circular trajectory prescribed by FDK is inadequate for obtaining the desired tomographic information. Furthermore, the disruption to the clinical workflow created by these limitations introduces bottlenecks into clinical efficiency which affects both the clinical staff as well as the patient's comfort in the procedure. In the case of a potential patient collision, the inability to acquire the required trajectory can even result in forgoing the CBCT image. For these particular examples, we investigated ways in which new trajectories enabled by optimization-based reconstruction could alleviate the limitations imposed by the standard circular scan.

2.2.2 General trajectories

Though there has been previous work in developing analytic methods for addressing the reconstruction from some novel trajectories [37, 38, 39, 36], it could be clinically useful to enable reconstruction from an arbitrary, collision-avoiding trajectory. As the collision region (if one arises) is contingent on the patient's size and treatment position, the imaging trajectory would vary on a per patient basis. As such, deriving the analytic inverse for each patient's scanning trajectory would be impractical.

Optimization-based reconstruction provides a generalized framework enabling greater flexibility in reconstructing from projections acquired with non-circular trajectories. Provided the geometry of each view is correctly incorporated into the system matrix $\mathcal{H}$ in Equation (2.2), clinically useful reconstructions can be obtained from acquisitions for which an analytic inverse may not be available. This robust approach enables tomographic imaging from collision-avoiding trajectories that would accommodate the patient's specific needs.

For the problem of the limited axial coverage, the current clinical method of extending the FOV is to acquire two circular scans at different axial positions and reconstruct each circle independently using FDK before stacking the two volumes together [23]. Unfortunately, the

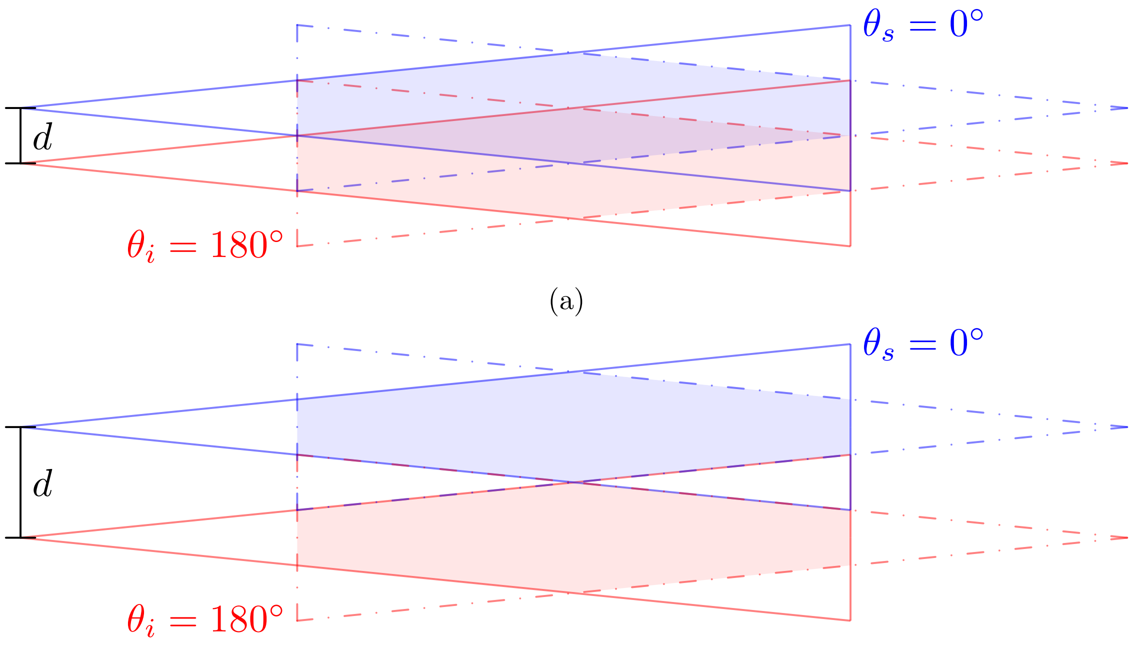

(a)

(b)

Figure 2.3: Schematic illustrating the axial coverage provided by stacking two circular FDK reconstructions together for the TrueBeam kV imaging system. In each figure, the top portion corresponds to the projective geometry of the superior circle (blue), and the bottom portion corresponds to that of the inferior circle (red). For both the inferior and superior circles, two projective views are illustrated as opposing projective views at $\theta = 0^\circ$ (solid lines) and $\theta = 180^\circ$ (dashed lines). The shaded regions corresponds to the image support of an FDK reconstruction of the respective circle. The top figure (a) represents an axial separation between the two circles ($d = 10$ cm) where the support volumes overlap (purple). The bottom figure (b) shows the maximum axial separation ($d = 20$ cm) for which the two support volumes are contiguous though they share no redundancy in the reconstructed volumes.

increased distortion from cone-angle artifacts at large cone angles limits the axial separation between these two circles illustrated in blue and red in Figure (2.3). In addition limitations incurred by the failure in the FDK approximation at larger cone angles, there is an additional limitation that the support, or volume of the image space that can be reconstructed, allowed by analytic-based methods is restricted to the shaded regions of Figure (2.3).

The use of the two circles alone provides one interesting example of a trajectory where optimization-based reconstruction provides an advantage to the stacked-FDK method currently used. Unlike stacking two separate reconstructions together, it is possible to reconstruct the entire volume at once provided the system matrix is correctly calculated to reflect the acquisition of two circles in planes located at different axial positions relative to the patient. In addition to the reduced cone-angle artifacts already seen in optimization-based methods, reconstructing both volumes together provides additional information about the overlapping region between the circles that further helps to reduce the cone-angle artifacts.

In addition to improving the use of the two circles, the optimization-based framework allows for noncircular trajectories. Given that there needs to be a relative axial translation between the kV-imaging system and the patient, we investigated if there were any advantages to acquiring some projection views during the axial translation. Such trajectories that included an axial translational stage have been studied before and have the potential to further reduce the impact of cone-angle artifacts with both analtyic-based [83, 53, 34, 38] and optimization-based methods [15].

In the case of potential patient collisions with the LINAC gantry, a simple change in the scanning trajectory could be sufficient to prevent a collision. Much like the extended axial FOV case, optimization-based reconstruction is able to handle variations in the acquisition trajectory provided it is accurately reflected in the system matrix. As such, there are two different ways we studied where the scanning trajectory could be modified to avoid a collision.

If the patient collision were to occur with the kV detector (the closest component of the CBCT system to the patient), one possible way to avoid that collision would be to move the kV detector away from the patient at the collision region. Since the detector is mounted on a robotic arm, it should be possible to move the detector outward from the isocenter radially, increasing the diameter of both the collision-free region and of the scanning trajectory. This effectively changes the magnification for that region, but the reconstruction framework is able to reconstruct from all the views at both magnifications provided that everything is accurately modeled in the reconstruction problem.

The other trajectory modification that could solve this problem would be to move the patient. As with the change in magnification, the change in the patient position does not prevent reconstruction with the optimization-based methods provided the patient motion is correctly incorporated into the system matrix $\mathcal{H}$. Moving the patient also provides a solution to avoid potential patient collisions that occur with the LINAC treatment head. The MV treatment head on Varian's TrueBeam system is actually closer to the patient than the kV detector. Unlike the kV detector, it is not possible to change the position of the treatment head. In this case, moving the patient would be the only viable trajectory modification to avoid a collision.

2.3 Generalized trajectory framework

To find an estimate of the object $\mathbf{f}^*$ as an approximate solution to Equation (2.2), we choose a reconstruction program that can be solved with the well-understood maximum-likelihood expectation maximization (MLEM) algorithm [18]. Here, our reconstruction program is formulated as

$$\mathbf{f}^* = \text{argmin} D_{KL}\left(\mathbf{f}\right) \tag{2.3}$$

where $D_{KL}(\mathbf{f})$ is the Kullback-Leibler (KL) divergence between $\mathbf{g}$ and $\mathcal{H}\mathbf{f}$ which is calculated as

$$D_{KL} = \sum_{i=1}^{M} g_i - \widetilde{g}_i + g_i \ln\left(\frac{\widetilde{g}_i}{g_i}\right) \tag{2.4}$$

where $\widetilde{g} = \mathcal{H}f$ [44, 1]. The KL divergence or relative entropy is minimized with the MLEM algorithm

$$f_j^{(n+1)} = \frac{f_j^{(n)}}{\sum_{i=1}^{M} \mathcal{H}_{ij}} \sum_{i=1}^{M} \mathcal{H}_{ij} \frac{g_i}{\sum_{j=1}^{N} \mathcal{H}_{ij} f_j^{(n)}} \tag{2.5}$$

where f_j^n is $j-$th voxel value at iteration n and $\mathcal{H}_{ij}$ is the element of the system matrix at the $i-$th row and $j-$th column for $i = 1, 2, ..., M$ and $j = 1, 2, ..., N$. The initial image estimate for the reconstructions was $\mathbf{f}^{(0)} = 1$.

We define a scanning trajectory as the sequence of source and detector positions used to acquire each projection view. For all of the trajectories we studied, the detector moves in diametric opposition to the kV-imaging source though this is not a requirement of this formulation. The coordinates of the trajectory are then defined relative to a fixed origin in the patient. In a traditional scanning configuration where the patient is stationary, the system matrix $\mathcal{H}_{ij}$ projects the object $\mathbf{f}$ from image space to the data space of $\mathbf{g}$. When this is the case, it is sufficient that the coordinate basis of the image space coincides with the room coordinate system, or is at least stationary relative to it. From each projection view acquired from the TrueBeam system, we extracted the position information of the CBCT imaging arms and subsequently built $\mathcal{H}_{ij}$ as the projective transform from image space in the room coordinate system to the data space of the kV detector.

When the patient is no longer fixed relative to the room-coordinate system, (e.g. moving the treatment couch as the gantry rotates), the image space ($\mathbf{f}_{\text{patient}}$) is moving relative to the room coordinate system for each projection view. As such, a change of basis for the columns space of $\mathcal{H}$ is necessary so that the new system matrix represents a transform from the image space of the patient to the data space of the detector represented as $\mathcal{H}'$. As the acquisition system also reports the couch position, we used this to build the required transformation matrix $\mathcal{T}_{\text{IEC,patient}}$ for each projection view. The imaging model in Equation (2.6) then becomes

$$\mathbf{g} = \mathcal{H}'\mathbf{f}_{\text{patient}}, \tag{2.6}$$

where

$$\mathcal{H}' = \mathcal{H}\mathcal{T}_{\text{IEC,patient}}. \tag{2.7}$$

Once the change of basis is accounted for, the reconstruction program in Equation (2.4) can be reformulated with $\mathbf{f}_{\text{patient}}$ instead of $\mathbf{f}$ and solved with the MLEM algorithm in Equation (2.5) using $\mathcal{H}'$ instead of $\mathcal{H}$.

2.4 Framework implementation with Varian TrueBeam kV-CBCT system

2.4.1 TrueBeam LINAC with Developer Mode

Table 2.1: Subset of Varian's TrueBeam projection header variables pertaining to the kV-imaging system.

	Couch	Detector	Gantry	kV Source
Acquisition	CouchLat CouchLng CouchRtn CouchThickness CouchVrt CouchWidth	ImagerLat ImagerLng ImagerOrigin ImagerResX ImagerResY ImagerSizeX ImagerSizeY ScatterGrid	GantryAcceleration StartAngle StopAngle	Current FrameRate KVFilter PulseLength SAD SID Voltage
Projection	CouchLat CouchLng CouchRtn CouchVrt	ImagerDeltaLat ImagerDeltaLng ImagerDeltaPitch ImagerDeltaRtn ImagerDeltaVrt	GantryRtn	SourceAngle SourceDeltaLat SourceDeltaLng SourceDeltaVrt

To study these trajectories on a clinical, kV-imaging system, we implemented some of them on Varian's TrueBeam system. The TrueBeam Developer Mode provides control of the kV imaging system to allow for motion control that is unavailable in clinical modes. Developer Mode provides a scriptable control interface that allows control of the gantry rotation, the kV-imaging arms, as well as the position of the treatment couch. By combining motions with all of these components, it is possible to acquire kV projection data from a variety of different interesting motions. From the acquisition, each projection is returned with self-reported nominal values that can be used to build the reconstruction system matrix. Table (2.1) shows a subset of these header variables pertaining to the kV imaging system.

The TrueBeam's kV imaging system is illustrated in Figure (1.6) in addition to the gantry, couch, and robotic arms that can all be utilized to implement these trajectories. The kV-imaging system itself consists of a Varian kV x-ray source (GS-1542) and a 39.7 cm x 29.8 cm amorphous silicon flat-panel detector (PaxScan 4030CB) with a 2048×1536 pixel array that performs a 2×2 binning for a readout of 1024×768 square pixels of effective size 0.388 mm. The source and detector are mounted on robotic arms with the kV beam direction orthogonal to the MV treatment beam.

2.4.2 Varian coordinates

Once the scanning trajectory has been completed, the view-by-view geometry reported in the projection headers shown in Table (2.1) must then be transformed so that it describes the projection information in the desired image-space basis. In the case of IGRT, the image-basis of interest to physicians is that of the patient. As discussed, this requires calculating the correct transform $\mathcal{T}_{\text{IEC,patient}}$ so that the system matrix for reconstructing into the image space $\left(\mathcal{H}'\right)$ as described in Equation (2.6) can be found.

The first coordinate system shown in Figure (2.4) is the radiation coordinate system; a basis in which the projection headers describe the projective geometry of the source onto the detector at each view. In this convention, the detector pixels can be converted into the physical units to describe their location relative to the source at each projection. As the source and detector rotate together with the gantry, this basis ignores the gantry rotation angle $\left(\theta_g\right)$ at each view.

However, in order to determine the relationship of each projection to the other views, this radiation coordinate system must be transformed into a global coordinate system describing the ensemble of projections relative to the image space. The global coordinate system

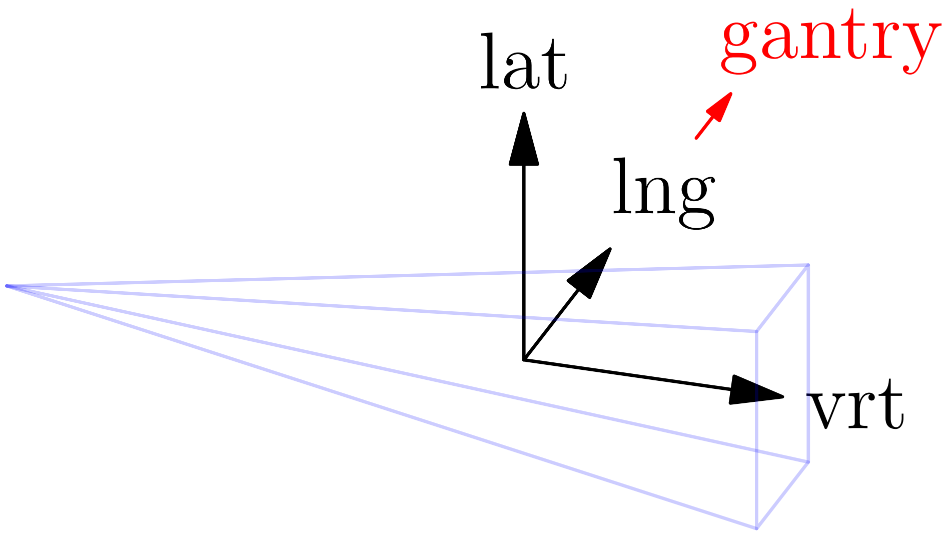

Figure 2.4: Radiation coordinate system which is the basis of the projection geometry reported in the projection headers. This coordinate system provides a description of the source position relative to the detector bins with the origin at the imaging isocenter of that view. Though this basis is agnostic of the gantry rotation, the red arrow points into the gantry (into the page here in the same direction as the longitudinal bases (lng)) for reference in images showing the other bases used in this transform.

describing the TrueBeam room geometry is the International Electrotechnical Commission (IEC) 61217 coordinate system shown in Figure (2.5). This coordinate system is designated by the IEC as the standard coordinate system for radiotherapy machines [31].

For a gantry angle of $\theta_g = 0°$, the radiation-coordinate system shown in Figure (2.4) has the same basis as the radiation coordinate system in Figure (2.4). This can be used to place the view-by-view header information into the IEC basis ignoring the gantry rotation initially. Using the IEC basis vectors X_{IEC}, Y_{IEC}, and Z_{IEC} shown in Figure (2.4), the source and detector positions for that view in homogeneous coordinates are then

$$\boldsymbol{r}_{\text{src,rad}} = \begin{bmatrix} \text{SourceVrt} \\ \text{SourceLng} \\ \text{SourceLat} \\ 1 \end{bmatrix}, \tag{2.8}$$

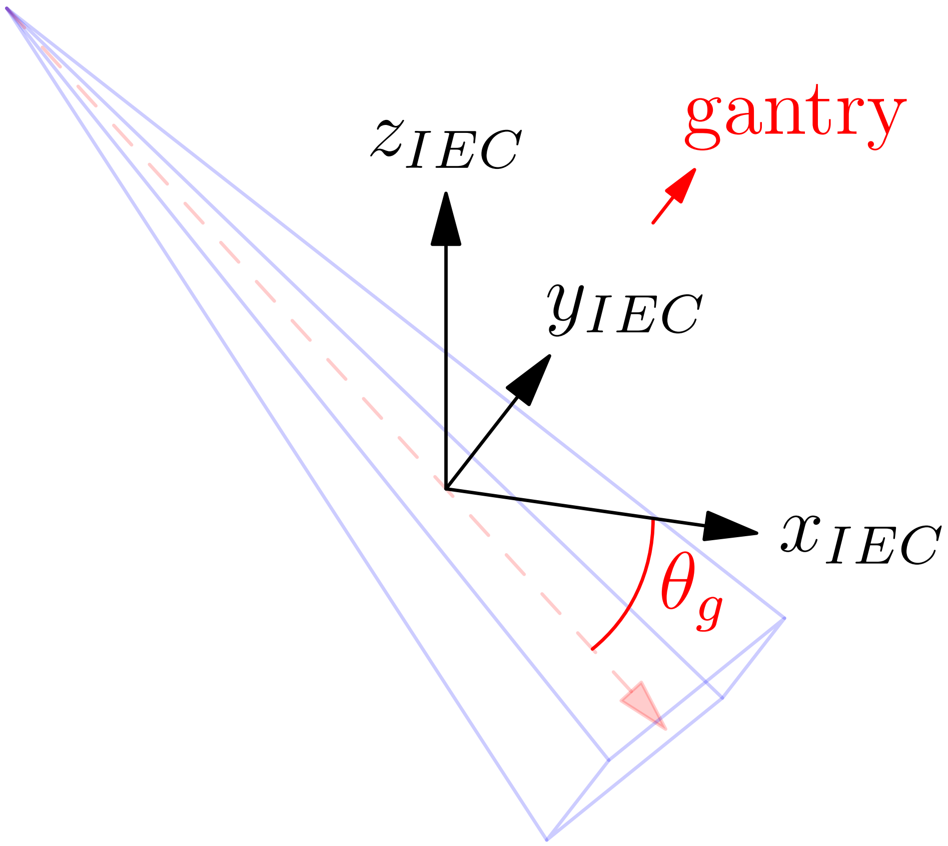

Figure 2.5: the IEC coordinate system that is the global-basis for all the LINAC geometry. To transform the data in the radiation coordinate system into the IEC coordinate system, the gantry rotation angle is used to rotate each view in the radiation-coordinate basis into the global room coordinates. For a gantry angle of $\theta_g = 0°$, the radiation-coordinate system in Figure (2.4) is the same as the IEC.

and

$$\boldsymbol{r}_{\text{det,rad}} = \begin{bmatrix} \text{ImagerVrt} \\ \text{ImagerLng} \\ \text{ImagerLat} \\ 1 \end{bmatrix}, \tag{2.9}$$

respectively.

To then get these source and position vectors into the correct IEC position, they are transformed via a rotation around the longitudinal or y_{IEC} axis by the gantry angle θ_g which is

$$\mathcal{R}\left(\theta_g\right) = \begin{bmatrix} \cos\left(\theta_g\right) & 0 & \sin\left(\theta_g\right) & 0 \\ 0 & 1 & 0 & 0 \\ \text{-}\sin\left(\theta_g\right) & 0 & \cos\left(\theta_g\right) & 0 \\ 0 & 0 & 0 & 0 \end{bmatrix}. \tag{2.10}$$

By then applying this transform to each projection view geometry in the radiation coordinate system, we then have

$$\boldsymbol{r}_{\text{src,IEC}} = \mathcal{R}\left(\theta_g\right) \boldsymbol{r}_{\text{src,rad}} \tag{2.11}$$

and

$$\boldsymbol{r}_{\text{det,IEC}} = \mathcal{R}\left(\theta_g\right) \boldsymbol{r}_{\text{det,rad}} \tag{2.12}$$

which are the view-by-view projection geometry in the IEC basis.

At this point, the system matrix ($\mathcal{H}$) will reconstruct into the global IEC room coordinates. In the event that this is a traditional scanning trajectory where the patient or object stays at the imaging isocenter, this geometry would be sufficient for performing a reconstruction. However, to then allow for trajectories where this fixed isocenter is no longer a requirement, we must perform one more transform the projection geometry to the basis of the patient.

To scan a patient with a trajectory where either the imaging object or the isocenter

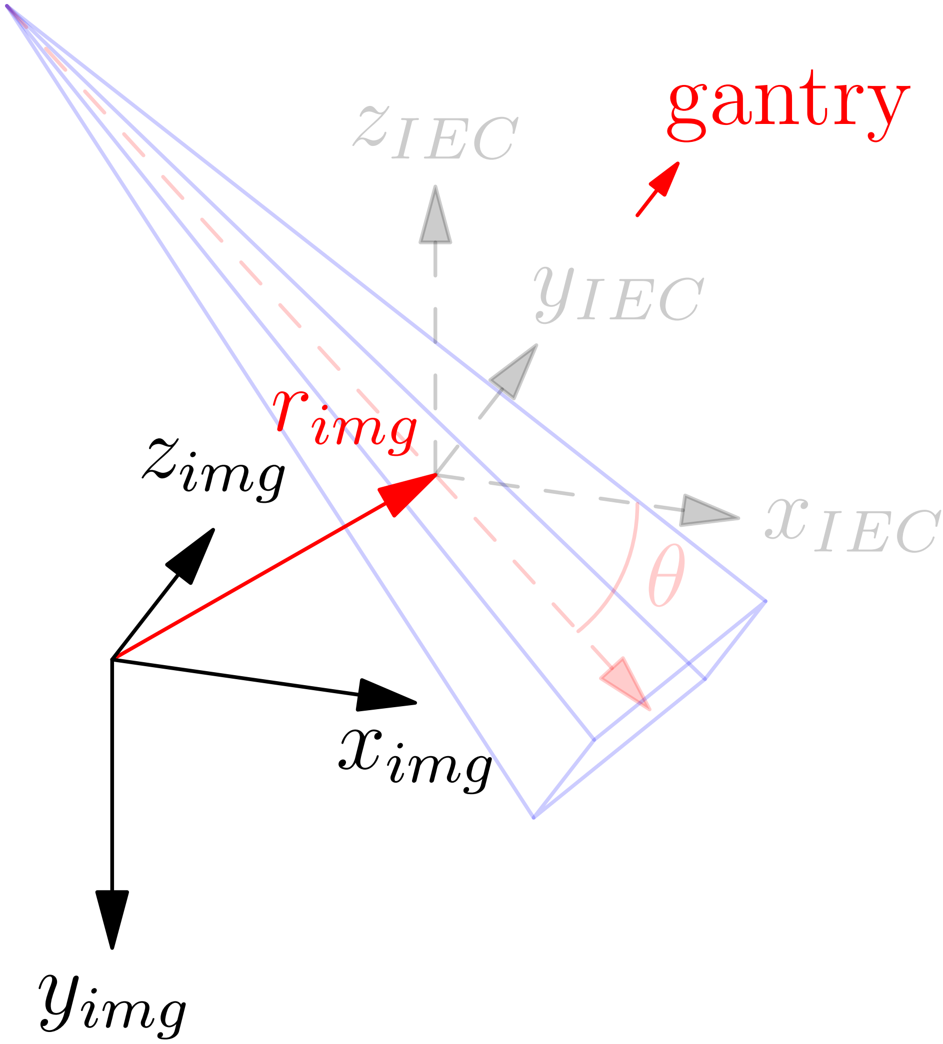

Figure 2.6: The image or patient coordinate system that will be used as the basis for the reconstruction system matrix $\mathcal{H}$ in Equation (2.6). By using the view-by-view transform enabled by optimization-based methods, this can incorporates the relative motion of the imaging source and detector as well as the motion of the couch and gantry relative to the point of interest in the patient dentoted by $\boldsymbol{r}_{img}$

.

itself are changing relative to each other during a scan, it is then necessary to make an additional transform the projection geometry into the basis of desired image space. Again, for IGRT, this is the image space of the patient's treatment volume whose basis vectors are schematically depicted in Figure (2.6).

As an example of this, Figure (2.6) illustrates one view where there is a translation vector ($\boldsymbol{r}_{\text{img}}$) denoting a transformation of the patient's imaging isocenter away from the mechanical isocenter of the imaging system. If this offset can be determined for each projection view, the detector data can be transformed into the basis of the patient's imaging volume. Though this transform need not be limited to translation, the form presented here would then involve a final transform of the form

$$\mathcal{T}_{\text{img,IEC}}\left(\theta_g\right) = \begin{bmatrix} 1 & 0 & 0 & -r_{x,IEC} \\ 0 & 1 & 0 & -r_{y,IEC} \\ 0 & 0 & 1 & -r_{z,IEC} \\ 0 & 0 & 0 & 0 \end{bmatrix}, \tag{2.13}$$

and the requisite transform of the system matrix would then be the necessary transfrom $\mathcal{T}_{\text{IEC,patient}}$ needed to reconstruct from view-by-view shifts of the image object and the imaging system into the fixed coordinate system of the patient's image space.

As we will show in the following chapters, this framework provides a very robust way to handle a variety of non-circular trajectories that have such shifts between the imaging system and the object. In our work the TrueBeam system, these shifts could arise from motion of the imaging arms relative to the patient, motion of the patient table, or even simultaneous motion of both.

2.5 Metric Evaluation

Though we by no means wish to suggest that this framework is limited to a particular hardware implementation, or even simply to the purview of IGRT alone, the TrueBeam system and the practical issues that currently face the clinic with its use motivated this investigation. As we present this as a potential solution to some of the limitations in the clinic, we must demonstrate that in bringing the benefits of these new trajectories, we are not adversely impacting the subsequent image quality. We emphasize that image quality alone cannot ultimately determine the true value of any particular imaging modality or technique.

It is imperative that for any translation of novel technology to a clinical setting to occur, rigorous clinical studies must be performed to determine the true impact any technology has on the real metric of performance which is the task-based utility. How that is defined is itself a challenging component in any field, but in medicine this must be given consideration to the patient outcome.

Image quality is itself one component of the myriad factors that must be considered when evaluating a clinical technique. As we discuss this framework of reconstructing from non-circular trajectories with optimization-based reconstruction, we will use image quality as a surrogate for clinical utility. Though the trajectories we will look at were formulated to address practical limitations of the current state of the art, the benefits to the clinical workflow must eventually be evaluated with the ultimate patient outcome. What we do posit is that if the framework can achieve reconstructions with image quality that is comparable to existing techniques that have already met the stringent clinical evaluation criteria, then the additional benefits allowed by the non-circular trajectories truly do have the potential to improve clinical utility.

As we look at some examples of different scanning trajectories that could be beneficial to the IGRT clinical workflow, we will use some of the following image quality metrics to compare reconstructions using this framework to the images of existing clinical techniques. We have attempted to select metrics based on existing clinical phantoms and image quality phantoms so as to reflect the potential image quality of these methods were they to be used clinically. Though some of the uses cases provide scanning configurations for which clinical image quality phantoms do not exist, we tried to use phantoms with direct clinical relevance.

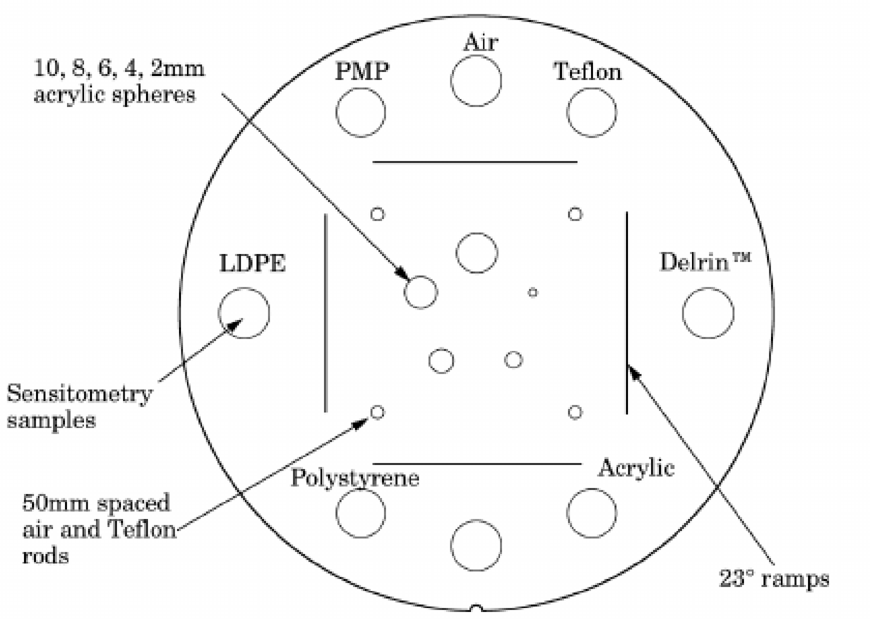

Figure 2.7: Schematic from the Catphan 504 manual of the the CTP 404 sensitometry module which features a variety of different electron density inserts which can be used for contrast and CT number analysis as well as beads and wires for extracting spatial resolution metrics.

The majority of the quantitative metrics we present come from scans of the Catphan 504 (The Phantom Laboratory, Salem, NY). This is a standard quality assessment (QA) phantom for clinical CT devices that provides a series of sections with different objects for calculating image quality metrics. We used the CTP 404 sensitometry module shown in Figure (2.7) and the CTP 528 spatial resolution module shown in Figure (2.8).

There are a number of ways to evaluate the spatial resolution from images of the Catphan phantom in a CT image. The CTP 528 module contains a circular array of bar patterns which we used to subjectively determine the highest frequency set which is resolvable. The same module also has two 0.28mm tungsten carbide beads simulating an impulse source from which a point spread and then modulation transfer function (MTF) can be determined. Furthermore, the MTF can be calculated from the bar patterns themselves [19], as well as any suitably high contrast edge in the image [63].

While the use of MTF in CT has its challenges, notably the assumption of shift-invariance is not satisfied, it still can be useful when treated with some care. Each of the methods above has some advantages and disadvantages. The point source method can provide 3D directional estimates of the point-spread function (PSF), however it can also be sensitive to the location of the bead relative to the image grid with significant difference between a bead located totally within a single voxel or on the interface of many. The bar pattern based evaluation is a clear complement to the visual analysis, however the orientation of the bars relative to the grid will affect some frequencies differently than others which can result in atypical appearing MTF curves. Using an edge spread analysis on the circular phantom boundary provides many samples, at varying directions to the image grid which can be averaged out. It can be impacted by scatter or saturation in the air region near the phantom boundary, however this has not proven to be a significant factor in the images we have analyzed.

The image slice for analysis, the central slice here, is first thresholded based on the image intensity, the connected component with area of the appropriate size is isolated and any holes in the thresholded region are filled. The center of this region is taken as the phantom

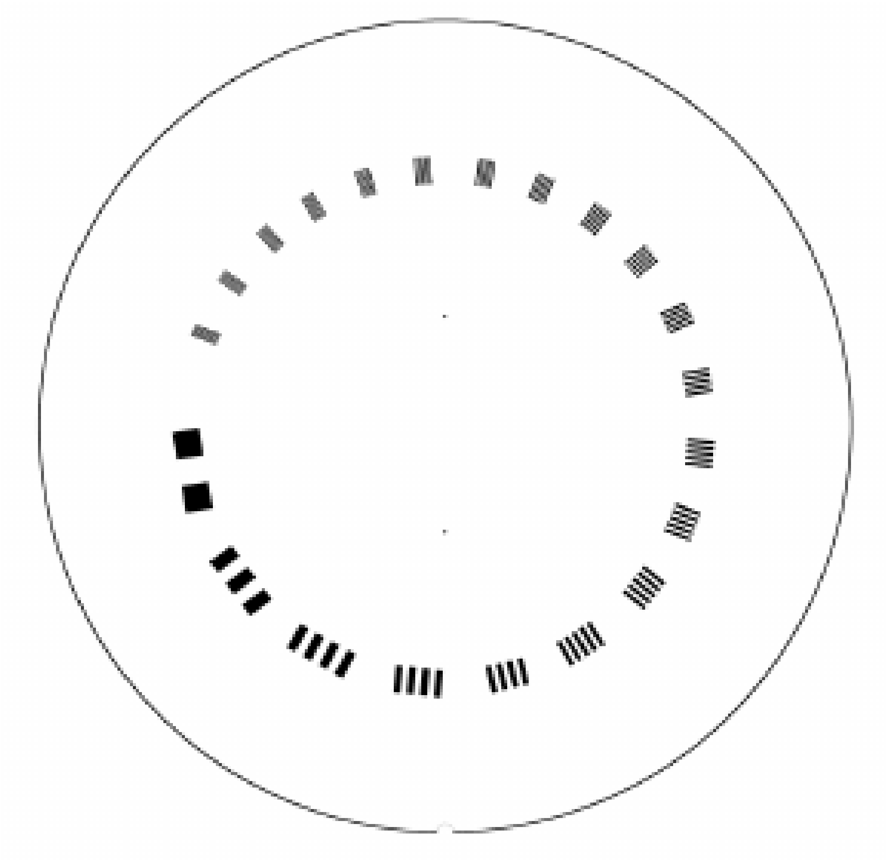

Figure 2.8: Schematic from the Catphan 504 manual of the CTP 528 module that provides a bar-pattern phantom for evaluating spatial resolution metrics.

center and used as the origin of the coordinates for analysis. The data are then resampled at high density, along radial spokes at 8 angles chosen to avoid surface alignment marks, using a linear interpolant from 5 mm inside to 5 mm outside the surface boundary. The edge-spread function is then the mean ($\mu(X)$) subtracted profile over the standard deviation ($\sigma(X)$), or

$$\text{ESF} = \frac{X - \mu(X)}{\sigma(X)}. \tag{2.14}$$

In standard form, the line-spread function (LSF) can be computed from the derivative of the edge-spread function (ESF),

$$\text{LSF} = \frac{d}{dX}\text{ESF}, \tag{2.15}$$

and the MTF as the discrete fourier transform ($\mathcal{D}$) of the LSF,

$$\text{MTF} = \mathcal{D}(\text{LSF}) \tag{2.16}$$

To characterize low-contrast resolution, we calculated the contrast-to-noise ratio (CNR) using the polystyrene insert in the CTP 404 sensitometry module. These inserts have CT numbers which are the closest to the water-like polymer that surrounds them. The metric is defined as

$$\text{CNR} = \frac{2\left|\mu_{\text{roi}} - \mu_{\text{bkg}}\right|}{\sigma_{\text{roi}} + \sigma_{\text{bkg}}} \tag{2.17}$$

where σ represents the standard deviation and μ the mean of the of the pixel values in the respective regions.

The last metric we evaluated was the reproducibility of the CT numbers in the images from the different scanning trajectories we investigated. For this we used the mean and standard deviations in ROIs for all the material inserts of the Catphan CTP 404 sensitometry module in addition to the polystyrene and background ROIs used for the low-contrast CNR calculations. We also evaluated three additional ROIs of the water-like background for a total of four background ROIs.

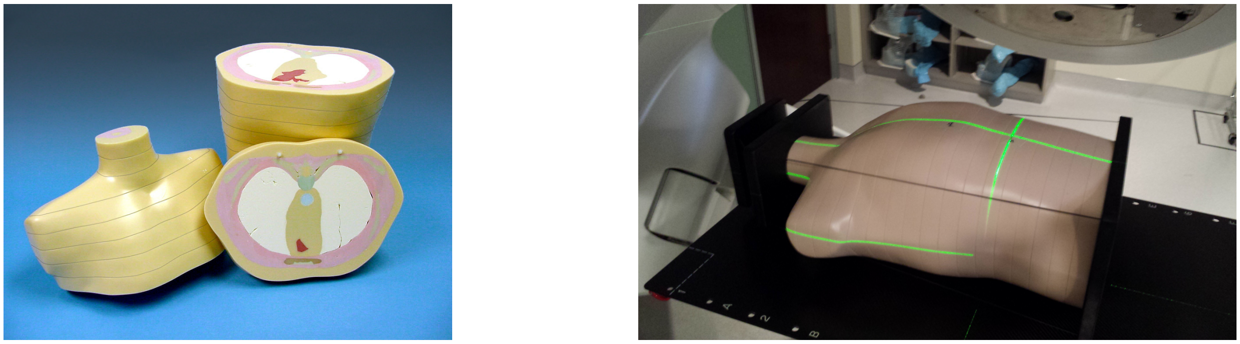

(a) (b)

Figure 2.9: The CIRS torso phantom. On the left is a picture of the phantom broken apart so that the cross-sectional composition of the slices is visible. The anthropomorphic phantom is designed to provide soft-tissue organ structures with realistic electron densities. The image on the right shows the phantom setup on the LINAC treatment couch.

In addition to the CTP 504 Catphan modules, we also used the CIRS model 600 torso phantom shown in Figure (2.9) to evaluate these trajectories with this non-circular scanning trajectory configuration. Though we primarily used this anthropomorphic phantom to produce clinically-relevant reconstructions in the use-case we envisioned for these proposed trajectories, we also extracted CT numbers from ROIs in some of the soft-tissue organs corresponding to aorta, liver and spleen in the phantom's abdomen.

2.6 Conclusion

As our framework was developed in the context of addressing current limitations of using CBCT for IGRT, we wanted to evaluate the image quality obtained from examples of real-data scans of such non-circular trajectories to address two existing clinical issues. To do this, we use our framework to build the necessary reconstruction geometry transforms for the TrueBeam system and selected image quality metrics from standard clinical phantoms for comparing reconstructions from this framework against current clinical image quality. In the next two chapters, we will look at two specific examples of two types of non-circular trajectories that address two existing limitations and compare the subsequent image quality to the current clinical standard.

CHAPTER 3

GEOMETRIC CALIBRATION

3.1 Introduction

Correctly modeling the geometric parameters of the image acquisition is a critical component of tomographic image reconstruction. This is true regardless of whether reconstruction is done with analytic-based or optimization-based methods. Any inconsistency between the real projection geometry and that used for image reconstruction creates artifacts in the reconstructed image [64, 20, 54, 74, 13, 82, 59, 14, 47, 78]. An example of such an artifact is shown in Figure (3.1). This is no less true when using non-standard scanning trajectories. Thus we developed a calibration procedure that can accommodate the different scanning configurations including non-standard scanning trajectories and scenarios in which the object, source and detector are all moving during the scan.

Previous work on geometric calibration for tomographic image reconstruction has approached the calibration problem via analytic [54, 74, 13, 82, 14] and estimation [25, 64, 50, 73, 59] frameworks. Initial calibration efforts utilized optimization-based methods to determine the geometric offsets from projections of a known phantom geometry and nominal system setup. By framing the calibration as an optimization problem, the acquisition parameters were estimated in a way that minimized a cost function associated with improper modeling of the acquisition geometry.

These calibration methods (analytic-based methods included) usually rely on a known calibration phantom, which is typically a set of highly attenuating fiducials arranged in a specific pattern. After scanning the phantom with the system of interest, the detected fiducials are then compared to predicted positions based on the known geometry of the phantom and the nominal projection geometry. In the analytic-based approach, the view parameters are determined by solving for parameters that would transform the projection of the phantom to match the observed projection. In the optimization-based approach,

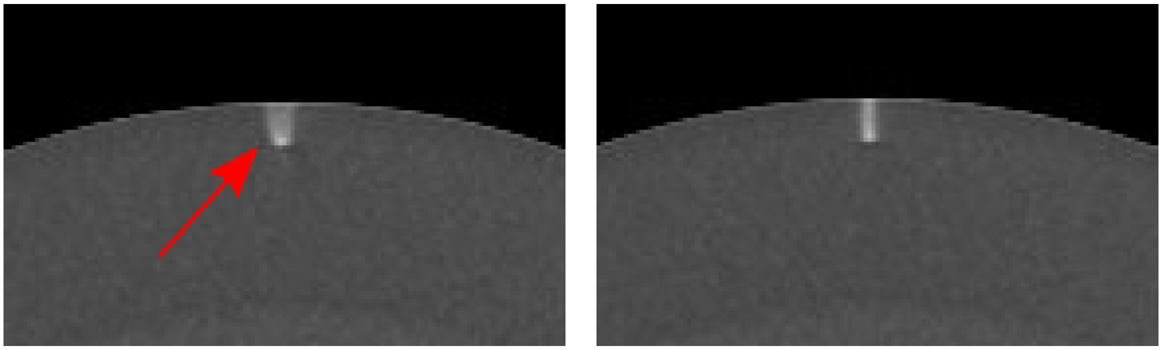

(a) (b)

Figure 3.1: Transverse slice of the Catphan 504 phantom. The image on the left is reconstructed without geometric calibration, and the image on the right is constructed with geometric calibration. The arrow in red indicates one example of the geometric distortion incurred by incorrectly modeling the scanning geometry. This blurring and subsequent loss of spatial resolution is a typical consequence of poor geometric calibration.

geometric parameters are varied to improve the match between the projection of the modeled fiducials and the detected fiducials in the sinogram.

Both methods of performing geometric calibration have their own strengths and weaknesses. The biggest advantage of utilizing analytic-based calibration methods is that the sensitivity to initialization and the sensitivity to the order of parameter variation due to nonlinearity and coupling of parameters faced by estimation are avoided [74]. However, as with optimization-based reconstruction, optimization-based calibration methods are more flexible in providing calibration offsets for the novel trajectories that we studied.

Using previous work for optimization-based geometric calibration [64, 25, 73], we developed a calibration method that utilizes a phantom with known placement of highly attenuating fiducials. By scanning this phantom and comparing the projections to the modeled forward-projection of a mathematical model of the phantom, we can more accurately determine the system matrix ($\mathcal{H}$) in Equation (2.6) for reconstructing from a non-circular scanning trajectory with optimization-based methods resulting in reduced image artifacts.

3.2 Methods

Where analytic-based methods, such as FDK, require a certain acquisition trajectory such as a fixed scanning radius of the source and detector and the angular position of each projection, the optimization-based system matrix makes no assumptions of the geometry in other views. As such, we created a reconstruction framework that incorporates the best geometric estimate of the projection geometry from each view. The flexibility to incorporate geometric corrections in this way is another useful aspect in using optimization-based methods for image reconstruction.

Before attempting to determine any geometric errors in our scanning acquisition, we first modified the calculation of our system matrix to incorporate the geometry information provided by the TrueBeam system as discussed in *Varian coordinates*. In doing this, we took advantage of all the inherent geometry information that is provided with the current clinical system. This information then provided an initial estimate of the scanning geometry which we could then refine with the calibration information we extracted with our calibration protocol.

3.2.1 Phantoms

The first calibration phantom we fabricated for determining geometric offsets is shown in Figure (3.2). The phantom is a 15.2 cm outer diameter acrylic tube with a spiral pattern of CT-spot fiducials placed 2.5 cm along the axial direction every 45°. When scanned, the CT spots are clearly visible in the projection images which is ideal for automating the fiducial detection in the data domain.

However, we realized that using such a spiral calibration phantom creates a degree of ambiguity in the geometry of the projected fiducials. With both this phantom and additional calibration phantoms we created, too much symmetry in the phantom design leads to a rather challenging objective function. Given that only a small portion of the phantom is visible in any one projection view, excessive symmetry produces multiple minima in the objective function where a simple axial shift and rotation offset allows for multiple matches of the modeled fiducials and those in the real data. To avoid such complexity, a calibration phantom with intentional asymmetry is desirable so that the projected fiducials can be indentified and matched without ambiguity.

In addition to the necessary complexity created by this phantom, another concern for a calibration phantom is the uncertainty in the geometry of the phantom itself. Though the guide lines on the cylinder were inscribed with the lathe and its rotational stage, we placed the fiducials by hand. As we were trying to determine millimeter offsets with our calibration, this fiducial placement was suboptimal.

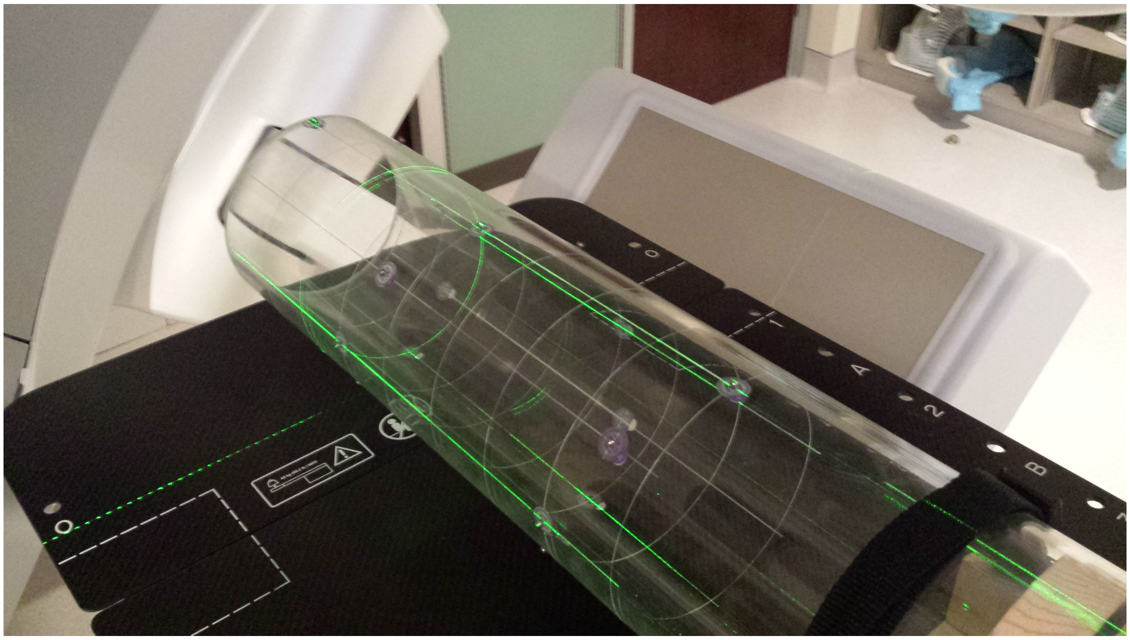

Figure 3.2: Initial geometric calibration phantom with a spiral fiducial pattern.

The phantom we then decided to use for calibration was the Isocal phantom created by Varian shown in Figure (3.3). Additionally, the phantom is manufactured by Varian to help align the MV-treatment isocenter with the kV-imaging isocenter. The Isocal phantom directly addresses the two problems encountered with our first phantom. First, the phantom is designed with intentional asymmetry. The position of the beads on this phantom have a much tighter tolerance than that of our original phantom.

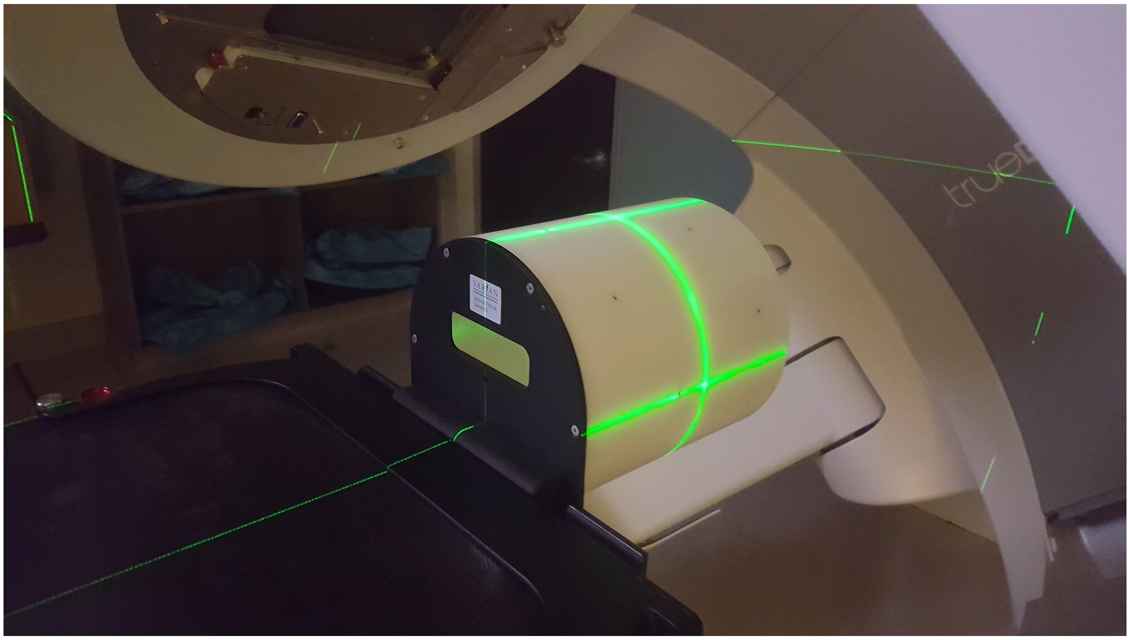

Figure 3.3: Varian's Isocal phantom positioned at the isocenter.

3.2.2 Calibration method

We designed a calibration procedure specifically for the non-standard scanning trajectories we implemented on the TrueBeam system with Developer Mode. Using the methods described in the section *Framework implementation with Varian TrueBeam kV-CBCT system*, we used the view-by-view header information from the TrueBeam system to initialize our calibration procedure. Starting with this initial estimate with which we calculated our reconstruction system matrix $\mathcal{H}$, the additional information extracted from our calibration was used to improve the estimate of both the system matrix and subsequently the estimated image from the reconstruction.

Figure (3.5) provides a schematic illustration of the Isocal phantom for a single view. Ideally, the nominal geometry used to calculate a single projection would produce the simulated projected fiducials in blue. However, as both our work and that of others has found, this is not usually the case [64, 54, 74, 13, 82, 47, 78]. Discrepancies between the reported geometry

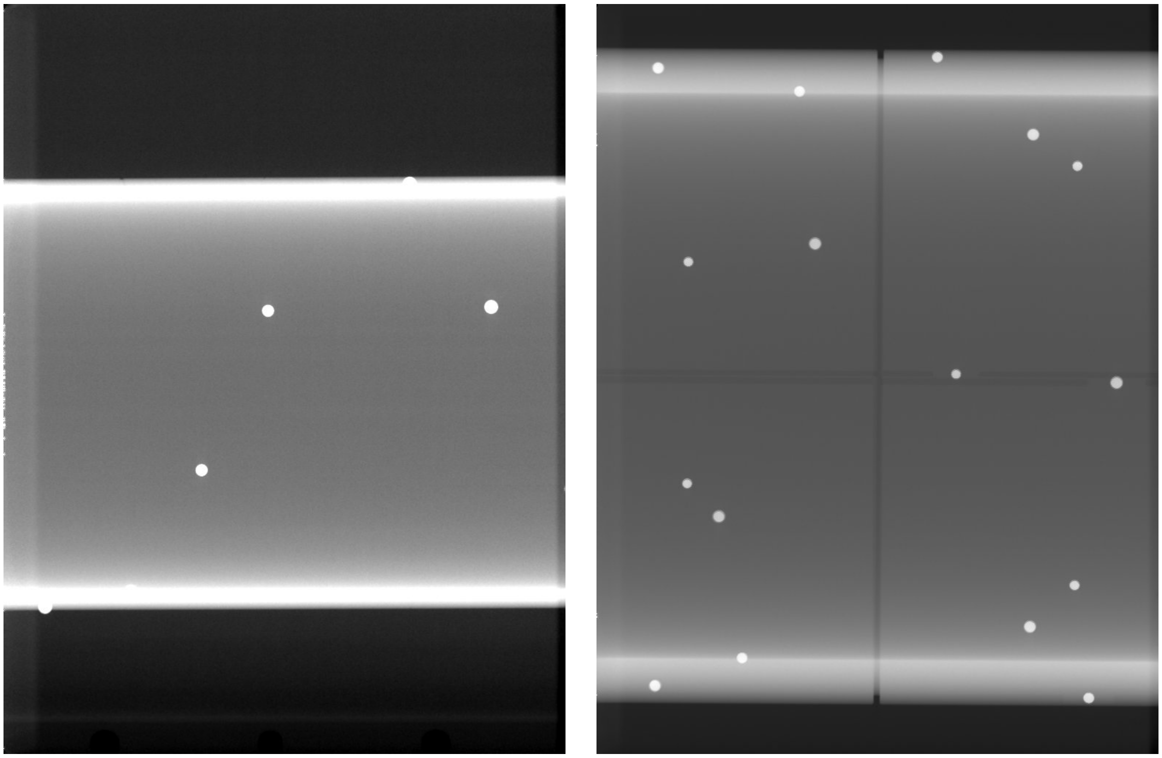

(a)

(b)

Figure 3.4: (a) shows a projection of our first calibration phantom consisting of a single spiral of fiducials around the acrylic tube. (b) shows a projection of Varian's isocal calibration phantom. The additional fiducials seen in each projection, and their unambiguous layout in the projection help prevent local minima when searching for correct geometry offsets

and the actual scanning geometry can arise from multiple sources in a given acquisition.

With a typical CBCT scan, deviations from the nominal geometry can occur in both the phantom's setup (translation and rotation in all three dimensions) as well as that of the source and detector positions (due to translation and rotation deviations in the gantry, source, and detector). The collective impact of these various discrepancies will produce projection views for which the projected fiducials in the data domain do not match the simulated projections from the nominal geometry as shown by the red projected fiducials in Figure (3.5).

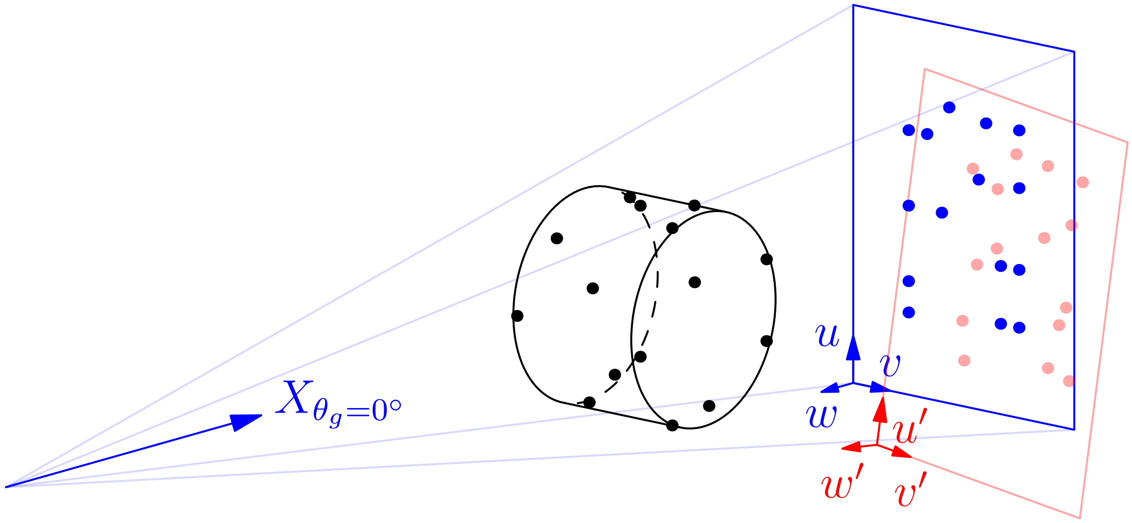

Figure 3.5: Schematic represenation of a single projection view for the isocal phantom with the TrueBeam kV-CBCT scanning geometry. The blue detector and projected isocal fiducials correspond to the self-reported geometry from the imaging system. The red detector and projected fiducials illustrate how translation and rotation offsets of both the phantom and the source-detector system create variations in the projected fiducials in the sinogram space. The bottom left corner corresponds to the origin of the detector coordinate system. The detector's translation and rotation offsets are exaggerated here for illustrative purposes.

Starting with the nominal scanning geometry reported by the projection metadata, we first build an initial projection matrix $\boldsymbol{X}$ that transforms the simulated phantom fiducials in room coordinates to projected spots in detector coordinates. The matrix $\boldsymbol{X}$ is calculated using the variables describing each view shown in Figure (3.6). The source and detector (including the detector's frame vectors $\{\hat{u}, \hat{v}, \hat{w}\}$) are rotated into the global image space by rotating these vectors by the gantry angle (θ_g) at each view. The gantry rotation axis is the logitudinal axis of the cylinder in Figure (3.5) and the y axis in Figure (3.6).

Projection of the fiducial coordinates onto the detector needs to be done in a coordinate system aligned with the detector's frame vectors. The source-to-detector distance needed for projection is the distance along a direction normal to the detector plane, i.e. parallel to the frame vector w. The normal distance from source to detector is calculated by first choosing a ray connecting the source to the detector, $\vec{r}_{\mathrm{sd}}$. The component of this ray that is orthogonal to the detector is then found using the dot product

$$L = \vec{r}_{sd} \cdot \hat{w}, \tag{3.1}$$

where the frame vector $\hat{w}$ corresponds to the detector's normal unit vector. This then provides the vector describing the piercing point ($\vec{p}$) at that view which is given by

$$\vec{p} = \vec{r}_s + L\hat{w}, \tag{3.2}$$

where $\vec{r}_s$ is the vector corresponding to the source position in the image coordinates for that view.

With this new piercing point, it is possible to now construct a transform that projects the fiducials as well as transforms them to the detector basis. The transform to the detector basis is represented by the homogeneous coordinate transform

$$\boldsymbol{G} = \begin{bmatrix} u_i & u_j & u_k & -r_{s,x} \\ v_i & v_j & v_k & -r_{s,y} \\ w_i & w_j & w_k & -r_{s,z} \\ 0 & 0 & 0 & 1 \end{bmatrix}. \tag{3.3}$$

where $\left[-r_{s,x}, -r_{s,y}, -r_{s,z}\right]$ are the room-coordinate components of the source position. Then using the orthogonal ray component found in Equation (3.1), the homogeneous coordinate

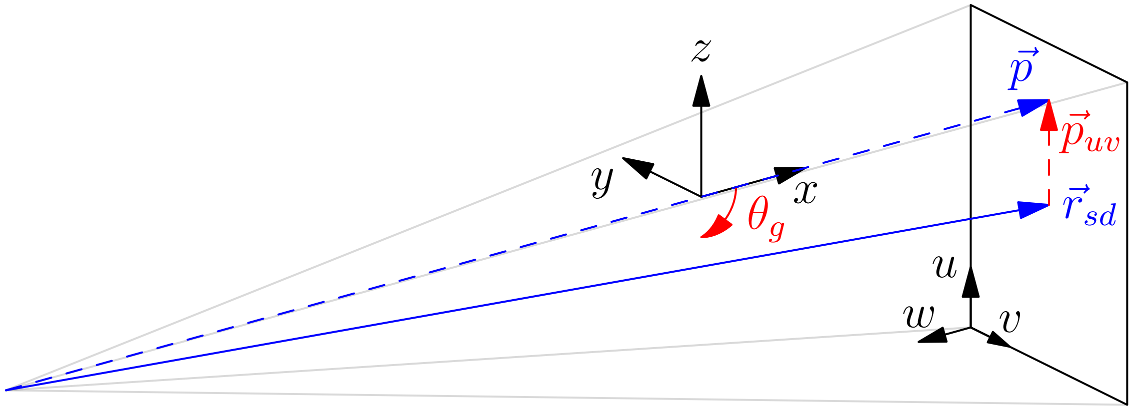

Figure 3.6: Schematic of a single projection view and the associated variables used in building the projective transform matrix ($\boldsymbol{X}$) for that view. The $\{x, y, z\}$ coordinate system corresponds to the standard IEC global coordinate system, and the $\{u, v, w\}$ coordinate system corresponds to the detector frame vectors for that view. The red arrow labeled by θ_g denotes the gantry rotation angle which is defined from the x axis as shown here for the kV imaging system. The blue vector $\vec{r}_{sd}$ points from the source to the detector center, and the blue vector $\vec{p}$ shows the piercing point of the x-ray source on the detector. The red vector $\vec{p}_{uv}$ corresponds to the piercing point in the detector basis as calculated in Equation (3.6).

projection matrix is

$$\boldsymbol{P} = \begin{bmatrix} 1 & 0 & 0 & 0 \\ 0 & 1 & 0 & 0 \\ 0 & 0 & 1 & \frac{1}{L} \\ 0 & 0 & 0 & 0 \end{bmatrix}. \tag{3.4}$$

Using these transforms so that they are pre-multiplied by the fiducial position vectors, the combined transform is then

$$\boldsymbol{M} = \boldsymbol{G}\boldsymbol{P}. \tag{3.5}$$

which transforms a room coordinate point into the detector basis, and then projects it onto the detector plane.

Finally, this information can be combined to create a single transform of the fiducials in the global image coordinate system to the projected spots on the detector in discretized detector bin coordinates. First, the coordinates of the piercing point must be calculated in the detector basis as

$$\vec{p}_{uv} = (\vec{p} - \vec{r}_d)\,\boldsymbol{G}, \tag{3.6}$$

where $\vec{r}_d$ is the center of the detector in room coordinates. With all this, the projection transform used to calculate the projected fiducials in discretized detector bin coordinates is

$$\boldsymbol{X} = \boldsymbol{M}\boldsymbol{T}(\vec{p}_{uv})\boldsymbol{S}\left(\left[\frac{1}{s_{\text{pix}}}, \frac{1}{s_{\text{pix}}}, 1\right]\right)\boldsymbol{T}\left(\left[\frac{u_{\text{len}}}{2} + 0.5, \frac{v_{\text{len}}}{2} + 0.5, 0\right]\right), \tag{3.7}$$

where $\boldsymbol{S}$ is a scaling transformation along the $\{u, v\}$ basis by the inverse of the pixel size (s_{pix}), and $\boldsymbol{T}$ is a translation transformation to place the origin of the discretized detector basis at the center of the corner pixel.

With the projection transform $\boldsymbol{X}$, each vector corresponding to the fiducials on the Isocal phantom can be projected onto the discretized detector basis as illustrated in Figure (3.5). These projected spots are then matched to the detector spots in the real sinogram. The L_2 norm between the real and simulated projected spots is then calculated and serves as the cost function for the optimization-based calibration.

As with other optimization-based calibration procedures, we iteratively vary the parameters corresponding to the geometric degrees of freedom (DOF) of the scanning trajectory. The phantom pose (position and orientation) is first allowed to vary in the room coordinate system to account for potential setup errors between the room coordinates and the modeled position of the phantom. Once the pose of the Isocal phantom is identified, then the source, detector, and patient couch translations and rotations are allowed to vary, and the cost of the simulated fiducial projections are calculated at each step. We use the Nelder-Mead simplex algorithm [46] to minimize the L_2-norm cost function.

Given that there are there are different combinations of couch, source and detector motions that can cause the same change of the object relative to the source and detector within the image coordinate system, there are some degrees of freedom that can couple with others. For instance, shifting the patient in the positive longitudinal direction is effectively the same as allowing the source and detector to move the same distance in the negative longitudinal direction. This requires that only a few parameters are allowed to vary at once as allowing too many parameters on this non-convex surface will often produce nonphysical geometric corrections. Once the cost has been minimized, the geometric offsets are used as the calibration information for calculating the system matrix $\mathcal{H}$ for the image reconstruction.

For a new trajectory, this phantom is first scanned to identify any potential corrections to the parameters reported in the TrueBeam data headers. Though we find the self-reported position from the acquisition metadata to be very accurate, there are still some scanning configurations for which the additional refinement from our geometric calibration is critical for obtaining the best quality reconstruction. This is particularly true for scanning trajectories where the object and the kV imaging system move simultaneously.

3.2.3 Experimental validation

To evaluate the efficacy of our calibration procedure, we investigated its performance on calibrating both a standard, half-fan, circular trajectory where the couch is stationary as well as a virtual isocenter trajectory. For purposes of discussion, a virtual isocenter is where the couch moves simultaneously with the gantry rotation from a fixed point that we call the virtual isocenter. We will return to the example of the virtual isocenter trajectory in *Collision-avoiding trajectories*. For each of these trajectories, we used the same Developer Mode script to scan both the Catphan phantom and the Isocal phantom. We subsequently used the sinogram from the Isocal scan to extract calibration offsets for that particular trajectory using the calibration method described above.

We reconstructed the Catphan scans from these two trajectories with and without the calibrations offsets. An isotropic image grid of 0.473 mm was used for each reconstruction with application of the half-fan weighting [4]. For all reconstructions, 200 iterations of MLEM were used, as described in the *Generalized trajectory framework* section.

3.3 Results

After acquiring the circle and virtual isocenter trajectories of both the Catphan phantom and the Isocal phantom, we used our calibration procedure to find the geometric offsets for each view. Table (3.1) shows a subset of the offsets given by our method for a gantry angles at approximately 90° intervals. For these calibrations, we only allowed the optimization program to vary the detector's lateral and longitudinal position as well as the source's longitudinal position. With the virtual isocenter trajectory that also introduces the couch motion, there is a larger amount of variation in the offset magnitude than in the circle trajectory that has a stationary treatment couch.

Table 3.1: Table of selected calibration offsets at approximately 90° increments of the gantry angle for the circle and virtual isocenter trajectories shown in these results. For these results, only the detector's lateral and longitudinal position as well as the source's longitudinal position in the radiation coordinate system were allowed to vary in this calibration example.

Trajectory	Gantry angle [°]	Det lat [mm]	Det long [mm]	Src long [mm]
Circle	-179.9	-0.4	-0.9	1.8
	-90.2	0.4	-0.8	1.5
	-0.2	0.5	-0.8	2.0
	90.2	-0.2	-1.0	2.2
	180.2	-0.4	-1.0	1.8
Virtual isocenter	-180.1	-0.3	-0.6	2.5
	-90.0	1.6	0.1	0.7
	0.0	0.7	-0.7	1.5
	90.0	0.1	-1.5	3.0
	178.2	-0.2	-0.8	2.5

Figure (3.7a) shows the CTP 528 spatial resolution module slice from the reconstructions of both the circular scan (left column) and the virtual isocenter scan (right column). The top row shows the slice from the uncalibrated reconstruction using the nominal projection geometry from image metadata. The circle and virtual isocenter scans without calibration demonstrate that moving the treatment couch during the scan introduces additional geometric error over the standard circle scan which visually degrades spatial resolution.

The bottom row of Figure (3.7a) shows the same slice from the corresponding trajectory with the geometric offsets from the calibration procedure incorporated into the system matrix $\mathcal{H}$. For the circular scan, using the calibration information does provide a bit of an improvement in spatial resolution. However, the efficacy of the calibration method is particularly striking for the virtual isocenter scan. By using the calibration offsets in the reconstruction model, the spatial resolution of the virtual isocenter reconstruction becomes comparable to that of the circular scan.

Figure (3.7b) shows the $L_2 -$ norm of the distance between the simulated fiducial projections and the real fiducial projections acquired from the circle and virtual isocenter scans of the isocal phantom. We can see that the calibration did effectively reduce this cost from the nominal geometry (blue) to the calibrated geometry (green). This cost also reflects the same trend we see in the spatial resolution of the images shown in Figure (3.7a).

Comparing the the $L_2 -$ norm of the uncalibrated scans in Figure (3.7b), we see that there is far more disagreement between modeled and observed Isocal fiducial positions for the virtual isocenter scan than that of the circular scan, leading to more artifacts and loss of spatial resolution in the virtual isocenter reconstruction than in that of the circular scan. With the geometric calibrations applied, the cost for the virtual isocenter and circular trajectories is quite comparable, as is the spatial resolution.

3.4 Discussion

From these results, especially with the virtual isocenter, we can see that there is an improvement in the spatial resolution by incorporating the calibration offsets obtained from the Isocal phantom and our calibration procedure. A general loss of spatial resolution is

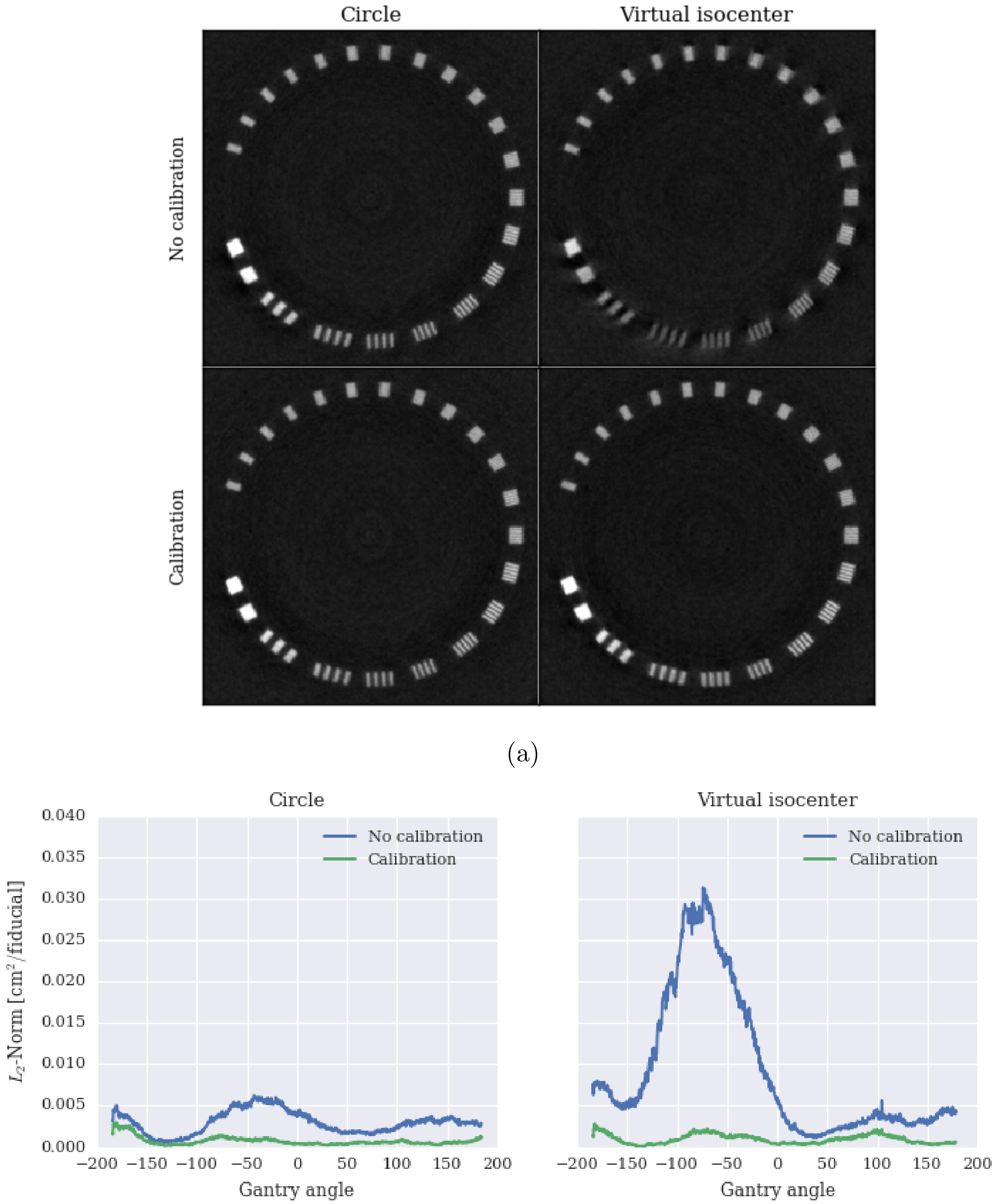

(a)

(b)

Figure 3.7: (a) shows the 200$^{\text{th}}$ iteration of MLEM reconstructions of the CTP 528 spatial resolution module from the Catphan phantom for two different trajectories. The left column is from a 1.5X circular scan, and the right column is from a 1.5X virtual isocenter scan reconstructed onto a 0.473 mm isotropic image grid([-100, 2000] HU). The top row shows the reconstruction using the nominal geometry from self-reported metadata, and the bottom row corresponds to the calibrated reconstructions. (b) shows the L_2-norm used for the calibration cost function before (blue) and after (green) calibration for both the circle (left) and the virtual isocenter (right).

the typical consequence of attempting to reconstruct an object without using the correct geometry to construct the system matrix. As shown in Figure (3.7a), this loss of spatial resolution can be drastic as in the case of the virtual isocenter trajectory.

It is important to understand that by introducing the motion of the couch in the virtual isocenter trajectory, there is the subsequent introduction of additional uncertainty associated with the geometry of the couch position. Both the visual appearance of the spatial resolution module in Figure (3.7a) as well as the cost function in Figure (3.7) prior to calibration reflect the additional uncertainty introduced by the couch motion. However, the ability to recover the bar phantom pattern and achieve a similar cost function after calibration as the circle trajectory demonstrate that this additional uncertainty can be accounted for with calibration.

It is also interesting to note the sinusoidal appearance of the cost function as plotted against gantry angle in Figure (3.7). The variation as a function of the gantry's orientation is most likely due to the variation in the torque applied to the gantry by gravity. Though this gravitational impact has been studied before [67], it is interesting to see the additional uncertainty this effect has when also combining the simultaneous couch motion into the trajectory.

One of the most challenging aspects of using an optimization-based calibration procedure such as ours is that different offset variables can couple with other parameters that geometrically impart the same effective offset relative to the image space coordinate system. An example of that would be a couch offset in one direction being equivalent to a detector offset in the opposite direction. While this ambiguity is exactly the same feature we utilize when implementing some of trajectories, i.e., an axial-FOV extension by either translating the couch or the imaging arms, it does complicate the calibration procedure.

In this work, we addressed by only allowing some parameters to vary while keeping other variables we know do have uncertainty fixed. For example in Table (3.1), we only use offsets for the source and detector for both the circle and virtual isocenter trajectories. In this case, though we know the couch introduces additional uncertainty, the calibration procedure is able to incorporate these offsets into the relative offsets of the source and detector. As we are ultimately interested in obtaining a proper reconstruction of the object in the image space, reduction in cost in the objective function subsequently manifests as an improvement in the projection geometry relative to the image space.

In future calibration work, it would useful to address this ambiguity by constraining the optimization function in a way that would ensure much greater absolute accuracy of the calibration offsets. Though we did not do that here, this could be done to some degree by taking known tolerance of the LINAC components into account. For example, the tolerances of the couch position and the imaging arms could be used to provide the appropriate weighting for how much the different offset magnitudes are allowed to vary.

3.5 Conclusion

In developing our optimization-based geometry calibration procedure, we found that proper geometric calibration is critical to achieving optimal tomographic image quality. This is particularly true for more complicated trajectories where additional motion components such as that of the treatment couch introduce additional degrees of freedom in which geometric errors can arise. As shown in Figure (3.7), the additional motion of the couch with the simultaneous motion of the source and detector introduces a larger deviation from the nominal scanning geometry.

The optimization-based calibration we used in this study provides a robust framework for calibrating arbitrary scanning trajectories. The ability to acquire view-by-view calibration information with this approach dovetails nicely with the optimization-based framework that enables the reconstruction from the different trajectories we studied in this research. Though many of the different analytic-based methods described in the literature could be adapted to some of these trajectories [54, 74], the benefit of the optimization-based framework for both reconstruction and geometric calibration comes from freedom to easily model and reconstruct from any desired trajectories as well as geometric offsets that deviate from the analytically prescribed model.

Though this does imply that calibration scans must be acquired for each scan of interest, there are optimization-based calibration methods similar to ours that attempt to extract calibration information with no *a priori* knowledge of the phantom [59]. Such calibration methods or built-in calibration markers in the table are potential ways in which it would be possible to avoid acquiring calibration information for every scan of interest. As we used the TrueBeam kV-CBCT system for our data acquisition, Varian's Isocal phantom provided a convenient means of calibrating the imaging system as the LINAC use case already demands accurate calibration for treatment accuracy in addition to image quality alone.

In the following chapters, where we investigate particular applications of these different trajectories, we will use our calibration method with the Isocal phantom to more accurately model the system matrix $\mathcal{H}$. Though the more exotic scanning trajectories introduce more degrees of freedom that create greater geometric uncertainty, our calibration procedure determines what these deviations are from the self-reported geometry metadata. For these trajectories, we found that incorporating geometric calibration consistently improves image quality.

CHAPTER 4

AXIAL FIELD-OF-VIEW EXTENSION

4.1 Introduction

A major limitation of LINAC-mounted CBCT kV-imaging systems is their axial coverage. This is primarily due to the detector size which is restricted by both cost and engineering concerns. Unlike modern diagnostic CT systems, the LINAC gantry is unable to perform more than a single rotation in a given direction. Without the ability to continuously rotate about the patient in the same direction, the helical scan solution to this limited-axial-FOV problem used by modern diagnostic CT systems is untenable.

When an extended axial FOV is needed in the IGRT clinic, the current practice is to acquire two circular scans centered at different axial positions. Once each independent volume has been reconstructed with an analytic-based FBP algorithm such as FDK, the two volumes are stacked to create the extended image. Though this stacked image does extend the axial coverage beyond that provided by a single circular scan, there are some limitations to this approach. We investigated if the non-circular trajectories with optimization-based methods described in *Generalized trajectory framework* can provide a solution to these shortcomings.

The main problem with the current clinical approach is a limitation incurred by reconstructing each of the volumes with analytic-based reconstruction methods, such as FDK. When combining the volumes of two independently-constructed FDK volumes acquired at different axial positions, the overlap region between the two axial positions corresponds to the larger cone angles of the two independent volumes. As methods like FDK are known to suffer from cone-angle artifacts at the axial extremes of the reconstruction volume as shown in Figure (2.2), this volume stacking approach abuts the regions of the two independent volumes most afflicted with cone angle artifacts against each other as shown in Figure (2.3).

Furthermore, the stacking of FDK volumes is also limited by the axial coverage allowed by the reconstruction algorithm. In Figure (2.3), everything bounded by the detectors for both circles at opposing views constitutes the image support of optimization-based methods like MLEM. For comparison, the support of the FDK reconstruction is limited to just the shaded regions of each circle.

As the axial spacing between the two circles is increased, the shadow zones [23] corresponding to regions outside the support of the FDK reconstruction further contaminate the region of overlap. As the spacing between the circles is increased, these shadows regions encroach into the volume of the stacked FDK image. At the maximum axial spacing of 20 cm for the TrueBeam system, the shadow zones extend directly to the center of the image as shown in Figure (2.3b) resulting in missing information in the stacked volume.

In addition to the shadow zone contamination, there is another limitation that affects the stacked FDK volume approach. As the two circular volumes are reconstructed independently, neither scan benefits from mutually-shared information in the overlap region between the two scans, which could potentially reduce the cone-angle artifacts. For axial separations between the two circles (d) that is less than the maximum spacing, there is redundant sampling of the image volume by the two circular scans. This is illustrated in Figure (2.3a) where the purple region corresponds to this redundant sampling. For any axial separation less than the maximum, optimization-based reconstruction methods can take this redundant sampling into account whereas the FDK volumes are agnostic to this additional information in the neighboring reconstruction volume.

Taking advantage of the flexible reconstruction framework described in *General CBCT trajectory reconstruction framework with optimization-based algorithms*, data from more than a single circular scan can be reconstructed. Provided that the correct geometry of the acquisition trajectory is well understood and properly calibrated (e.g. using a calibration method such as that discussed in *Geometric calibration*), the system matrix of the image formation process can be calculated for arbitrary CBCT scanning configurations. Trajectories are not limited to the few cases of non-circular trajectories for which analytic inverse formulations exist such as the line [72], circle and line [83, 38], circle and arcs [84, 39], and non-planar orbits [42].

Using some of the trajectories enabled by optimization-based methods, we can address the problem of the limited axial coverage for LINAC-mounted CBCT kV-imaging systems. Rather than increasing the size of the detector, the source and detector motion can be extended in the axial direction, allowing projections to be obtained for axial positions beyond what is illuminated with current detector sizes and a circular scanning trajectory.

In this chapter, we study a few different trajectories that could address the limited axial coverage provided by LINAC-mounted kV-imaging systems. For the case of the TrueBeam system, the axial coverage of the treatment FOV is 40 cm while the CBCT coverage from a single circle is only 20 cm. This limitation can be problematic for patients with treatment volumes that extend axially beyond what is visible in a single circular acquisition [77]. The trajectories we investigate in this chapter provide extended axial coverage. Our hypothesis is that data from scans with extended axial coverage can be reconstructed into extended FOV images with quality equivalent to current clinical scans using only a single circle and resultant limited axial FOV.

4.2 Methods

4.2.1 Trajectories

In order to obtain additional axial tomographic information from a patient beyond what is covered by the detector, there must be a relative shift along that axis between the patient and the imaging system. As described to in the *Generalized trajectory framework* section, either the patient or the imaging system can shift along this direction to obtain the desired projection information as long as the motion is correctly reflected in the system matrix $\mathcal{H}$. With the additional projections along the axial direction, it is possible to extend the axial coverage of the tomographic image beyond that which is provided by a single circular scan.

The current clinical method of obtaining an extended axial image involves stacking the

FDK reconstructions of two circular scans at different axial positions. For this reason, the first class of trajectories we studied was a dual-circle trajectory shown on the left in Figure (4.1). As the LINAC is only able to make one complete rotation of the gantry, this is implemented by acquiring a circular trajectory scan, applying the axial shift, and then acquiring a second circle by rotating the gantry in the opposite direction.

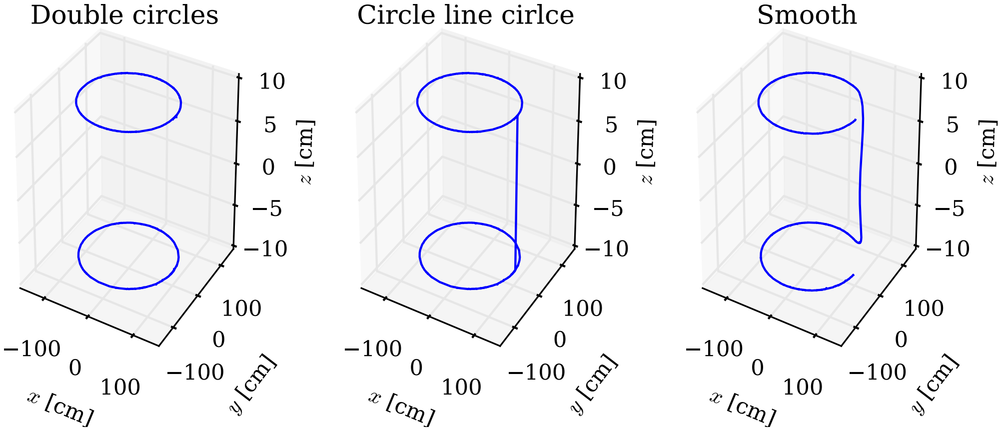

Figure 4.1: Source trajectories of the three classes of extended axial-FOV trajectories studied with a separation of 17 cm between the planes of the circular components of the scan. Moving in diametric opposition of the source is the CBCT detector which provides coverage 15 cm above and below the source trajectory in the axial direction (z) All of these trajectories are plotted in the image coordinate space described in the section *Varian coordinates*. On the left is the double circle trajectory that is equivalent to the double circle scan currently used in the clinic to obtain extended axial coverage. In the middle is the circle-line-circle trajectory that acquires additional projection information as the source and detector translate from the axial position of the first circle to that of the second. On the right is the smooth trajectory in which the translation component occurs during the rotation of the two circles.

Another class of trajectories we studied was the circle-line-circle (CLC) trajectory shown in the middle of Figure (4.1). Like the double circle trajectory, this trajectory consists of two circles at various axial positions, but with projections also acquired during the linear shift between the two axial positions of the circles for the CLC trajectory.

The last class of trajectories we studied will be referred to as the smooth trajectory which is shown at the right of Figure (4.1). It is similar to the CLC trajectory in that it consists of two circles at two different axial positions with projections acquired along the axial shift component. The gantry motion is the same in that it performs two rotations in the opposite direction. The difference here is that the axial shift component is begun before the first gantry rotation is complete, and the second gantry rotation begins before the axial shift is complete. Unlike the double circle and CLC trajectories, this trajectory does not have a complete circle at either of the two axial positions.

4.2.2 Simulation

As the current clinical procedure for obtaining an extended axial FOV CBCT is by stacking together the independently reconstructed images of two circular scans acquired at different axial locations, we first used simulations to determine the maximum axial spacing between the two circular trajectories allowed by this technique. To evaluate this, we compared the simulated results of stacking independently-reconstructed FDK images from two circular scans at various axial separations to the MLEM reconstruction of those same two circles reconstructed simultaneously as a single acquisition sinogram [16].

We simulated a Defrise-style phantom modeled with the 3D X-ray projection software TAKE [65]. The phantom was composed of a 15.2 cm outer diameter acrylic cylinder with alternating density disks of Delrin and cork 0.5 cm thick. Due to the alternating density disks along the axial direction, this particular phantom has been acknowledged by the authors of FDK to be particularly susceptible to cone-angle artifacts [21]. We used the TAKE software to forward project the phantom as well as generate a digitized "truth" phantom for calculating comparison metrics. The simulation program generates a forward projection from a specified trajectory given a mathematical definition of the phantom as well as its material properties and the spectrum generated by the x-ray source.

We created projection data for dual-circle trajectories that had variable axial separation between the two circles. With a 1.5x magnification factor and a 30 cm detector size along the axial direction (e.g., geometry equivalent to that of the TrueBeam kV-imaging detector), a single circular scan has a maximum axial coverage of 20 cm. Thus, the maximum spacing between the two circles is 20 cm as any separation larger than this creates a gap between the two imaging volumes. We therefore created trajectories with 10, 12, 14, 16, 18, and 20 cm separations between the planes of the source's dual-circle trajectory.

In addition to the double circle trajectory, we also simulated projections from the CLC and smooth classes of trajectories shown in Figure (4.1). We uniformly distributed 600 views over the entire trajectory. Of these 600 views, 20% were distributed along the axial translation stage.

For the extended-volume reconstruction using the stacked FDK, we independently reconstructed each circular scan with FDK using a standard Hann filter. The reconstruction image space consisted of a 256 × 256 transverse grid of 1 mm isotropic voxels. To combine the two reconstructed volumes for an extended axial-coverage image at a given spacing, the axial location between the two circle positions was used as a discriminator to select where to truncate each of the two volumes before stacking them together. In the reconstructed image, the volume superior to this axial position was taken from the superior circle, and the volume inferior to this position was taken from the inferior FDK reconstruction volume.

For the MLEM reconstructions, the projection data were treated as a single sinogram to reconstruct the extended volume. After defining the extended image volume, we computed the system matrix for each of the different spacings and trajectories based on the trajectory of the source and detector. We used 100 iterations of the MLEM algorithm to find an estimate for the image.

4.2.3 Experimental Data

After identifying potential benefits of addressing the limited axial FOV using non-circular trajectories as described in the *Generalized trajectory framework* section, we then evaluated how well this approach worked when implemented on our TrueBeam system using Developer mode as describe in the *Framework implementation with Varian TrueBeam kV-CBCT system* section. By using the Developer Mode XML control schema, we created acquisition scripts that implemented gantry rotations with a component of axial translation between the patient and the kV-imaging system. The trajectory plots shown in Figure (4.1) are from the actual trajectories of the three classes studied with a 17 cm gap between the two planes of the circular orbits.

Though the imaging framework is agnostic to which component of the system effects the relative motion between the patient and the imaging system, there are some engineering limitations of the TrueBeam system that determine how the axial translation component of these trajectories is implemented. In the current TrueBeam implementation, the kV-imaging robotic arms cannot perform any translational movement while the gantry is rotating. As such, all of our axial translation were implemented by moving the treatment couch for all of the trajectories instead of translating the robotic arms. As the CLC trajectory requires no gantry rotation during the translation stage, we did acquire one CLC trajectory using translation of the robotic imaging arms for comparison.

The image quality that results from using these trajectories with optimization-based algorithms must be quantitatively evaluated for the different trajectories and spacings chosen. Given that contrast resolution is important to clinical utility [17], we wanted to characterize the low-contrast resolution as a function of axial position for the different trajectories and spacings. As the extended axial coverage we obtain with the kV imaging system using these methods is novel, there is not a standard phantom for characterizing low-contrast resolution as a function of axial position within a single scan. Figure (4.2) shows the limited coverage afforded by a single Catphan 504 phantom.

For this reason, we built a custom low-contrast disk phantoms that fit into an acrylic tube with extended axial coverage as shown in Figure (4.4a). The disks themselves, such as the one shown in Figure (4.4b), are designed to provide similar metrics such as those obtained with the Catphan phantom's low-contrast module CTP515 shown in Figure (4.3). Additionally, the largest holes are designed to hold the different electron density plugs from the Gammex (Middleton, WI) RMI tissue characterization phantom. By placing four of

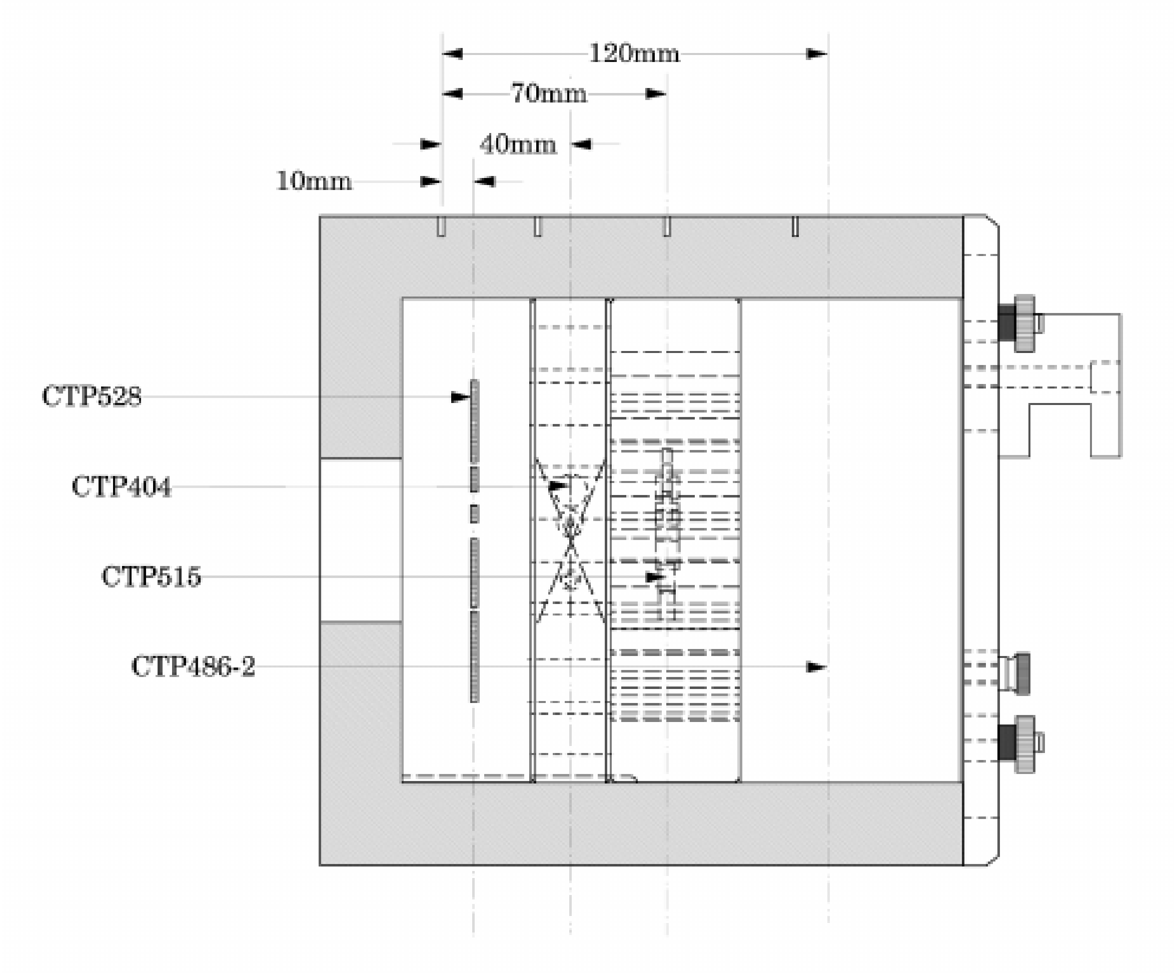

Figure 4.2: Catphan sagittal view showing the axial extent of a single Catphan 504 phantom from the Catphan 504 manual.

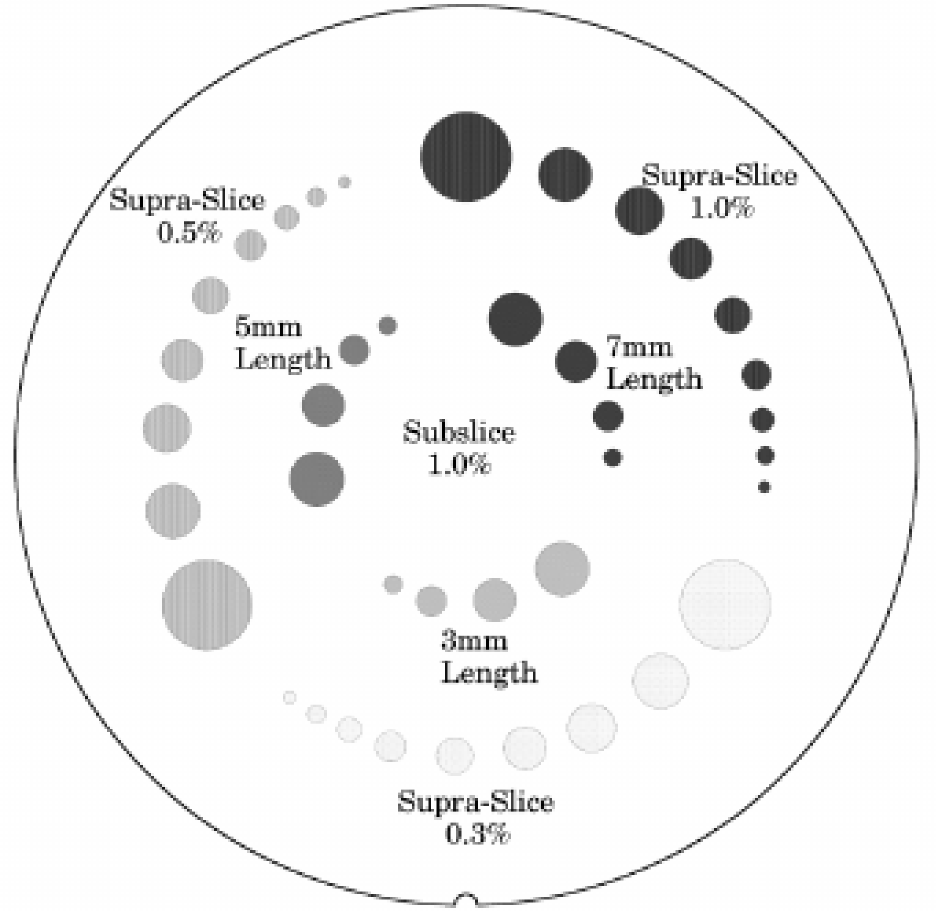

Figure 4.3: Catphan CTP 515 low-contrast module schematic from the Catphan 504 manual.

(a) (b)

Figure 4.4: The left image shows the experimental setup of the acrylic tube with four low-contrast disks. Given the symmetry of the scanning geometry, one disk is placed at the plane between the two circles. The remaining three are placed at different axial positions in one half of the image volume. The right image shows the four low-contrast disks with the larger holes holding solid water RMI inserts.

these disks in the tube, we can obtain these metrics as a function of axial position within a given reconstruction.

After some preliminary studies, we found the nominal 1% low-contrast inserts were too challenging to consistently identify on the LINAC's kV-imaging system. Thus, we decided to use two Catphan 504 phantoms to provide features for obtaining image quality metrics. As we needed to acquire image quality metrics over the extended axial coverage, we placed the two Catphan phantoms end to end. This effectively provided a standard image-quality phantom that also spanned the extended axial-FOV volume enabled by these trajectories of interest.

For the all of the different trajectory scans, the double-Catphan configuration was positioned with one of the Catphan's sensitometry module shown in Figure (2.7) aligned at imaging isocenter. As this module provides many of the features we used to calculate image metrics, we wanted to acquire metrics with this module placed so that it is in the plane of the source's orbit for one of the two circles. By doing this, we could compare the image quality metrics from the different scanning trajectories against a clinical circular FDK scan where the image quality is evaluated on the plane where FDK satisfies Tuy's condition. We acquired all three classes of trajectories (double circle, CLC, and smooth) with both full-fan and half-fan detector configurations.

For a LINAC system, it often is the case that the patient's transverse slice volume exceeds the transverse FOV support allowed by the trans-axial coverage of the kV-imaging detector when it is centered with the piercing point of the source to detector ray in the middle of the detector. To overcome this limitation, a detector offset is given to the detector so that it is shifted in the lateral dimension in the radiation coordinate system shown in Figure (2.4) [10, 12]. In doing this, the transaxial FOV is increased as this half-fan configuration acquires projections from half of the phantom or patient in the first 180° of rotation and the second half of the phantom or patient projections in the second 180° of rotation..

We also scanned the CIRS torso phantom shown in Figure (2.9b). We aligned the phantom so that the center of phantom was placed at the midpoint between the axial position of the two circular components of the different trajectories. We again acquired the three classes of scanning trajectories, but only with a half-fan detector configuration as this larger phantom would incur truncation artifacts with a full-fan configuration.

In addition to acquiring the different trajectory scans of these phantoms, we also repeated the scans with the Isocal phantom to acquire geometric calibration information. As the Isocal phantom is designed to align the MV-treatment isocenter with the kV-imaging system's isocenter, it has a fixed mounting point on the treatment couch. In order to extract the calibration information for the different trajectories, we positioned the Isocal phantom on the treatment table at the location where we placed the double Catphans and the CIRS torso phantom. As described in *Geometric calibration*, we used the Isocal scans to provide calibration corrections for all three trajectories with both the full-fan and half-fan detector configurations.

The clinical reconstruction software uses a larger voxel size for half-fan detector scans than for full-fan detector configurations. We therefore reconstructed the CIRS torso phantom onto a 0.836 mm isotropic voxel grid. However, as voxel size is a critical parameter of the reconstruction program, we reconstructed all of the scans of the double-Catphan configuration onto a 0.473 mm isotropic image grid for all detector configurations so that only the detector configuration would be the independent variable. As we will discuss in the next chapter, we selected 200 iterations of MLEM for all of our optimization-based reconstructions.

In addition to reconstructing the extended-axial-FOV sinograms using the optimization-based framework, we also reconstructed the superior and inferior circles of the double circle using Varian's clinical FDK algorithm in iTools. In addition to the default reconstruction chain, we also reconstructed the two circles without Varian's pre-processing chain that provides a scatter-correction to the projection data. We did this because no scatter correction modeling was implemented in our MLEM reconstructions. Though we had initially attempted to extract the pre-processed projection data from iTools to use in our reconstruction chain, we discovered that some of the non-standard motions we implemented with the LINAC could not be accommodated in iTools as it did not conform to the typical circular trajectory anticipated by Varian's software.

For additional comparison, we also reconstructed the superior and inferior circle independently with our analytic-based reconstruction chain. We then stacked these two independent volumes together the same way as for the FDK reconstructions. Finally, as MLEM generally provides better spatial resolution that FDK, we also reconstructed the two circles without pre-processing using the iTools FDK with a sharp kernel as to increase the spatial resolution from the FDK reconstructions.

4.3 Results

4.3.1 Simulation

Our simulations suggested that the optimization-based reconstruction of the dual-circle trajectory is comparable to the clinical stacked FDK method when the axial spacing is small enough that the stacked FDK method is still able to yield a complete reconstruction. As shown in Figure (2.3), larger axial spacings (d) between the two circles results in larger portions of the image volume falling outside of FDK's support volume. For the geometry of our Defrise-style phantom and our TrueBeam kV-imaging system geometry, the stacked-FDK method and the optimization-based reconstruction were comparable up to a gap of approximately 14 cm. For larger axial gaps, the FDK shadow zone between the two volumes begins to infiltrate the reconstruction volume creating voids in the reconstruction volume.

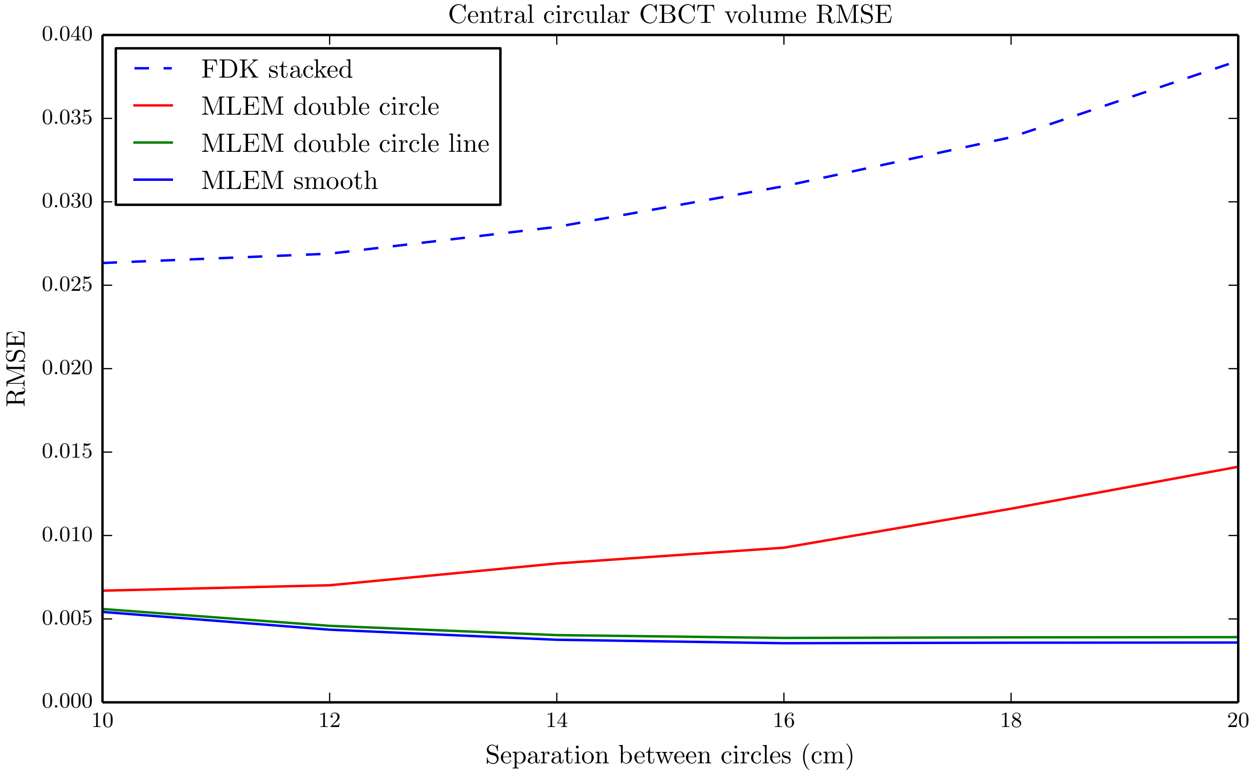

Figure 4.5: Plot of the RMSE for extended volumes of different simulated trajectories with different spacing between planes of the circles, compared to the central CBCT volume of a single circular scan which is an axial FOV of 20 cm.

Figure (4.5) shows a root-mean-square error (RMSE) comparison of the three classes of trajectories as well as the stacked FDK method with different axial spacings between the two planes of the circles. The volume for which the RMSE is calculated is the central volume between the two circles with a 20 cm axial length, which would be the region seen with a single circular scan at the midplane. The figure shows that for any extended volume spacing, the stacked-FDK reconstruction from two separate circles deviates the most from the truth, and it degrades with increasing separation.

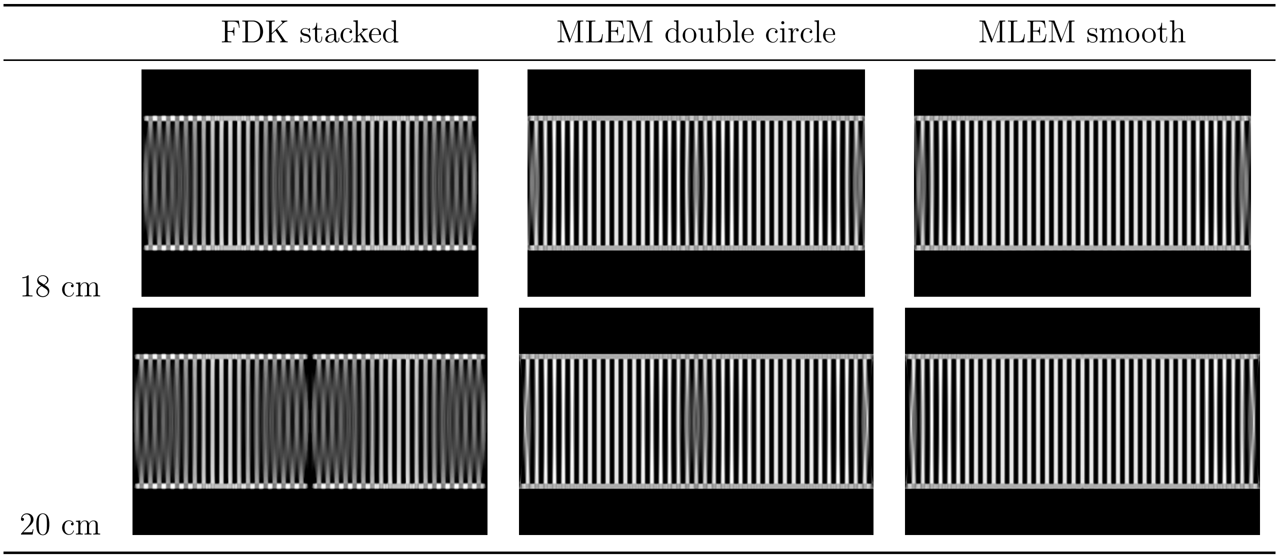

Figure 4.6: Mid-sagittal views of the simulated Defrise disk phantom reconstructions at different separation distances. The display window is [0.1, 0.3] cm^{-1}. The left column shows the stacked FDK extended volumes, and the remaining columns show the 100^{th} iteration of the MLEM extended volumes for different trajectories. In the stacked-FDK image at the maximum 20 cm spacing shown on the bottom left, the encroachment of the shadow zones into the reconstruction volume appear as two black wedges into the Defrise phantom volume.

Figure (4.5) also shows that the optimization-based reconstruction of the same dual-circle trajectory is much closer to the truth, but also demonstrates degradation with increasing spacing between the two circles. Finally, the CLC trajectory and the smooth trajectories reconstructions remain relatively constant for increasing spacing, with the smooth trajectory being closer to the truth. The slices shown in Figure (4.6) visually agree with these results. Notice that in the center of the volume, both the CLC and smooth trajectories are able to recover most of the alternating disks by acquiring some projections in the region between the circles. Furthermore, by acquiring these projections in the overlap region while also rotating as with the smooth trajectory, there is an additional improvement in this central region. The double circle and line trajectory was left out of Figure (4.6) since the results were not visually distinguishable from the smooth trajectory reconstructions.

4.3.2 Experimental data

Figure (4.7) shows the central sagittal slice from the stacked volume of the iTools FDK reconstruction of the dual-Catphan phantom scanned with a full-fan detector configuration. This is representative of the current clinical method of acquiring an extended axial FOV image though the axial spacing exceeds the axial support of FDK. Figure (4.8) shows the central sagittal slices of MLEM reconstructions of the same dual-Catphan configuration with each of the extended-axial-FOV trajectories in both the full-fan and half-fan detector configurations. The left column of the figure represents full-fan detector configuration scans, and the right column the half-fan detector configuration scans. From the top row to the bottom, these images correspond to the double circle, the CLC, and the smooth trajectory.

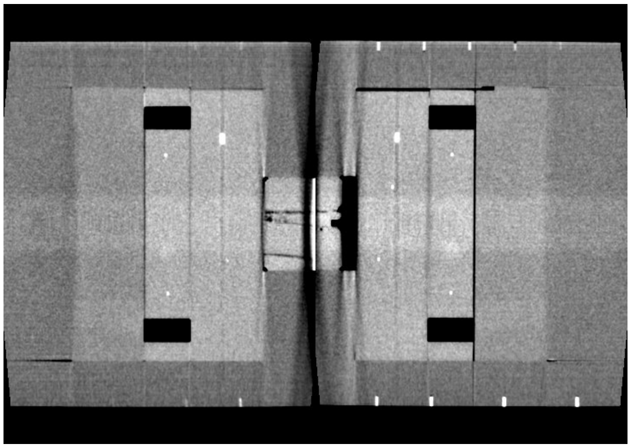

Figure 4.7: Sagittal slice of the stacked FDK volumes reconstructed independently with the iTools software. The two circular scans were acquired with a full-fan detector configuration. The display window is [-160, 240] HU.

We first investigated the quantitative Hounsfield units (HU) from the different sensitometry modules. Figure (4.9) shows the mean ROI value for each of the Catphan sensitometry modules for the stacked FDK and the stacked MLEM reconstructions as well as the extended-axial-FOV reconstructions. The height of each of the bars is the standard deviation of the ROI. The first plot in Figure (4.9a) corresponds to the full-fan detector scans, and the bottom plot in Figure (4.9b) corresponds to the half-fan detector configuration.

In both Figures (4.9a) and (4.9b), we can see there is a consistent reproducibility between

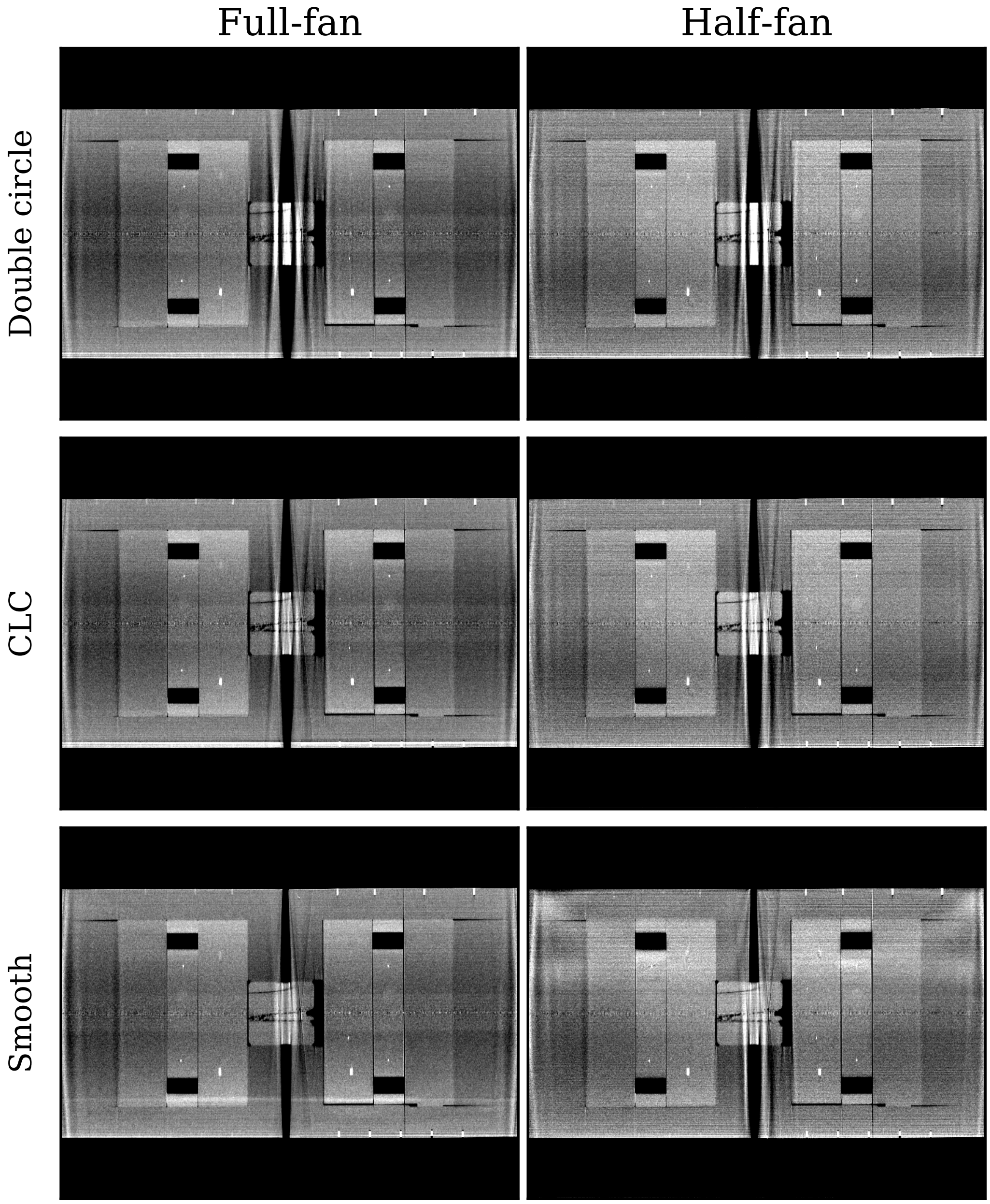

Figure 4.8: Sagittal slices of the dual-Catphan MLEM reconstruction acquired with the double-circle, the CLC, and the smooth trajectories (in order from top to bottom). The left column corresponds to the full-fan detector configuration, and the right column corresponds to the half-fan detector configuration. The display window is [-160, 240] HU.

the different scanning trajectories reconstructed with both the full-fan and half fan detector configurations. As the FDK reconstruction is from Varian's iTools software, it serves as a reference for the performance of current clinical reconstructions available from this LINAC-mounted CBCT imaging system. We used the Hounsfield values from the clinical reconstruction in the sensitometry module to determine a map from electron density to CT number that we then used to convert the MLEM reconstructions to Hounsfield units.

To further investigate the relationship between the full-fan and half-fan configuration as well as the algorithm used, we plotted the ROI values for just the stacked circle trajectories. As the introduction of additional trajectory components will be applicable for the optimization-based framework, this comparison simply provides a baseline of how MLEM directly compares to the clinical standard. Figure (4.10) shows the ROI CT numbers of both the FDK and MLEM reconstructions for both the full-fan and half-fan detector configurations. Again, each bar is centered on the mean CT number, and the height corresponds to the standard deviation of the ROI. Again, these plots server for comparison purposes between scans rather than illustrating the true CT number as even the clinical iTools reconstructions show a bias given as the CT number for water is not mapped to zero HU.

We then studied the impact the different scanning configurations and algorithms had on the spatial resolution of the reconstruction. Though the MTF is a problematic metric of spatial resolution in CT due to its violation of linear shift invariance, it can provide a useful benchmark for evaluating the impact different scanning parameters could have on the reconstruction's spatial resolution. By using different MTF metrics from different features in the Catphan, we could get an approximate characterization of how the different classes of trajectories reconstructed with our framework compare to the current clinical standard of stacked FDK.

The spatial resolution metrics we extracted from the dual-Catphan reconstructions from the different classes of trajectories are shown in Figure (4.11). This plot shows the different MTF values for the different algorithms with both the full and half-fan configuration. As

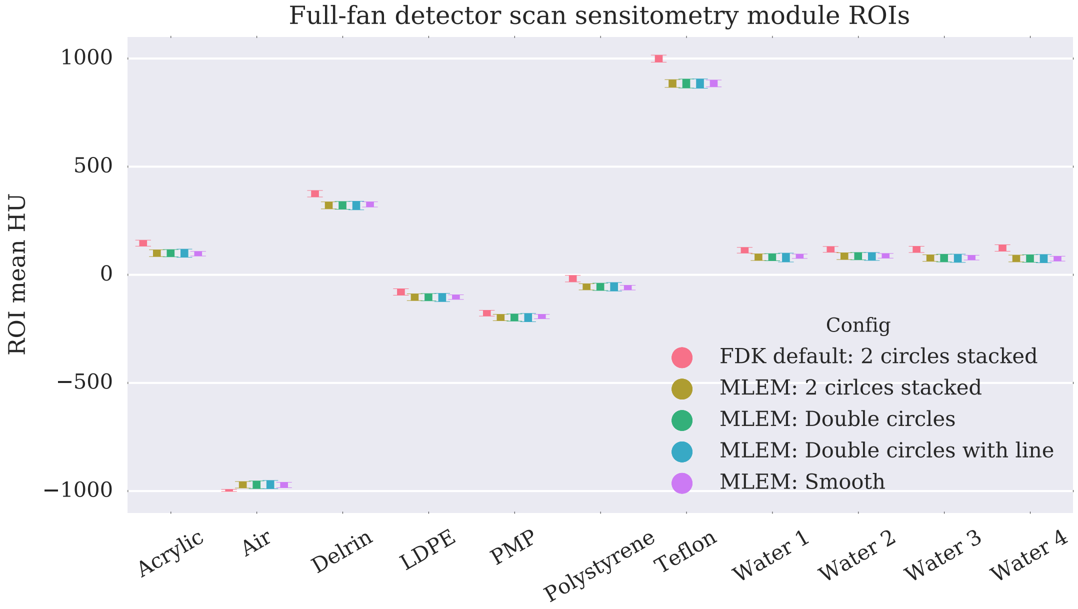

(a)

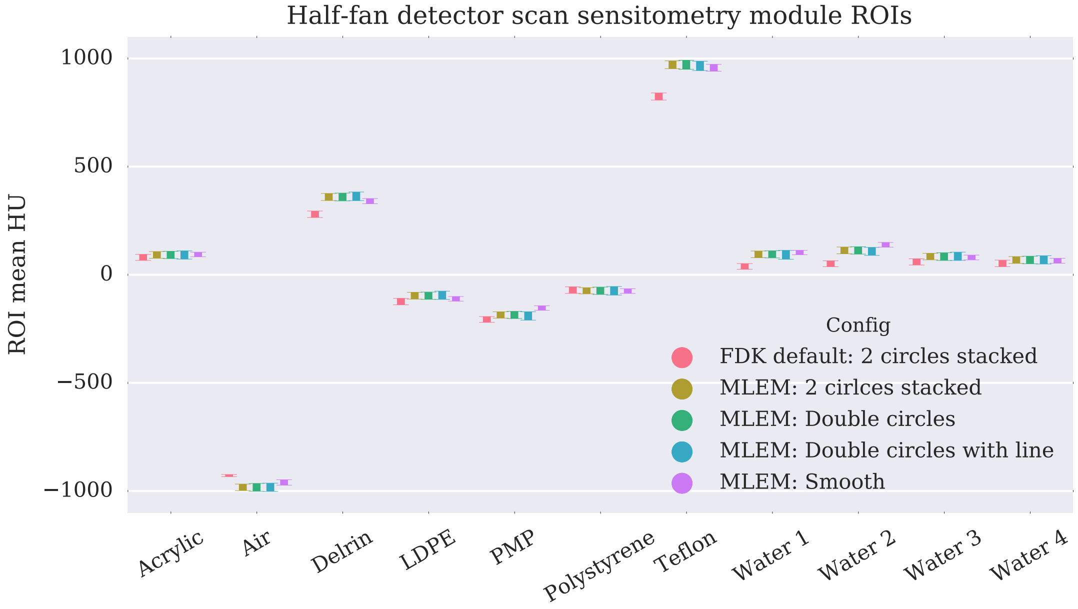

(b)

Figure 4.9: Plots of the Catphan CTP 404 sensitometry insert ROIs for the different classes of trajectories studied. Each bar in the plot is centered on the mean ROI value, and the height of the bar is the standard deviation of that ROI. The top plot (a) shows the ROI measurements for the full-fan detector scans, and the bottom plot (b) shows the corresponding measurements from the half-fan detector scans. For each material ROI, the different scanning trajectory results are presented from left to right in the same order listed in the legend.

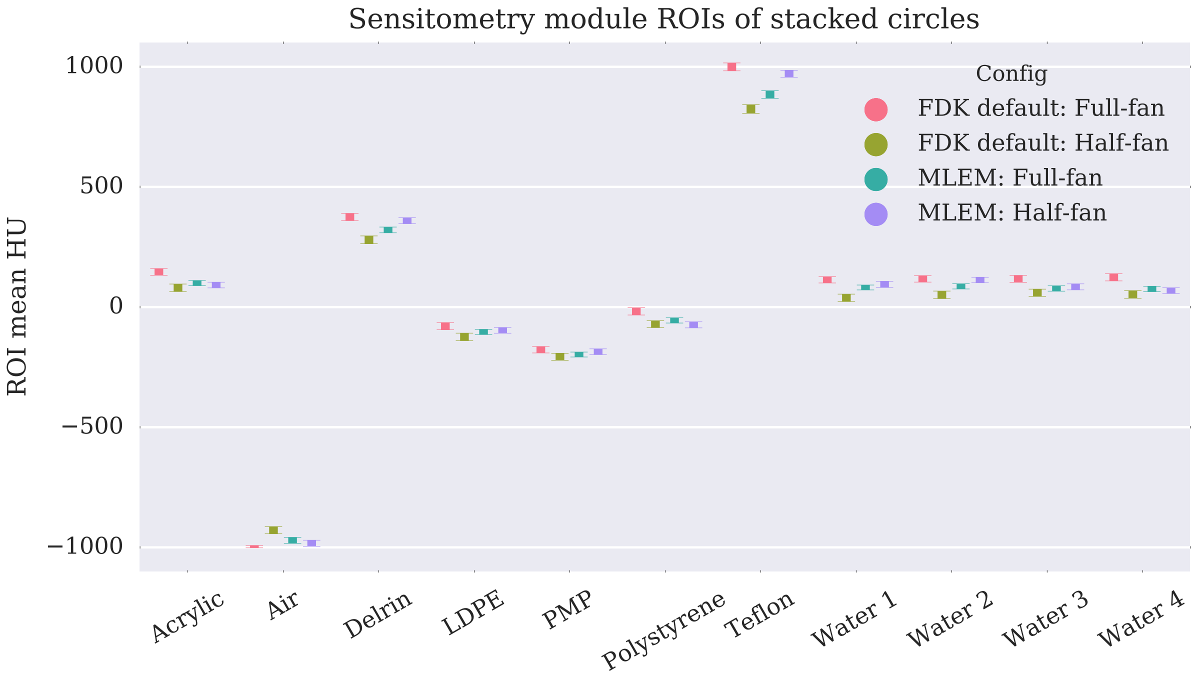

Figure 4.10: Comparison of the MLEM algorithm as a direct replacement of the current clinical method of axial-FOV extension by stacking two independently reconstructed circular scans together. These ROIs are measured from two independently reconstructed circular scans (both full and half fan) using MLEM and FDK. As in Figure (4.9), the bars are centered on the mean CT number of the ROI, and the height corresponds to the standard deviation in that ROI.

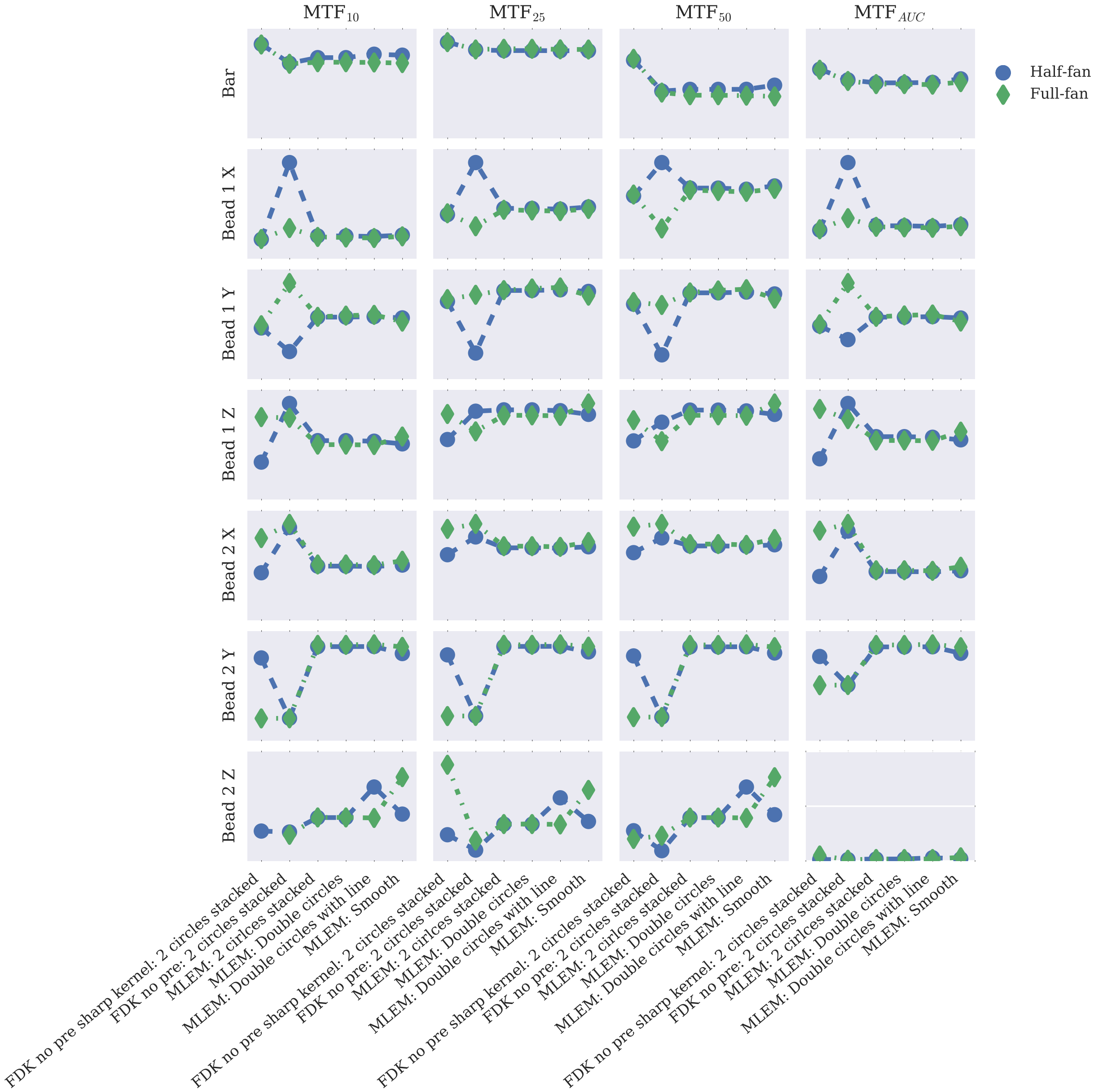

Figure 4.11: Grid of the different normalized spatial resolution metrics extracted from the MTF analysis of the dual-Catphan phantom scan using the different trajectory classes. The green points are the full-fan detector configuration and the blue points are the half-fan detector configuration. As CT lacks linear-shift invariance, these MTF metrics are shown only to illustrate the generally consistent spatial resolution beteween the different classes of trajectories reconstructed with MLEM and how this compares to the stacked FDK with both the standard and sharp kernels,

the lack of spatial-shift invariance in CT makes using the MTF metric only a rough estimate of spatial resolution performance, there are a few reconstructions where the metric values are somewhat anomalous.

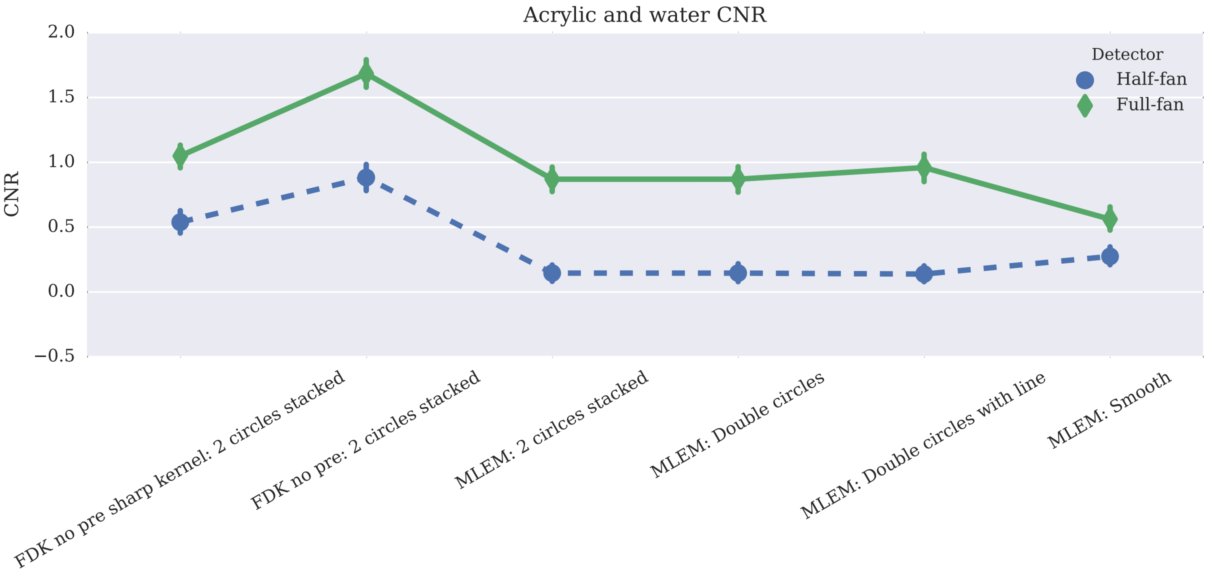

Figure 4.12: Acrylic CNR for FDK and MLEM with full-fan and half-fan detector configurations.

In addition to the spatial resolution metrics, we also used the CTP 404 sensitometry module to calculate the CNR of the acrylic, PMP, and polystyrene inserts. These are the inserts that provide the lowest contrast relative to the water-equivalent inserts as can be seen in the ROI measurements in Figure (4.9). Figures (4.12), (4.13), and (4.14) show the calculated CNR plots for the different algorithms and trajectories for both the full-fan and half-fan detector configurations for three different contrast plugs of acrylic, polymethylpentane (PMP), and polystyrene.

Finally, the reconstructed images of the anthropomorphic CIRS torso phantom provide a visual illustration of the three different trajectory classes. The rows in Figure (4.15) show the central sagittal, coronal, and transverse slices (from top to bottom respectively) of the CIRS torso phantom scanned with the three extended-axial-FOV trajectories using a half-fan detector configuration. Each column in the figure corresponds to one of the scanning

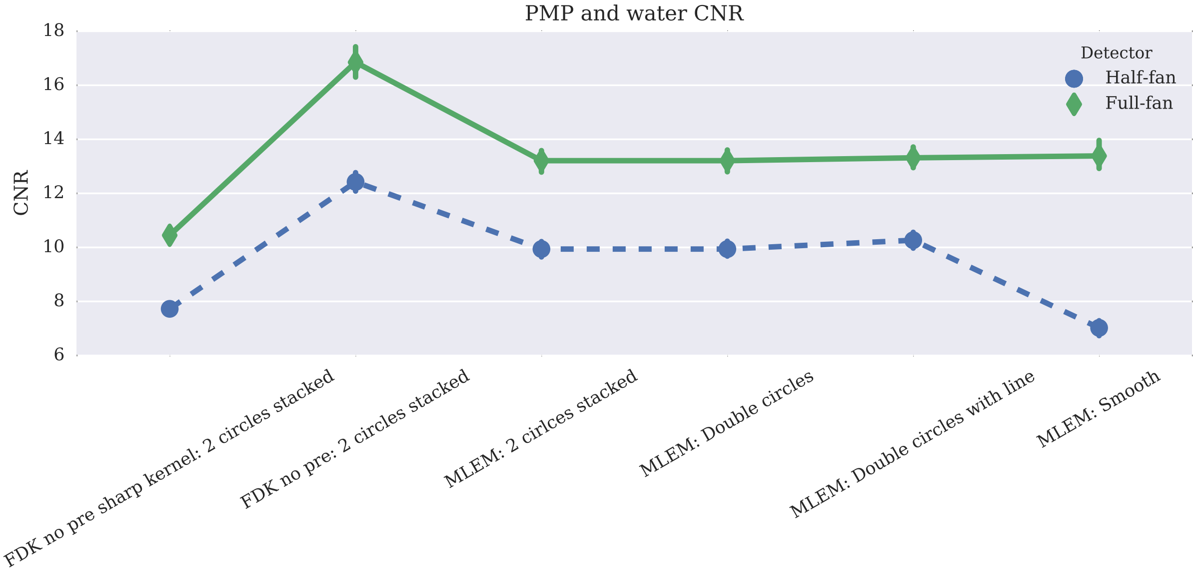

Figure 4.13: PMP CNR for FDK and MLEM with full-fan and half-fan detector configurations.

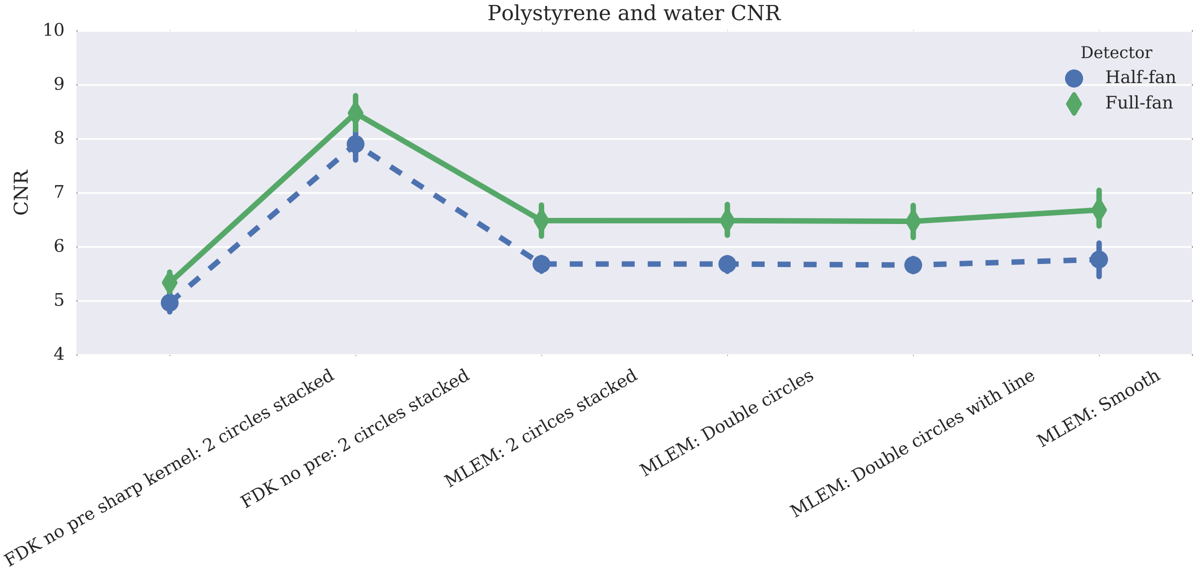

Figure 4.14: Polystyrene CNR for FDK and MLEM with full-fan and half-fan detector configurations.

trajectories.

4.4 Discussion

By increasing the separation between the two circular scans up to the maximum spacing of 20 cm, it is apparent that FDK has fundamental support limitations that restricts the acceptable distance between these two circles to less than the maximum 20 cm spacing due to the increasing size of the shadow zone with increased separation between the two planes of the circles. This is particularly problematic in that the infiltration of the shadow zones into the reconstruction volume occur in the region between the two circles. It is likely that if such an extended image volume were needed clinically, it would be axially centered on the region of interest. As such, using the stacked-FDK method for these larger axial volumes would place the region of interest directly in the overlap region where FDK is plagued by both cone-angle artifacts and the shadow zone.

Optimization-based reconstruction methods can use information from both circular scans simultaneously, leading to improved reconstruction of the image in the shadow zone as seen in Figure (4.6). However, as it can be seen in Figure (4.2), artifacts can still appear in the overlap region even with optimization based method. The streaking is particularly noticeable in these results for two reasons.

The first issue is the fact that there is a sharp density change in the axial direction much like the difficult Defrise-like phantom design we used in simulation. We made an effort to minimize this drastic density change from the Catphan to air and then directly back to the Catphan by inserting a urethane plug we machined to fit in the ends of the two phantoms. In addition to this, we also sandwiched a foam disk in the region to attempt to fill the flush concavities of the two Catphan tops.

Another problem with this particular data is related to contamination of the beam at the edge of the axial FOV from the collimator blade appearing in the FOV. Though this collimator blade would be slightly inconvenient in a typical circular scan, it would not be

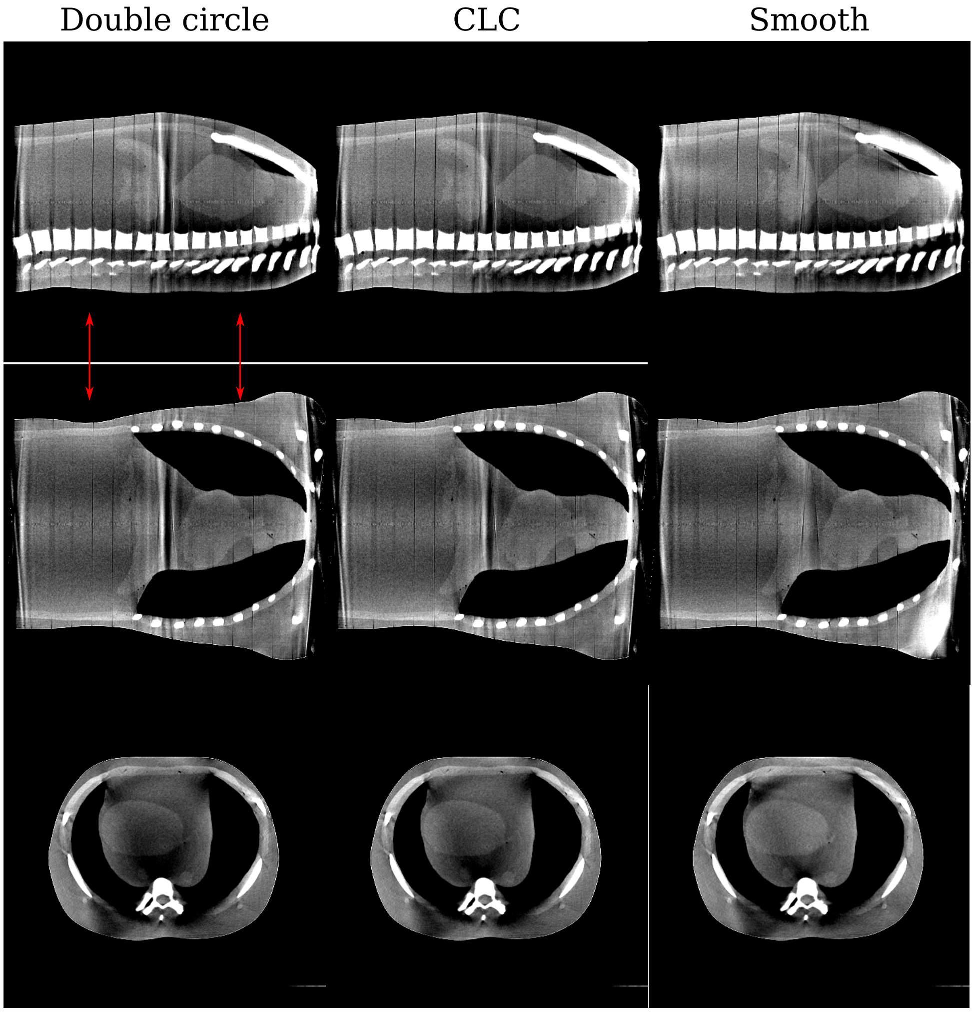

Figure 4.15: Sagittal, coronal, and transverse slices of the CIRS torso phantom reconstructions. Given the increased size of this anthropomorphic phantom, only the half-fan configuration was used as the full-fan configuration would have incurred truncation artifacts. The display window is [-160, 240] HU. The red arrows indicate the axial location of the two planes of the source's circular component of the different trajectories, and is applicable for the first two rows.

excessively problematic as it would appear in the region typically affected by cone-angle artifacts. Here however, as the edge of the axial FOV appears in the center of the image, this additional source of inconsistency exacerbates an already challenging feature to reconstruct with a CBCT system.

For future work on this particular use of non-circular trajectories, it would first be beneficial to ensure the collimator blades do encroach onto the detector. Especially along the axial extremes of the detector as that will contaminate what would probably be the region of most interest. It would also be nice to place an image quality module in the overlap region to evaluate the image quality that this method would be able to provide without the collimator blade contamination.

Despite the limitations of this study, the decision to place the image quality modules at the axial position of the circle's source plane gives an upper limit on what FDK can reasonably achieve, even as a standalone circular scan comparison. By evaluating the two algorithms at a location where FDK does satisfy Tuy's condition, we can see in the results that MLEM can do just as well if not better than FDK.

For example, in the comparison of the stacked, independently-reconstructed, dual-circle trajectories using both algorithms, it can be seen that FDk fails to be consistent with itself in the full-fan versus half-fan configuration. As Figure (4.10) shows, the CT numbers for the FDK with the different detector configuration do not agree with each other. The two detector configurations for MLEM however, not only are consistent with each other, but they also fall between the two extremes bracketed by the FDK results which ought to be the same number.

The MTF results shown in Figure (4.11) also reflect a consistency among the different classes of scanning trajectories reconstructed with MLEM. Though the difficulty of MTF metrics in CT introduce some nonsensical outiers, we can see that the MLEM reconstructions perform as well as the standard FDK, and that the sharper kernel does produce better spatial resolution. This is best illustrated by the top row of Figure (4.11) that shows the bar pattern

MTF results which are more robust to the violation of linear-shift invariance.

Similarly, the CNR results shown in Figures (4.12), (4.13), and (4.14) demonstrate the same consistency for the MLEM reconstructions of the different trajectory classes. As expected, the increased spatial resolution of the sharp kernel in FDK is accompanied by a loss of contrast. Other than the very low-contrast acrylic CNR, the FDK results using the two kernels bracket the MLEM reconstruction results. Again, we only wish to illustrate that these new trajectories with optimization-based reconstruction can perform as well as the current clinical standard.

Finally, it is important to point out that for the smooth trajectory, the half-fan configuration does not provide complete support when using the half-fan detector configuration. In a full-fan configuration, the typical π-plus-fan-angle angular coverage provides sufficient projection data. With the half-fan configuration however, this is not the case; so as the axial-translation component of the trajectory begins, there is insufficient support at the axial extremes of the entire extended image.

However, as both the simulation and experimental results show, distributing some of the angular coverage during the translation does help to improve the image quality in the overlap region. As we have mentioned, this would probably be the region of most interest if a technique like this were used in the clinic. Therefore, while the axial extremes of the extended volume are degraded, as can be seen in Figure (4.15) especially in the shoulders of the torso phantom, the streaking in the overlap region is significantly reduced as opposed to the double circle and CLC trajectories. Therefore, if using a half-fan configuration with such a trajectory, care must be take to determine which part of the tomographic image requires higher fidelity.

4.5 Conclusion

We found that the use of our optimization-based, non-circular scanning trajectories could successfully reconstruct extended-axial-FOV reconstructions that are comparable to the current clinical image quality achieved with a circular scan and FDK. In addition to being able to maintain comparable image quality in the region where FDK performs the best, our framework was able to extend the axial-FOV coverage beyond the axial separation distances allowed to FDK by the fundamental limitations of its support. Our hypothesis that our optimization-based reconstruction framework could reconstruct from extended axial coverage non-circular trajectories was correct. We also found that the image quality from these reconstructions was at least as good as the current clinical standard. Though additional studies need to be conducted to perform quantitative image quality analysis in the overlap region, we do know this framework provides a feasible means addressing the limited axial FOV coverage that currently affects the clinical use of CBCT in IGRT.

CHAPTER 5

COLLISION-AVOIDING TRAJECTORIES

5.1 Introduction

Given the clinical benefits provided by the LINAC-mounted CBCT sytem, it is detrimental when adequate tomographic information cannot be obtained from the kV-imaging CBCT system. One such situation is when a collision between the patient and the machine arises. While there has been substantial work done aimed at the detection and avoidance of collisions in treatment delivery [30, 11, 75, 52, 29, 2, 56, 57], the methods are often insufficient for standard CBCT imaging because they generally seek to avoid collisions preventing ideal treatment positions and preventing complete collection of tomographic image information. A generalized imaging framework such as the one we use may allow for the use of patient-specific collision-avoiding CBCT trajectories..

Collision avoiding trajectories may be of particular concern in breast and lung cancer patients where the arm position increases the likelihood of potential collisions as shown in Figure (5.1). Collisions also present a problem in treatment of posterior and lateral lesions in stereotactic body radiosurgery (SBRT). Similarly in prone breast treatments, where the target is near the couch top and a lateral couch translation is needed to bring the target to isocenter, collision with the contralateral side of the patient may occur. When collisions do occur, the angular range available for scanning is restricted and it is not possible to acquire a complete circular scan in the treatment position.

To avoid collisions with the LINAC head, it might be desirable to move the patient away from the gantry by translating the couch. To avoid collisions with the imaging panel, the patient might also be moved away from the panel. As many LINAC-mounted, kV-imaging panels have motion capabilities, another solution would be to move the imager away from the patient in the collision zone, which changes the imaging magnification for that portion of the scan. Given that the clearance distance of the kV-imaging panel is not much larger

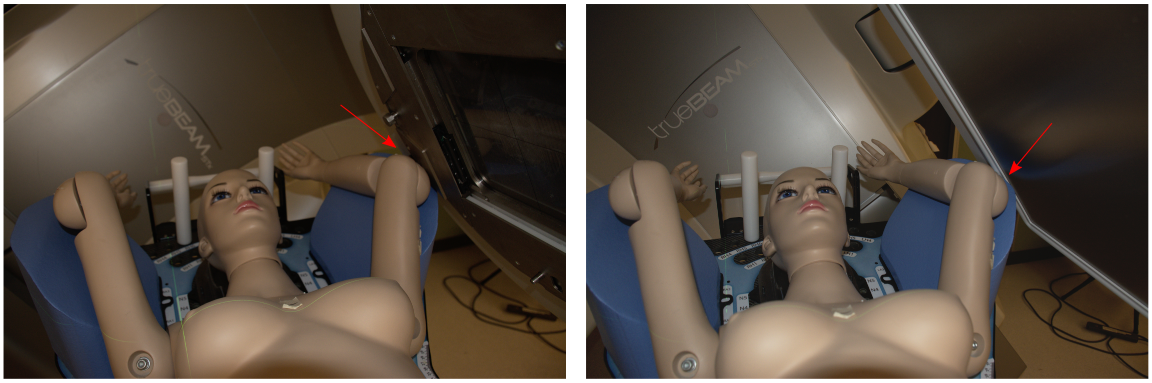
(a) (b)

Figure 5.1: Two examples of potential collision for a typical patient setup using a mannequin in a supine treatment position. As can be seen, collisions can occur both with the face of the MV treatment head (distance 41.7 cm from isocenter for this LINAC) and with the kV detector (distance 45-70 cm from isocenter, depending on magnification).

than that of the MV-treatment head, a collision avoidance solution should account for both of these components.

Here, we investigate trajectories that could allow the acquisition of sufficient projection information for a clinically useful image while avoiding a potential patient collision with the gantry such as those shown in Figure (5.1). One trajectory that would avoid a patient collision with the MV-treatment head is a virtual isocenter trajectory, which increases the effective source-to-axis distance (SAD) for all gantry angles. By using this increased SAD for an imaging trajectory, the clearance between the patient and the MV-treatment head as the gantry rotates is increased and the collision is avoided.

The virtual isocenter trajectory utilizes synchronized gantry rotation and couch translation to maintain a fixed distance ("virtual SAD") between the MV source and a chosen center of rotation ("virtual isocenter") in the patient as shown by the red circle in Figure (5.2). At the beginning of the scan, the patient is moved away from the LINAC head along the MV beam direction. As the gantry rotates, the couch moves continuously to maintain the specified separation as shown in Figure (5.2). The virtual SAD can be chosen large enough such that collisions as shown in Figure (5.1a) are avoided; at this point in the trajectory, the couch would have moved far enough to the left to avoid the collision. Note that it is only

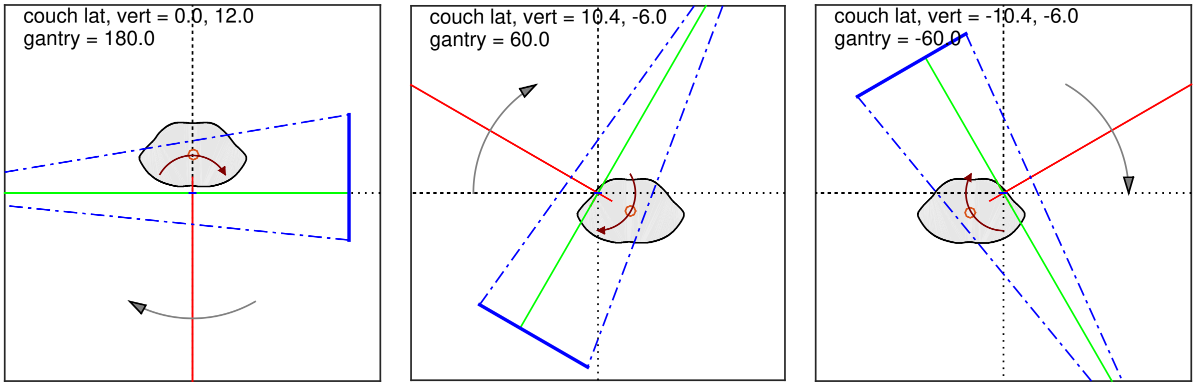

Figure 5.2: Patient, kV and MV beams and kV detector at several angles during a virtual isocenter rotation. Room coordinate system (dotted axes) has its origin at mechanical isocenter, also the intersection of the MV (red) and kV (green) beam axes. As the gantry rotates, the patient (filled contour) is continually shifted to maintain a specified distance along the MV beam direction between the mechanical isocenter and the chosen virtual isocenter (circle symbol within the patient). The path of the virtual isocenter is a circle about the mechanical isocenter, with radius equal to the chosen shift (12 cm from the isocenter in this example). Detector may or may not be shifted as shown, depending on virtual isocenter position and patient geometry.

the distance to the LINAC head that is increased in the virtual SAD technique; the distance from the kV source and detector to the patient and to each other are unchanged.

Another trajectory that could avoid a patient collision with the kV detector would be one during which either the patient or the detector is moved during the scan in the angular range of a collision. Either solution leads to changing kV-CBCT imaging magnification during the acquisition. Again, optimization-based reconstruction methods can readily handle such a change in magnification provided the projection information is correctly incorporated into the system matrix.

Finally, we study a trajectory that combines virtual isocenter and dynamic magnification trajectories to create a hybrid scanning acquisition that could alleviate collisions with both the MV-treatment head and the kV-CBCT detector. With such a trajectory, the potential collisions with both the LINAC head and the kV detector panel are resolved. We use such a trajectory as an example of a patient-specific scanning trajectory that could be implemented to resolve potential collisions with two components of the LINAC treatment system.

5.2 Methods and Materials

5.2.1 Scans

For the circular scans, the gantry made a full rotation about the patient with the treatment volume at a fixed mechanical SAD of 100 cm. For the virtual isocenter scans, the patient couch was translated continuously in the gantry rotation plane during gantry rotation to maintain a distance of 112 cm between the MV source and the chosen target point within the treatment volume (the "virtual isocenter"), rather than the mechanical SAD of 100 cm as shown in Figure (5.2). We generated all of the scanning trajectories in this study using the Developer Mode 2.0 XML schema to define the positions of the gantry, the kV imaging arms, and the patient treatment table. The schema was also used to enable kV-projection imaging during the scan. We used a half-fan detector configuration with a 13 cm offset for the circular acquisition, and an equivalent offset for the virtual isocenter to obtain the same illumination.

To increase the clearance between the kV detector and the patient, we increased the radius of the kV detector with accompanying increase in magnification of the kV imaging system. Currently, the detector positioning arm cannot be moved while the gantry rotates. Thus, to create projection datasets where the detector distance changes during a scan, we acquired multiple scans using different detector positions and subsequently spliced these together to create the sinograms of interest with the corresponding system matrix $\mathcal{H}$. This allowed us to create different dynamic magnification scan datasets. We acquired both circular and virtual isocenter trajectories with detector positions of 50 cm, 60 cm and 70 cm away from the mechanical isocenter for magnifications of 1.5X, 1.6X and 1.7X respectively. In each case, the detector cover is 5 cm closer to the patient than the CsI layer, potentially leading to collisions with the limits shown in the first plot in Figure (5.3).

To create the combined sinogram of a hypothetical collision-avoiding dynamic magnification scan, we replaced a 45° region of the 1.5X circular scan with the corresponding angular

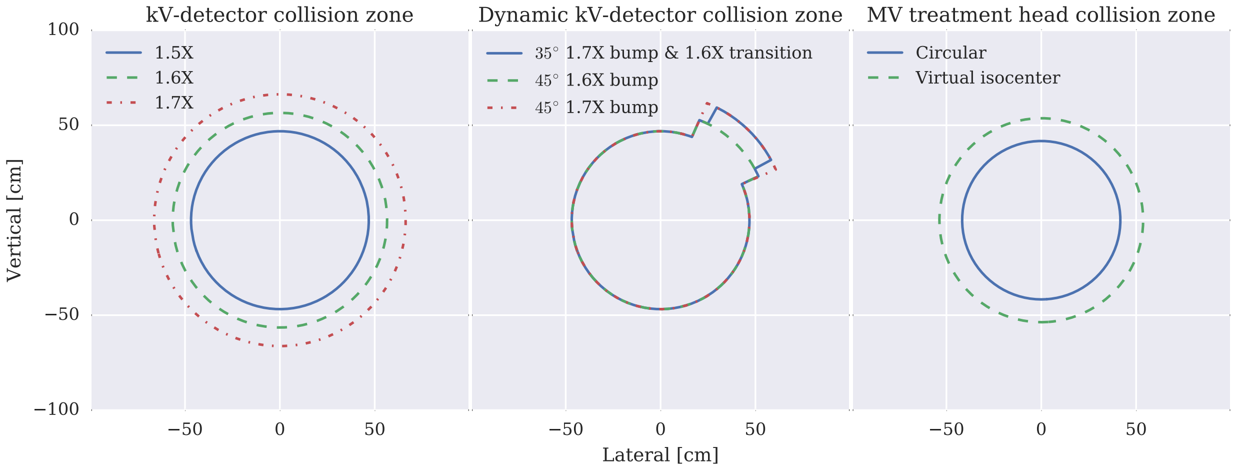

Figure 5.3: Collision zones in the patient image space for the kV detector cover and the MV treatment head accessory mount. The left figure shows the increasing radius of the kV-detector collision zone with an increase in magnification. The middle figure shows the increased radius of the kV-detector collision zone for the two dynamic magnification trajectories utilizing a 45° bump at a higher magnification. The right figure shows the increased radius of the MV-treatment-head collision zone when using the virtual isocenter scanning trajectory.

range from scans at different magnifications. We chose this region to be centered on the angular position corresponding to the mannequin's elbow in Figure (5.1). Increasing the magnification in this region corresponds to increasing the clearance between the kV-detector and the patient. Increasing the magnification to 1.6X and 1.7X provides an additional 10 cm and 20 cm of clearance respectively. We also created an additional 35° 1.7X bump magnification with 5° transitions at a 1.6X magnification. The kV-detector collision zones of these dynamic magnification trajectories are shown in the middle plot shown in Figure (5.3).

The virtual isocenter imaging trajectory would alleviate the potential collision with the MV treatment head accessory mount shown in Figure (5.1a). The radius of the accessory mount from the mechanical isocenter is 41.7 cm. Using a virtual isocenter would increase the radius of the collision zone by 12cm to alleviate potential collisions (as shown in (5.3)). Utilizing a different virtual SAD would allow for additional clearance if necessary.

The last set of trajectories we studied combines the dynamic magnification with the virtual isocenter trajectory. As the collision radius with the MV treatment head and the kV detector are similar for the current clinical scan trajectories, collisions with either could arise. By combining the change in magnification with the virtual isocenter trajectory, both collision zones could be avoided. Table (5.1) shows the different scans investigated in this study.

Table 5.1: Scanning trajectories

Trajectory	Magnification
Circle	1.5X
	1.5X & 45° 1.6X bump
	1.5X & 45° 1.7X bump
	1.5X & 35° 1.7X bump, 1.6X transitions
Virtual isocenter	1.5X
	1.5X & 45° 1.6X bump
	1.5X & 45° 1.7X bump
	1.5X & 35° 1.7X bump, 1.6X transitions

5.2.2 Generalized-trajectory framework detector offset

When applying the generalized-reconstruction framework discussed in *Framework implementation with Varian TrueBeam kV-CBCT system* to this specific non-circular trajectory case of collision avoidance, care must be taken to correctly transform the coordinate system of the imaging geometry to ensure the desired detector offset is used. In the case of utilizing the virtual isocenter to prevent potential patient collisions with the LINAC treatment head using an offset detector, we used the following formulation of the framework to calculate the detector offset for the virtual isocenter trajectory that would provide equivalent projective illumination of the patient onto the detector as that of a standard circular scanning configuration.

As shown in Figure (5.4), using a virtual isocenter at a distance R_v from the mechanical isocenter results in the virtual isocenter projecting to a different location on the detector. The red arrow in the image indicates the projection of the mechanical isocenter onto the detector whereas the blue arrow indicates the projective location of the virtual isocenter onto the detector. If using a detector of width w with a full-fan configuration relative to the

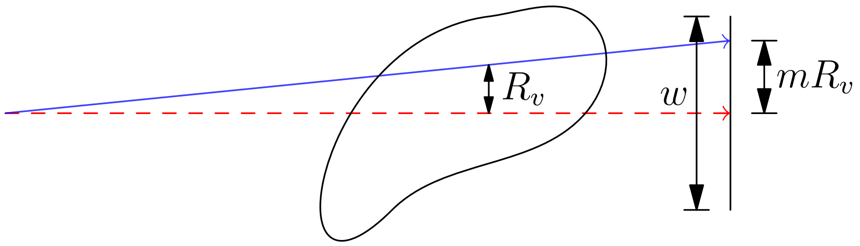

Figure 5.4: Schematic showing the offset between projecting the virtual isocenter (blue) and the mechanical isocenter (red) onto the detector. By implementing a virtual isocenter offset of R_v, the projection of this new virtual isocenter onto the detector of width w is a function of the magnification (m) and is indicated by the blue arrow. The projection of the mechanical isocenter onto the detector is represented by the red arrow.

mechanical isocenter, this is effectively a half-fan configuration with a lateral offset of mR_v in the virtual isocenter image space for a magnification m.

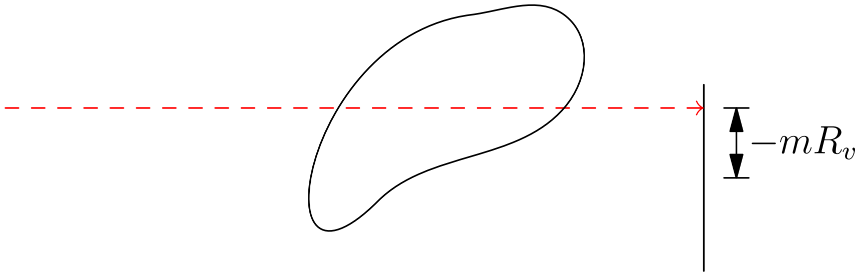

Figure 5.5: If using the effective lateral detector offset for the virtual isocenter configuration shown in Figure (5.4), a lateral detector offset of $-mR_v$ would be necessary to achieve the same illumination geometry for a circular canning trajectory around the mechanical isocenter.

If the lateral offset mR_v in the virtual-isocenter image space is the desired offset, then the lateral detector offset for the circular scan must be changed in the opposite lateral direction to achieve equivalent illumination of the object on the detector. Figure (5.5) shows such an example of the lateral offset needed for achieving the equivalent illumination of the object on the detector as the virtual isocenter configuration shown in Figure (5.4).

However, it is also possible to calculate the virtual-isocenter lateral offset (δ) to achieve

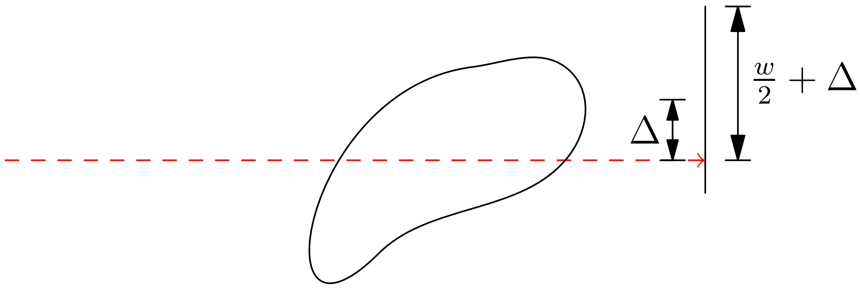

Figure 5.6: For a typical half-fan detector configuration for a circular scan, a lateral offset of Δ is chosen.

the same illumination geometry as a half-fan detector configuration for a circular scanning trajectory with a lateral offset (Δ). As the circular scanning trajectory with a half-fan detector configuration is used clinically, as shown in Figure (5.6), this is also the approach we used. For each virtual isocenter scan a given magnification, we calculated the lateral offset to achieve similar projective illumination on the detector.

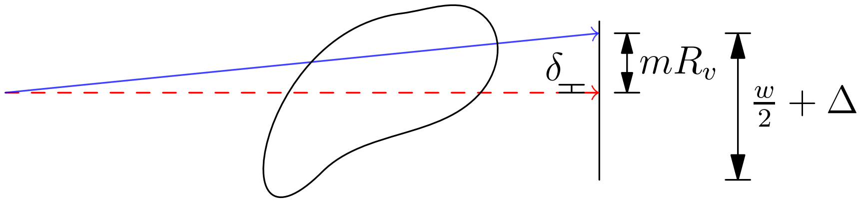

Figure 5.7: To achieve the equivalent detector support for the circular trajectory lateral offset (Δ) in Figure (5.6), a lateral offset of δ must be used.

Once the desired lateral offset (Δ) was chosen for the half-fan detector configuration, we then calculated the virtual-isocenter offset as

$$\delta = mR_v - \Delta. \tag{5.1}$$

By then utilizing this offset, we could replicate the projection of the virtual isocenter onto the detector as using the offset (Δ) in Figure(5.6). With this choice of lateral offset, the virtual isocenter is then projected onto the detector as illustrated in Figure (5.7).

5.2.3 Reconstruction

The addition of couch motion to the imaging trajectory does increase the degrees of freedom for which proper geometric calibration must be acquired. Using the methods described in the chapter *Geometric calibration*, we computed corrections to the nominal reported couch, source and detector positions for each of the tested trajectories.

We reconstructed all of these fixed magnification and dynamic magnification scans from circular and virtual isocenter trajectories into the patient image space described by the imaging model in Equation (2.6). The Catphan scans were reconstructed onto an isotropic voxel size of 0.473 mm. The CIRS torso scans were reconstructed onto an isotropic voxel size of 0.836 mm. As the circular acquisition with 1.5X magnification is the typical clinical acquisition trajectory, this provides a clinical reference volume for the reconstructions from the other scanning configurations.

For the number of iterations in our reconstruction program, we selected 200 iterations as subsequent improvements in spatial resolution with further iterations were diminished. This is shown in Figure (5.8) which plots as a function of iteration numnber the 25% and 50% crossing spatial frequencies of the modular transfer function (MTF) and the area under the curve (AUC) of the MTF. The MTF was found using the edge spread function from the MLEM reconstruction of the Catphan phantom acquired with a circular scan at 1.5X magnification.

5.3 Results

Figure (5.9) shows slices of the CTP 528 spatial-resolution module from the 200$^{\text{th}}$ iteration of the MLEM reconstructions of the Catphan phantom for the different scanning trajectories. The top row shows reconstructions from the circular scanning trajectories, and the bottom

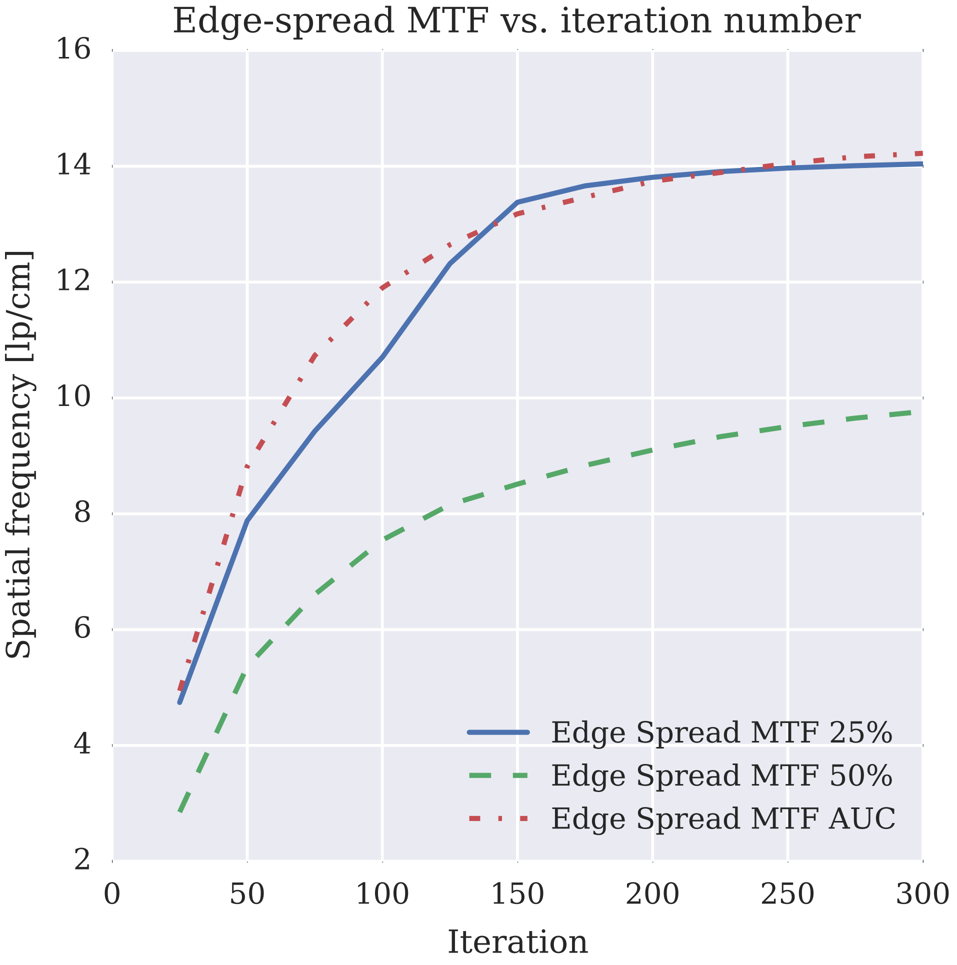

Figure 5.8: Plot of the Catphan's edge-spread function MTF at 50% and 25% as well as the MTF AUC for the clinical circular 1.5X half-fan scan. The effectie plateau in these spatial resolution metrics at 200 iterations is why we selected this as the fixed iteration number for all of our reconstructions.

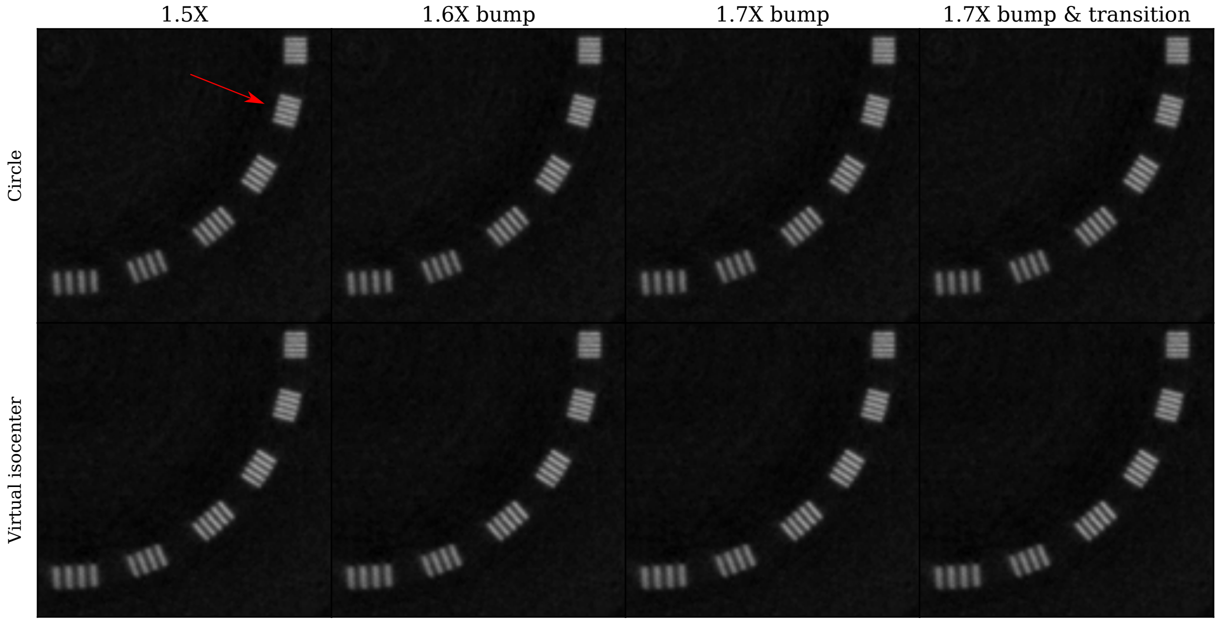

Figure 5.9: Images of the Catphan 528 spatial resolution module in a display window of [-100, 2000] HU. The top row shows all the circular scan permutations while the bottom row shows those of the virtual isocenter. The columns show different magnification combinations from left to right of 1.5X only, 1.5X with a 1.6X bump, 1.5X with a 1.7X bump, and a 1.5X with a 1.7X bump and a 1.6X transition on either side. For all of the reconstructions, the 8th largest gauge is resolvable (indicated by the red arrow).

row shows reconstructions from the virtual isocenter trajectories. The left column is from a single 1.5X magnification, and the remaining columns are different synthesized trajectories with different magnifications as illustrated in Figure (5.3). In all of these images, the 8th largest gauge is visually resolvable.

The visual similarity in the spatial resolution shown in Figure (5.9) is reflected in the MTF metrics for all of the different scanning configurations. We compared MTF metrics derived from the PSF using the Catphan beads, the bar pattern shown in Figure (5.9), and the edge-spread function (ESF) measure along an ensemble of radial lines. When comparing these MTF-based metrics between the circle and the virtual isocenter scans with different magnifications, we found no clear trend distinguishing the different trajectories.

Figure (5.10) shows the low-contrast CNR from the Catphan with these different imaging configurations which are also in good agreement with each other. In addition to using the

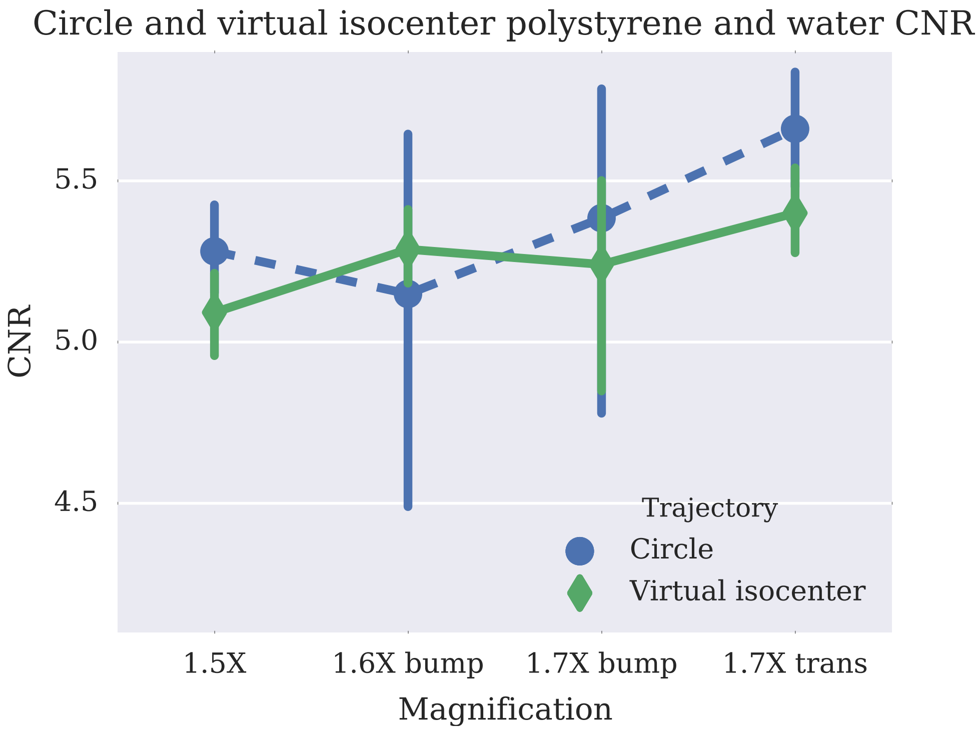

Figure 5.10: Plot of low-contrast polystyrene CNR and error bars corresponding to ± one standard deviation of the CNR from the Catphan scanned with both the circular and virtual isocenter trajectories.

material rods in the CTP 404 sensitometry module to calculate the CNR, we also compared mean values from each of the materials for the different scanning trajectories and magnifications. Figure (5.11a) shows the ROI means for these different scanning configurations. The height of the bar represents the standard deviation of the ROI. The first four bars for each material are from the circular scans, and the remaining four from the virtual isocenter scans.

Figure (5.12) shows an abdominal slice from the 200^{th} iteration MLEM reconstruction of the CIRS torso phantom scanned with a 13 cm offset half-fan configuration. The layout of these images is the same as that in Figure (5.9) with the top row showing magnification variations from the circular trajectory. The bottom row shows the corresponding magnifications from the virtual isocenter trajectory. The slice is the same as that in Figure (5.11b) which we used to calculate values for three organ ROIs.

For the different organ ROIs, we recorded the means and standard deviations for the different scanning trajectories and magnifications. Figure (5.11b) shows these mean values and the associated standard deviations. Though the circular scan variations fluctuate more than the virtual isocenter scans, the values are in agreement for the different organs of interest. As with Figure (5.11a), the first four points for each organ are from the circular scan, and the remaining four are from the virtual isocenter trajectory.

5.4 Discussion

As mentioned earlier, the virtual isocenter trajectory is designed to increase the distance between the gantry head and the patient by synchronized table translation and gantry motion. The geometry of the imaging arms remains unchanged, though the center of the image space is moved from the mechanical isocenter to the virtual isocenter. As shown in the previous section, this results in CBCT image quality that is comparable to a normal circular scan.

It is certainly possible to envision situations in which collisions with the kV imaging source or (more likely) the detector also occur. The system matrix in our optimization-based reconstruction method can incorporate changes in the position of the imaging arms

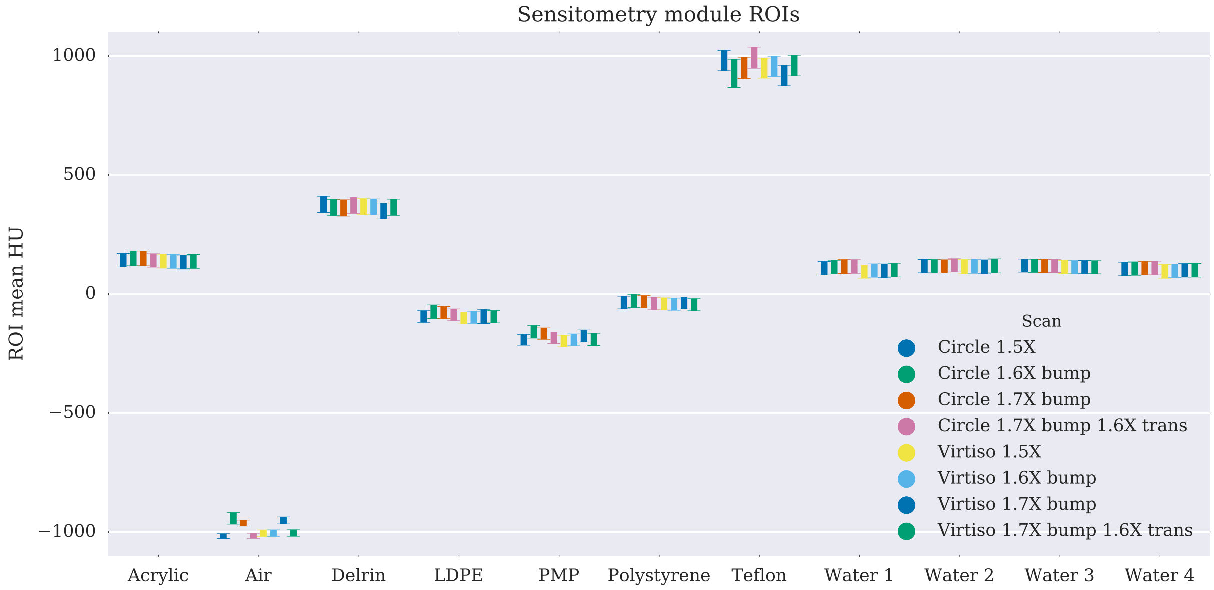

(a)

(b)

Figure 5.11: ROI material comaprison results for the Catphan CTP 404 module and the CIRS torso phantom. The height of the bars are ± one standard deviation of the ROI mean. The first four bars for each material ROI are from the circular scans, and the remaining four bars for each material ROI are from the virtual isocenter scans. The order of the scans for each material ROI are displayed in the order listed in the legend in (a) from left to right.

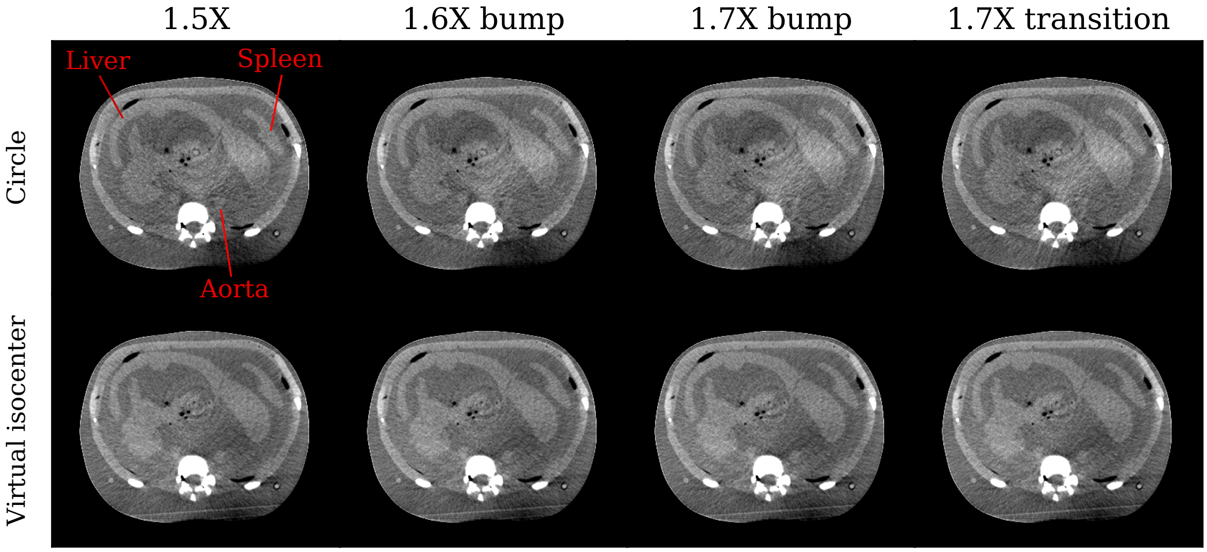

Figure 5.12: Images of the CIRS torso phantom's abdomen in a display window of display window of [-100, 200] HU. The top row shows all the circular scan permutations while the bottom row shows those of the virtual isocenter. The columns show different magnification combinations from left to right of 1.5X only, 1.5X with a 1.6X bump, 1.5X with a 1.7X bump, and a 1.5X with a 1.7X bump and a 1.6X transition on either side.

as well as the patient position. Thus a trajectory with variable source-detector distance, caused by the detector moving to avoid a patient collision, can also be reconstructed. Such a variable magnification scan may be performed with the patient couch moving in a virtual isocenter trajectory, or with the patient couch fixed and rotation about the physical machine isocenter.

All virtual isocenter scanning in the present work was done in TrueBeam Developer Mode, which is a strictly nonclinical mode of operation. Simultaneous motion of couch, gantry and imaging arms is not fully supported by the TrueBeam; however, the motions required for the virtual isocenter scan, which involve only coupled gantry rotation and couch translation, are feasible in Developer Mode. Although the LINAC can clearly execute the required motions and acquire the images, virtual isocenter scanning is as yet not available as a clinical capability. In addition, these scans must be reconstructed using iterative optimization-based methods, rather than the current clinically available filtered back-projection method. A historic concern about optimization-based methods has been reconstruction speed. These are very computationally intensive programs, but with the recent availability of GPU-based processing, reconstruction times are more manageable.

5.5 Conclusion

Virtual isocenter trajectories and dynamic magnification are potentially useful as collision-avoiding alternatives to standard isocentric rotation, both in cases where arc treatments are being delivered and in cases where CBCT scanning is desirable, but a normal isocentric scan could cause gantry-patient collisions. Using optimization-based reconstruction methods, patient-specific, collision avoiding imaging trajectories that utilize virtual isocenter CBCT scans and different kV-detector magnifications can be reconstructed by incorporating the view-by-view imaging and patient geometry into the system matrix. Image quality, as characterized by spatial resolution and low contrast object detectability, is comparable for virtual isocenter scans and for standard isocentric scans using different magnification bumps to avoid kV-detector collisions. Thus, virtual isocenter CBCT scans and kV-detector magnification changes could be combined with optimization-based reconstruction as a useful clinical approach in collision-plagued situations.

CHAPTER 6

CONCLUSIONS

In this dissertation work, we developed a framework that leverages optimization-based reconstruction methods to enable generalized, non-circular, scanning trajectories in CBCT. Where analytic-based reconstruction methods require a prescribed trajectory in order to derive an analytic inverse, optimization-based methods require no such assumption regarding the trajectory by which the projection views were acquired. This agnosticism of optimization-methods to the order and geometry by which projections are acquired allows for dynamic, view-by-view modifications to the scanning trajectory that would be untenable if the scanning trajectory were fixed by necessity of the reconstruction program's requirements.

We describe our generalized framework for reconstructing from generalized scanning trajectories using optimization-based reconstruction methods in *Chapter 2*. Though we limited ourselves to MLEM to solve our reconstruction problem, we by no means imply that this framework is dependent on this algorithm. Not only can other optimization-based algorithms be plugged into this framework, more sophisticated optimization techniques may be better suited to this optimization problem. However, regardless of the optimization-based algorithm employed in this paradigm, it is always critical that the user ensure that the parameters of the algorithm are carefully selected for the desired task.

In addition to developing this framework, we also developed a general calibration procedure in *Chapter 3* that would accommodate view-by-view corrections to the different non-circular trajectories we studied. We then proceeded to use this calibration protocol to make calibration corrections for the non-circular trajectory classes we studied in the subsequent chapters. Though optimization-based algorithms are very robust, the view-by-view agnosticism we utilize for our trajectory framework is only beneficial if the geometry describing each of the views in the system matrix is correct. As with all inverse problems, the answer provided by the inverse is only useful if you have solved the right problem.

As our investigation into different non-circular trajectories was motivated by existing clinical limitations currently encountered in using LINAC-mounted CBCT for IGRT, we then found two clinical examples where the ability to use non-circular trajectories could provide a solution. By first selecting two particular tasks to test our framework, we were able to constrain our investigation of the trajectory parameters that were relevant to solving these problems. Just as the parameters of the optimization program must be selected for the desired task, similar task-based considerations must be given to selecting what type of non-circular trajectory, if any, would be suited for intended application.

The first clinical limitation we studied in *Chapter 4* is the problem of the limited axial FOV provided by LINAC-mounted CBCT systems. Since the axial coverage provided by the CBCT detector is limited by engineering constraints, we hypothesized that non-circular trajectories would be able to extend the axial FOV while maintaining image quality that is comparable to current clinical methods. In addition to studying the double circle trajectory that is comparable to the current clinical practice of stacking the independently reconstructed FDK volumes of two circles together, we also studied the circle-line-circle and smooth trajectory classes that include acquiring projections as the CBCT imaging system translates between the two planes of the circular components of the scan. We found that not only does our framework with MLEM perform as well as FDK in the portion of the reconstructed volume where FDK satisfies Tuy's condition, but that it is also able to improve the image quality in the region between the planes of the source's circular orbit. Additionally, our framework demonstrated that it is possible to extend the axial spacing between the planes of the two circles into distances that exceed the support of two stacked FDK volumes.

The second clinical problem in using LINAC-mounted CBCT for IGRT that we investigated in *Chapter 5* is that of potential patient collisions with the LINAC when attempting to acquire a CBCT. For some of the treatment positions used for breast, lung, and head and neck cancer patients, the orientation of the patient on the treatment table puts them at risk of being hit by the LINAC as it rotates around the patient. In this study, we investigated different non-circular trajectories that could alleviate the different types of collisions potentially faced by these patients. One such trajectory would increase the radius of the kV-imaging detector in a potential collision zone to create a dynamic magnification trajectory. To avoid potential collisions with the LINAC treatment head, we studied a virtual isocenter trajectory that moved the patient couch while the gantry rotated to maintain a safe distance between the patient and treatment head to ensure no collision would take place. Finally, we created a trajectory that combined the virtual isocenter trajectory with the dynamic magnification in order to create a trajectory that could alleviate collisions with both the kV-detector and the treatment head. For each of these different configurations, we showed we could obtain reconstructions with image quality comparable to the standard clinical circular trajectory.

In conclusion, we found that our non-circular scanning trajectory framework using optimization-based reconstruction methods have the potential to address limitation of LINAC-mounted CBCT for IGRT. We selected specific non-circular trajectories that we knew had the potential to address real clinical limitations. In finding that the subsequent image quality was no worse than that achieved by the existing clinical methods, we demonstrated that these non-circular scanning trajectories have the potential to address limitations of CBCT in IGRT. Though we did not explicitly study any other application here, we do not think this framework is limited to these two applications or even solely to the purview of radiotherapy. In selecting the two examples shown here, we have only wished to demonstrate the potential utility enabled by non-circular trajectories with optimization-based reconstruction. As with all tomographic reconstruction problems, careful consideration must be given to the desired task and further task-based metric analysis must be performed to evaluate not only the performance of the chosen reconstruction chain, but also to that of the chosen scanning trajectory.

REFERENCES

[1] Harrison H. Barrett and Kyle J. Myers. Foundations of Image Science. *Foundations of Image Science , by Harrison H. Barrett, Kyle J. Myers, pp. 1584. ISBN 0-471-15300-1. Wiley-VCH , October 2003.*, October 2003.

[2] Stewart J. Becker, Wes Culberson, and Ryan Flynn. Collision indicator charts for gantry-couch position combinations for Siemens ONCOR and Elekta Infinity linacs. *Journal of Applied Clinical Medical Physics*, 14(5), September 2013.

[3] Junguo Bian, Jeffrey H. Siewerdsen, Xiao Han, Emil Y. Sidky, Jerry L. Prince, Charles A. Pelizzari, and Xiaochuan Pan. Evaluation of sparse-view reconstruction from flat-panel-detector cone-beam CT. *Physics in Medicine and Biology*, 55(22):6575, November 2010.

[4] Junguo Bian, Jiong Wang, Xiao Han, Emil Y. Sidky, Lingxiong Shao, and Xiaochuan Pan. Optimization-based image reconstruction from sparse-view data in offset-detector CBCT. *Physics in Medicine and Biology*, 58(2):205, January 2013.

[5] Jean-Pierre Bissonnette, Peter A. Balter, Lei Dong, Katja M. Langen, D. Michael Lovelock, Moyed Miften, Douglas J. Moseley, Jean Pouliot, Jan-Jakob Sonke, and Sua Yoo. Quality assurance for image-guided radiation therapy utilizing CT-based technologies: A report of the AAPM TG-179. *Medical Physics*, 39(4):1946–1963, April 2012.

[6] Buzug, Thorston M. Fundamentals of X-ray Physics. In *Computed Tomography*, pages 15–73. Springer Berlin Heidelberg, 2008. DOI: 10.1007/978-3-540-39408-2_2.

[7] Buzug, Thorston M. Milestones of Computed Tomography. In *Computed Tomography*, pages 75–99. Springer Berlin Heidelberg, 2008. DOI: 10.1007/978-3-540-39408-2_3.

[8] Buzug, Thorston M. Three-Dimensional Fourier-Based Reconstruction Methods. In *Computed Tomography*, pages 303–401. Springer Berlin Heidelberg, 2008. DOI: 10.1007/978-3-540-39408-2_8.

[9] Buzug, Thorston M. Two-Dimensional Fourier-Based Reconstruction Methods. In *Computed Tomography*, pages 151–200. Springer Berlin Heidelberg, 2008. DOI: 10.1007/978-3-540-39408-2_5.

[10] Wei Chang, S. Loncaric, Gang Huang, and P. Sanpitak. Asymmetric fan transmission CT on SPECT systems. *Physics in Medicine and Biology*, 40(5):913, May 1995.

[11] Max M. Chao, Liang S. Chao, Yu J. Chen, Chuen M. Hsieh, Shueh C. Liou, Yuh L. Lee, and and Sang H. Yen. Image Display for Collision Avoidance of Radiation Therapy: Treatment Planning. *Journal of Digital Imaging*, 14(4):186, December 2001.

[12] P. S. Cho, R. H. Johnson, and T. W. Griffin. Cone-beam CT for radiotherapy applications. *Physics in Medicine and Biology*, 40(11):1863, November 1995.

[13] Youngbin Cho, Douglas J. Moseley, Jeffrey H. Siewerdsen, and David A. Jaffray. Accurate technique for complete geometric calibration of cone-beam computed tomography systems. *Medical Physics*, 32(4):968–983, 2005.

[14] M. J. Daly, J. H. Siewerdsen, Y. B. Cho, D. A. Jaffray, and J. C. Irish. Geometric calibration of a mobile C-arm for intraoperative cone-beam CT. *Medical Physics*, 35(5):2124–2136, April 2008.

[15] A. Davis, E. Pearson, X. Pan, and C. Pelizzari. WE-G-BRF-07: Non-Circular Scanning Trajectories with Varian Developer Mode. *Medical Physics*, 41(6):523–523, June 2014.

[16] Andrew Davis, Erik Pearson, Xiaochuan Pan, and Charles Pelizzari. Extended Axial Field of View in Radiotherapy Cone-Beam CT with Iterative Reconstruction. In *Fully Three-Dimensional Image Reconstruction in Radiology and Nuclear Medicine*, Lake Tahoe, CA, 2013.

[17] Laura A. Dawson and David A. Jaffray. Advances in Image-Guided Radiation Therapy. *Journal of Clinical Oncology*, 25(8):938–946, March 2007.

[18] A. P. Dempster, N. M. Laird, and D. B. Rubin. Maximum Likelihood from Incomplete Data via the EM Algorithm. *Journal of the Royal Statistical Society. Series B (Methodological)*, 39(1):1–38, January 1977.

[19] Ronald T. Droege and Richard L. Morin. A practical method to measure the MTF of CT scanners. *Medical Physics*, 9(5):758–760, September 1982.

[20] R. Fahrig and D. W. Holdsworth. Three-dimensional computed tomographic reconstruction using a C-arm mounted XRII: Image-based correction of gantry motion nonidealities. *Medical Physics*, 27(1):30–38, January 2000.

[21] L. A. Feldkamp, L. C. Davis, and J. W. Kress. Practical cone-beam algorithm. *Journal of the Optical Society of America A*, 1(6):612–619, June 1984.

[22] David V. Finch. Cone Beam Reconstruction with Sources on a Curve. *SIAM Journal on Applied Mathematics*, 45(4):665–673, August 1985.

[23] P. Forthmann, M. Grass, and R. Proksa. Adaptive two-pass cone-beam artifact correction using a FOV-preserving two-source geometry: A simulation study. *Medical Physics*, 36(10):4440–4450, September 2009.

[24] Pierre Grangeat. Mathematical framework of cone beam 3d reconstruction via the first derivative of the radon transform. In Gabor T. Herman, Alfred K. Louis, and Frank Natterer, editors, *Mathematical Methods in Tomography*, number 1497 in Lecture Notes in Mathematics, pages 66–97. Springer Berlin Heidelberg, January 1991.

[25] Grant T. Gullberg, Benjamin M. W. Tsui, Carl R. Crawford, J. Glen Ballard, and John T. Hagius. Estimation of geometrical parameters and collimator evaluation for cone beam tomography. *Medical Physics*, 17(2):264–272, March 1990.

[26] Xiao Han, Junguo Bian, Erik L. Ritman, Emil Y. Sidky, and Xiaochuan Pan. Optimization-based reconstruction of sparse images from few-view projections. *Physics in Medicine and Biology*, 57(16):5245, August 2012.

[27] Gabor T. Herman, Arnold Lent, and Stuart W. Rowland. ART: Mathematics and applications: A report on the mathematical foundations and on the applicability to real data of the algebraic reconstruction techniques. *Journal of Theoretical Biology*, 42(1):1–32, November 1973.

[28] Jiang Hsieh. *Computed Tomography, Second Edition.* SPIE, 1000 20th Street, Bellingham, WA 98227-0010 USA, October 2009.

[29] Chiaho Hua, Jenghwa Chang, Kamil Yenice, Maria Chan, and Howard Amols. A practical approach to prevent gantry–couch collision for linac-based radiosurgery. *Medical Physics*, 31(7):2128–2134, July 2004.

[30] John L. Humm, Domenico Pizzuto, Eric Fleischman, and Radhe Mohan. Collision detection and avoidance during treatment planning. *International Journal of Radiation Oncology*Biology*Physics*, 33(5):1101–1108, December 1995.

[31] International Electrotechnical Commission, International Electrotechnical Commission, and Technical Committee 62. *Radiotherapy equipment–coordinates, movements and scales = Appareils utilisés en radiothérapie–coordonnées, mouvements et échelles.* International Electrotechnical Commission, Geneva, 2011. OCLC: 772343784.

[32] David A Jaffray, Douglas G Drake, Michel Moreau, Alvaro A Martinez, and John W Wong. A radiographic and tomographic imaging system integrated into a medical linear accelerator for localization of bone and soft-tissue targets. *International Journal of Radiation Oncology*Biology*Physics*, 45(3):773–789, October 1999.

[33] David A. Jaffray, Jeffrey H. Siewerdsen, Gregory K. Edmundson, John W. Wong, and Alvaro A. Martinez. Flat-panel cone-beam CT on a mobile isocentric C-arm for image-guided brachytherapy. volume 4682, pages 209–217, 2002.

[34] Roger H. Johnson, Hui Hu, Steven T. Haworth, Paul S. Cho, Christopher A. Dawson, and John H. Linehan. Feldkamp and circle-and-line cone-beam reconstruction for 3d micro-CT of vascular networks. *Physics in Medicine and Biology*, 43(4):929, April 1998.

[35] W A Kalender, W Seissler, E Klotz, and P Vock. Spiral volumetric CT with single-breath-hold technique, continuous transport, and continuous scanner rotation. *Radiology*, 176(1):181–183, July 1990.

[36] A Katsevich, K. Taguchi, and AA Zamyatin. Formulation of four katsevich algorithms in native geometry. *IEEE Transactions on Medical Imaging*, 25(7):855–868, July 2006.

[37] Alexander Katsevich. Theoretically Exact Filtered Backprojection-Type Inversion Algorithm for Spiral CT. *SIAM Journal on Applied Mathematics*, 62(6):2012–2026, January 2002.

[38] Alexander Katsevich. Image reconstruction for the circle and line trajectory. *Physics in Medicine and Biology*, 49(22):5059, November 2004.

[39] Alexander Katsevich. Image reconstruction for the circle-and-arc trajectory. *Physics in Medicine and Biology*, 50(10):2249, May 2005.

[40] Alexander Katsevich, Samit Basu, and Jiang Hsieh. Exact filtered backprojection reconstruction for dynamic pitch helical cone beam computed tomography. *Physics in Medicine and Biology*, 49(14):3089, July 2004.

[41] H. Kudo and T. Saito. Helical-scan computed tomography using cone-beam projections. In *, Conference Record of the 1991 IEEE Nuclear Science Symposium and Medical Imaging Conference, 1991*, pages 1958–1962 vol.3, November 1991.

[42] H. Kudo and T. Saito. Derivation and implementation of a cone-beam reconstruction algorithm for nonplanar orbits. *IEEE Transactions on Medical Imaging*, 13(1):196–211, March 1994.

[43] Hiroyuki Kudo and Tsuneo Saito. Fast and stable cone-beam filtered backprojection method for non-planar orbits. *Physics in Medicine and Biology*, 43(4):747, April 1998.

[44] S. Kullback and R. A. Leibler. On Information and Sufficiency. *The Annals of Mathematical Statistics*, 22(1):79–86, March 1951.

[45] Marina Kushnirsky, Vaibhav Patil, and Michael Schulder. The History of Stereotactic Radiosurgery. In Lawrence S. Chin and William F. Regine, editors, *Principles and Practice of Stereotactic Radiosurgery*, pages 3–10. Springer New York, 2015.

[46] J. Lagarias, J. Reeds, M. Wright, and P. Wright. Convergence Properties of the Nelder–Mead Simplex Method in Low Dimensions. *SIAM Journal on Optimization*, 9(1):112–147, January 1998.

[47] Xinhua Li, Da Zhang, and Bob Liu. A generic geometric calibration method for tomographic imaging systems with flat-panel detectors—A detailed implementation guide. *Medical Physics*, 37(7):3844–3854, July 2010.

[48] Daniel Létourneau, John W. Wong, Mark Oldham, Misbah Gulam, Lindsay Watt, David A. Jaffray, Jeffrey H. Siewerdsen, and Alvaro A. Martinez. Cone-beam-CT guided radiation therapy: technical implementation. *Radiotherapy and Oncology*, 75(3):279–286, June 2005.

[49] Charles E. Metz. Basic principles of ROC analysis. *Seminars in Nuclear Medicine*, 8(4):283–298, October 1978.

[50] M.M. Mitschke and N. Navab. Optimal configuration for dynamic calibration of projection geometry of X-ray C-arm systems. In *IEEE Workshop on Mathematical Methods in Biomedical Image Analysis, 2000. Proceedings*, pages 204–209, 2000.

[51] Siddhartha. Mukherjee. *The emperor of all maladies: a biography of cancer.* Scribner, New York, 1st scribner hardcover ed. edition, 2010.

[52] Elena Nioutsikou, James L. Bedford, and Steve Webb. Patient-specific planning for prevention of mechanical collisions during radiotherapy. *Physics in Medicine and Biology*, 48(22):N313, November 2003.

[53] F. Noo, M. Defrise, R. Clack, T. J. Roney, T. A. White, and S. G. Galbraith. Stable and efficient shift-variant algorithm for circle-plus-lines orbits in cone-beam CT. In *, International Conference on Image Processing, 1996. Proceedings*, volume 3, pages 539–542 vol.3, September 1996.

[54] Frédéric Noo, Rolf Clackdoyle, Catherine Mennessier, Timothy A. White, and Timothy J. Roney. Analytic method based on identification of ellipse parameters for scanner calibration in cone-beam tomography. *Physics in Medicine and Biology*, 45(11):3489, November 2000.

[55] Mark Oldham, Daniel Létourneau, Lindsay Watt, Geoffrey Hugo, Di Yan, David Lockman, Leonard H. Kim, Peter Y. Chen, Alvaro Martinez, and John W. Wong. Cone-beam-CT guided radiation therapy: A model for on-line application. *Radiotherapy and Oncology*, 75(3):271.E1–271.E8, June 2005.

[56] L. Padilla, E. A. Pearson, and C. Pelizzari. Patient-Specific Collision Detection Package Using Surface Imaging. *International Journal of Radiation Oncology • Biology • Physics*, 90(1):S827, September 2014.

[57] Laura Padilla, Erik A. Pearson, and Charles A. Pelizzari. Collision prediction software for radiotherapy treatments. *Medical Physics*, 42(11):6448–6456, November 2015.

[58] Xiaochuan Pan, Emil Y. Sidky, and Michael Vannier. Why do commercial CT scanners still employ traditional, filtered back-projection for image reconstruction? *Inverse Problems*, 25(12):123009, December 2009.

[59] D. Panetta, N. Belcari, A. Del Guerra, and S. Moehrs. An optimization-based method for geometrical calibration in cone-beam CT without dedicated phantoms. *Physics in Medicine and Biology*, 53(14):3841, July 2008.

[60] Dennis L. Parker. Optimal short scan convolution reconstruction for fan beam CT. *Medical Physics*, 9(2):254–257, March 1982.

[61] E.A. Pearson, Seungryong Cho, Charles A. Pelizzari, and Xiaochuan Pan. Non-circular cone beam CT trajectories: A preliminary investigation on a clinical scanner. In *2010 IEEE Nuclear Science Symposium Conference Record (NSS/MIC)*, pages 3172–3175, October 2010.

[62] Maryam Rahman, Gregory J. A. Murad, Frank J. Bova, and William A. Friedman. LINAC: Past, Present, and Future of Radiosurgery. In Lawrence S. Chin and William F. Regine, editors, *Principles and Practice of Stereotactic Radiosurgery*, pages 121–134. Springer New York, 2015.

[63] Kurt Rossmann. Point spread-function, line spread-function, and modulation transfer function: Tools for the study of imaging systems 1. *Radiology*, 93(2):257–272, 1969.

[64] Anne Rougée, Catherine Picard, Cyril Ponchut, and Yves Trousset. Geometrical calibration of x-ray imaging chains for three-dimensional reconstruction. *Computerized Medical Imaging and Graphics*, 17(4–5):295–300, July 1993. bibtex: rougee_geometrical_1993.

[65] Olle Seger and Maria Magnusson Seger. *The MATLAB/C program take - a program for simulation of X-ray projections from 3D volume data. Demonstration of beam-hardening artefacts in subsequent CT reconstruction.* Linköping University, Department of Electrical Engineering, 2005. The MATLAB/C program take version 3.1 is a program for simulation of X-ray projections from 3D volume data. It is based on an older C version by Muller-Merbach as well as an extended C version by T ...

[66] G. C. Sharp, N. Kandasamy, H. Singh, and M. Folkert. GPU-based streaming architectures for fast cone-beam CT image reconstruction and demons deformable registration. *Physics in Medicine and Biology*, 52(19):5771, September 2007.

[67] Michael B. Sharpe, Douglas J. Moseley, Thomas G. Purdie, Mohammad Islam, Jeffrey H. Siewerdsen, and David A. Jaffray. The stability of mechanical calibration for a kV cone beam computed tomography system integrated with linear acceleratora). *Medical Physics*, 33(1):136–144, December 2005.

[68] L.A. Shepp and Y. Vardi. Maximum Likelihood Reconstruction for Emission Tomography. *IEEE Transactions on Medical Imaging*, 1(2):113–122, October 1982.

[69] Emil Y. Sidky, Chien-Min Kao, and Xiaochuan Pan. Accurate image reconstruction from few-views and limited-angle data in divergent-beam CT. *Journal of X-Ray Science and Technology*, 14(2):119–139, January 2006.

[70] Emil Y Sidky and Xiaochuan Pan. Image reconstruction in circular cone-beam computed tomography by constrained, total-variation minimization. *Physics in Medicine and Biology*, 53(17):4777–4807, September 2008.

[71] E.Y. Sidky, R. Chartrand, and Xiaochuan Pan. Image reconstruction from few views by non-convex optimization. In *IEEE Nuclear Science Symposium Conference Record, 2007. NSS '07*, volume 5, pages 3526–3530, October 2007.

[72] E.Y. Sidky, Yu Zou, and Xiaochuan Pan. Volume image reconstruction from a straight-line source trajectory. In *2005 IEEE Nuclear Science Symposium Conference Record*, volume 5, pages 2441–2444, 2005.

[73] Michael D. Silver, Anindya Sen, and Satoru Oishi. Determination and correction of the wobble of a C-arm gantry. pages 1459–1468, June 2000.

[74] Lorenz von Smekal, Marc Kachelriess, Elizaveta Stepina, and Willi A. Kalender. Geometric misalignment and calibration in cone-beam tomography. *Medical Physics*, 31(12):3242–3266, 2004.

[75] Miltiadis F. Tsiakalos, Eduard Schrebmann, Kiki Theodorou, and Constantin Kappas. Graphical treatment simulation and automated collision detection for conformal and stereotactic radiotherapy treatment planning. *Medical Physics*, 28(7):1359–1363, July 2001.

[76] Heang K. Tuy. An Inversion Formula for Cone-Beam Reconstruction. *SIAM Journal on Applied Mathematics*, 43(3):546–552, June 1983. ArticleType: research-article / Full publication date: Jun., 1983 / Copyright © 1983 Society for Industrial and Applied Mathematics.

[77] Khinh Ranh Voong, Kelli McSpadden, Chelsea C. Pinnix, Ferial Shihadeh, Valerie Reed, Mohammad R. Salehpour, Isidora Arzu, He Wang, David Hodgson, John Garcia, Michalis Aristophanous, and Bouthaina S. Dabaja. Dosimetric advantages of a "butterfly" technique for intensity-modulated radiation therapy for young female patients with mediastinal Hodgkin's lymphoma. *Radiation Oncology*, 9(1):1–17, April 2014.

[78] Julia Wicklein, Holger Kunze, Willi A. Kalender, and Yiannis Kyriakou. Image features for misalignment correction in medical flat-detector CT. *Medical Physics*, 39(8):4918–4931, July 2012.

[79] D. Xia, P. Paysan, Z. Zhang, D. Seghers, M. Brehm, P. Munro, A. M. Davis, M. Lehmann, E. Y. Sidky, C. Pelizzari, and X. Pan. Optimization-based reconstruction from megavoltage cone-beam CT data in image guided radiation therapy. In *Proc. 4th Intl. Mtg. on image formation in X-ray CT*, pages 415–8, 2016.

[80] Lei Xing, Brian Thorndyke, Eduard Schreibmann, Yong Yang, Tian-Fang Li, Gwe-Ya Kim, Gary Luxton, and Albert Koong. Overview of image-guided radiation therapy. *Medical Dosimetry*, 31(2):91–112, 2006.

[81] Fang Xu and K. Mueller. Accelerating popular tomographic reconstruction algorithms on commodity PC graphics hardware. *IEEE Transactions on Nuclear Science*, 52(3):654–663, 2005.

[82] Kai Yang, Alexander L. C. Kwan, DeWitt F. Miller, and John M. Boone. A geometric calibration method for cone beam CT systems. *Medical Physics*, 33(6):1695–1706, 2006.

[83] G. L. Zeng and G. T. Gullberg. A cone-beam tomography algorithm for orthogonal circle-and-line orbit. *Physics in Medicine and Biology*, 37(3):563, March 1992.

[84] Yu Zou, Dan Xia, Lifeng Yu, E. Sidky, and Xiaochuan Pan. Image reconstruction from longitudinally and transversely truncated data along an arc-line trajectory. In *2005 IEEE Nuclear Science Symposium Conference Record*, volume 4, pages 2433–2436, 2005.